Multi-scale Modelling of Biohydrogen Production in Closed Photobioreactors

A thesis submitted to The University of Manchester for the degree of

Doctor of Philosophy (PhD)

in the Faculty of Science and Engineering

2022

Bovinille Anye Cho

Department of Chemical Engineering

Abstract

The synthesis of bio-based products, fuels, and materials in large-scale closed-photobioreactors (PBRs) presents a sustainable option for tackling the ever-increasing mass and energy demands of the world's rapidly growing population. With the scale-up of production comes significant cost reductions and increased commercial viability. However, successful PBR scale-up must overcome key hurdles relating to the local environmental conditions, including uneven light distribution caused by cellular absorption and mutual shading, as well as nutrient and biohydrogen partial pressure gradients. Therefore, this thesis confronts these engineering challenges with advanced mathematical modelling techniques by tackling the biotechnology's multi-scale complexities with minimum simulation cost strategies. The proposed models were thoroughly validated using both literature and experimental data collected from cultivating different microbial species in PBRs of different configurations and scales.

In a "journal format" style thesis, Chapters 1 to 2 covers the general introduction and comprehensive literature review whereas Chapters 3 to 5 present the published original contributions. More specifically, Chapter 3 proposes the first-ever mechanistic model to directly integrate the effect of PBR mixing-induced light/dark cycles into the biomass growth kinetics. This enables the manipulation of the PBR mixing rate to alleviate light attenuation challenges and maintain higher biomass growth rates. Chapter 4 extends the mechanistic model's capabilities to account for the effects of temperature and PBR biohydrogen partial pressure, which were previously ununified for any microbial species. To evaluate the biotechnological transfer across two types of PBR, namely the Schott bottle-based and vertical tubular-based PBR, two parameters related to the PBR's local environmental conditions were derived: the *effective light coefficient* and the *biohydrogen enhancement coefficient* for recalibration. The successful systematic upscaling approach was recommended for other similar biosystems. Building on these achievements, Chapter 5 focuses on the multi-physics coupling within a Computational Fluid Dynamics (CFD) solver to facilitate optimisation and upscaling of biohydrogen production. For this, accelerated growth kinetics and parallel computing were combined to greatly reduce the simulation cost, enabling uncertainty estimation via Monte Carlo simulation for the first time.

Finally, Chapter 6 concludes the thesis and presents two future directions: the exploitation of the models developed in Chapters 3 and 5 for (i) model-based optimal control of PBR mixing, (ii) the optimisation of PBR static mixers to enhance biomass growth and biohydrogen productivity, and (iii) application to other scalable PBR configurations.

Declaration

No portion of the work referred to in the thesis has been submitted in support of an application for another degree or qualification of this or any other university or other institute of learning.

Bovinille Anye Cho

Copyright statement

i. The author of this thesis (including any appendices and/or schedules to this thesis) owns certain copyright or related rights in it (the "Copyright") and s/he has given The University of Manchester certain rights to use such Copyright, including for administrative purposes.

ii. Copies of this thesis, either in full or in extracts and whether in hard or electronic copy, may be made **only** in accordance with the Copyright, Designs and Patents Act 1988 (as amended) and regulations issued under it or, where appropriate, in accordance with licensing agreements which the University has from time to time. This page must form part of any such copies made.

iii. The ownership of certain Copyright, patents, designs, trademarks and other intellectual property (the "Intellectual Property") and any reproductions of copyright works in the thesis, for example graphs and tables ("Reproductions"), which may be described in this thesis, may not be owned by the author and may be owned by third parties. Such Intellectual Property and Reproductions cannot and must not be made available for use without the prior written permission of the owner(s) of the relevant Intellectual Property and/or Reproductions.

iv. Further information on the conditions under which disclosure, publication and commercialisation of this thesis, the Copyright and any Intellectual Property and/or Reproductions described in it may take place is available in the University IP Policy (see http://documents.manchester.ac.uk/DocuInfo.aspx?DocID=24420) in any relevant Thesis restriction declarations deposited in the University Library, The University Library's regulations (see http://www.library.manchester.ac.uk/about/regulations/) and in The University's policy on Presentation of Theses.

Acknowledgements

I am and will forever be grateful to my main supervisor Dr. Dongda Zhang, internal co-supervisor Prof. Robin Smith, and external co-supervisor Dr. Antonio Del Rio Chanona for firstly accepting me into their research group. Since the beginning, you have provided me with sound technical advice, invaluable guidance and support, and immeasurable time input into the realisation of this research project. Thank you all immensely, especially to Dr. Dongda Zhang.

I am forever grateful to the Commonwealth Scholarship Commission in the United Kingdom for providing me with this unique and financially generous PhD opportunity. For three consecutive years, I received monthly stipends, NHS health insurance coverage, paid tuition (not cheap 24,000 GBP/ year), travel grants, to-and-fro flight tickets, just to name a few.

I wish to appreciate our external collaborators: Prof. Robert Pott at Stellenbosch University, South Africa and Prof. David Lea-Smith at University of East Anglia, United Kingdom, for sharing valuable insights and generating experimental datasets during our collaborations.

A big thank you to my comrades then at (i) Stellenbosch University, South Africa: Dr. Godfrey Gakingo and Dr. George Mbella Teke, at (ii) The University of Manchester, United Kingdom: Dr. Max Mowbray, Alex Norman, Alexander W. Rogers, Fernando Vega-Ramon and Oliver Pennington, and at (iii) Imperial College London, United Kingdom: Miguel Angel de Carvalho Servia and Thomas Savage. We exchanged knowledge and insights during group meetings, peer-reviewed my drafted manuscripts and provided insightful feedback for improvement, as well as socialised in pubs over a few pints. All this made my PhD experience in a foreign country pleasurable.

To conclude, I wish to express my sincere gratitude to my beloved mom, Asanji Patience Fru and siblings, Anye Makeeva Awah and Asanji Alain Aburi for their unconditional support and loving care despite being many miles aways.

List of Publications

Journal Publications:

1. D. Zhang, T. Savage, & **B. Anye Cho**, (2020). Combining model structure identification and hybrid modelling for photo-production process predictive simulation and optimisation. https://doi.org/10.1002/bit.27512.
2. **B. Anye Cho**, M. A. Carvalho Servia, E. A. del Rio Chanona, R. Smith, & D. Zhang (2021). Synergising biomass growth kinetics and transport mechanisms to simulate light/dark cycle effects on photo-production systems. https://doi.org/10.1002/bit.27707.
3. **B. Anye Cho**, B. S. Ross, J. P. du Toit, R.W.M.C. Pott, E. A. del Rio Chanona, & D. Zhang (2021). Dynamic modelling of *Rhodopseudomonas palustris* biohydrogen production: Perturbation analysis and photobioreactor upscaling. https://doi.org/10.1016/j.ijhydene.2021.08.162.
4. M. Mowbray, T. Savage, C. Wu, Z. Song, **B. Anye Cho**, E. A. del Rio Chanona & D. Zhang (2021). Machine learning for biochemical engineering: A review. https://doi.org/10.1016/j.bej.2021.108054.
5. L. Gerken-Starepravo, X. Zhu, **B. Anye Cho**, F. Vega-Ramon, O. Pennington, E. A. del Rio Chanona, K. Jing & D. Zhang (2022). An MIQP framework for metabolic pathways optimization and dynamic flux analysis. https://doi.org/10.1016/j.dche.2022.100011.
6. Z. Song, A. Rogers, **B. Anye Cho**, K. Jing, & D. Zhang (2022). Kinetic modelling of γ-linolenic acid production by Cunninghamella echinulate. https://doi.org/10.1016/B978-0-323-95879-0.50019-9.
7. **B. Anye Cho**, B. S. Ross, J. P. du Toit, R.W.M.C. Pott, E. A. del Rio Chanona, & D. Zhang (2022). Dynamic modelling of light and temperature effects on biomass growth and biohydrogen production by the photosynthetic bacterium *Rhodopseudomonas palustris.* https://doi.org/10.1016/B978-0-323-95879-0.50004-7.
8. **B. Anye Cho**, J. Á. Moreno-Cabezuelo, L. A. Mills, E. A. Del Rio Chanona, D. J. Lea-Smith, & D. Zhang (2023). Integrated experimental and photo-mechanistic modelling of biomass and optical density production of fast versus slow growing model cyanobacteria. https://doi.org/10.1016/j.algal.2023.102997.

9. **B. Anye Cho**, E. Grobler, R.W.M.C. Pott, E. A. del Rio Chanona, & D. Zhang (2022). A CFD coupled photo-bioreactive transport modelling of tubular photobioreactor mixed by peristaltic pump. Accepted by Chemical Engineering Science, currently in press.

Table of Contents

List of Figures

List of Tables

Chapter 1

General Introduction

This chapter briefly describes the PhD research carried out within the last three years (September 2019 to September 2022) and is structured into four sub-chapters. The first sub-chapter makes a case for biorenewable energy as a source of renewable energy for the future. The second sub-chapter presents the challenges surrounding systematic upscaling, while the third presents the PhD thesis aims and objectives. Then the final sub-section details the thesis structure and highlights the original contributions.

1.1 Biorenewable energy prospects

Continuing to meet the world's energy demand (circa 80% for electricity generation, transportation, and heating, as indicated by Dechatiwongse et al., and Anye Cho et al., [1,2]) by the large-scale combustion of fossil fuels is of increasing concerns due to the repercussions of global climate change. As a result, policymakers are striving to enact measures (e.g., the PARIS COP 21 Agreement) to limit global warming and greenhouse gas emissions by reducing the use of fossil-resource-derived fuels. This directive has spearheaded the research for clean and renewable energy sources such as wind, hydro, solar and biofuels. Among them, solar energy from the Sun, reaching the earth's atmospheric surface at an estimated rate of 1.73×10^{17} W or 6.38×10^{19} Wh year^{-1} by Pilon et al., [3] is by far, the most abundant renewable energy source available to humanity.

For this reason, significant research has been invested into developing technologies for capturing, converting, and storing solar energy to meet the world's mass and energy demands. Solar electricity is gaining much traction due to the ability of commercial photovoltaic (PV) cells to be manufactured in modular units and installed in small, distributed facilities like the roofs of local residences. These PV cells consist of semiconductor materials like silicon, selenium, germanium, cadmium telluride diselenide, copper indium, and indium antimonide, as highlighted by Bayod-Rujula [4]. Among the semiconductors, silicon derived from silica which composes 60 % of the earth's crust, is cheaply available. Thus silicon constitutes 90 % of the commercially available PV cells, as mentioned by Bayod-Rujula [4]. Even so, the solar-to-electrical energy conversion efficiencies of these PV cells are estimated by Green et al., [5] at 25 ± 0.5 %, while electricity by PV cells remains 5 to 10 times more expensive than that produced by burning fossil fuels.

Hence, PV power generation continues to struggle to compete as the primary energy source due to present semiconductor technological limitations.

The natural photosynthetic bioconversion process of solar into chemical energy, stored in several biomolecules such as sugars, starch, and lipids, to name a few, presents a viable alternative. This is because the biomolecules constituents of crops, plants, macroalgae (e.g., seaweed), microalgae (e.g., cyanobacteria) and bacteria can become precursors to various transport biofuels. For instance: (i) bioethanol by the authors Tang et al., and Kim-Dale [6,7], (ii) biodiesel by the authors Kim-Dale [7], (iii) biomethanol by the author Dong [8] and (iv) biohydrogen by the author Demirbas [9], to name a few. The fundamentals for obtaining these biomolecules via natural photosynthetic processes are detailed in Section 2.1 of this PhD thesis, while the photobiological production of biohydrogen was investigated in Chapter 4. For now, Section 1.1 revisits the classification of these biorenewable energy sources into three different generations.

The use of biomass from crops like corn, sugarcane, and soybeans for the production of liquid biofuels such as bioethanol in Kim-Dale [7] and biodiesel in the works of Kim-Dale and Hill et al., [7,10] are classified as first-generation biofuels. First-generation biofuels are characterised by their low energy densities (e.g., 21.26 MJ L^{-1} for bioethanol, as stated by Hill et al., [10]), so would therefore require large swaths of arable land to be turned over to biofuel production to replace the demand currently satiated by petroleum-derived transport fuels. Competing with agricultural land makes first-generation biofuels unattractive, given (i) the growing demand for food and water by the rapidly growing world's population and (ii) this would exacerbate the already large carbon footprint of ammonium-based fertilisers manufactured from the fossil fuel-intensive Haber-Bosch process.

On the other hand, second-generation biofuels are derived from nonedible plants like woody crops, lignocellulosic biomass, agricultural residues and wastes. For example, cellulose-based products from plants such as *Miscanthus* explored by Brosse et al., [11], switchgrass (*Panicum virgatum L.*) studied by Hartman et al., [12] and *Sorghum* investigated by Tang et al., [6], can all be converted into liquid biofuels. However, second-generation biofuels are also characterised by low energy densities (e.g., 21.26 MJ L^{-1} for bioethanol, as stated by Hill et al., [10]) and given the technological challenges associated with gasification, pyrolysis and fermentation, they remain commercially unviable.

Finally, third-generation biofuels are derived solely from microalgae (including cyanobacteria) and photosynthetic bacteria. In contrast to former generation biofuels, microalgae and photosynthetic bacteria grow faster and accumulate more biomolecules (e.g.,

up to 77 % lipids in the microalgae *Schizochytrium* sp. as reported by Chisti [13]), enabling higher biofuel productivities. These benefits can be attributed to their simpler structure and lack of roots, leaves or flowers, shrinking their geographical footprint, and water requirements so they can be cultivated away from more arable land. Despite the promising prospects, the commercial viability of third-generation biofuels is hampered by the high cost of small-scale production and their non-competitive price in the fossil-fuel-dominated liquid fuel market. Full details of these bottlenecks will now be elucidated in Section 1.2 of this PhD thesis.

1.2 Predictive scale-up perspectives

Given that producing third-generation biofuels at larger capacities is key to minimising the production, operational and maintenance costs, thus making them commercially viable, there is an urgent need for effective, affordable, scalable photobioreactors (i.e., a specialised piece of equipment for supporting microbial growth as reviewed in Chapter 2). Upscaling microbial cultivation and biofuel production from lab scale to pilot plant and industrial scale may initially seem trivial. For a specific power input and flow regime, one should increase the photobioreactor's diameter and/or height to achieve a volume within 10 L [14–17] for lab scale, within 500 L [17–21] for pilot plant scale, and 500 L or greater [17,22,23] for industrial scale. Furthermore, the microbes involved only require simple minimal growth media such as nitrates, phosphates, trace elements, and most importantly, the greenhouse gas carbon dioxide while in the presence of light.

However, supplying the required light intensity and of the correct wavelength to all the microbial cells within photobioreactors of different scales has proven challenging. This is due to the inability to store, pump or mix the light over space and time, while light attenuates due to cellular mutual shading. As such, microbial cells on the side of the photobioreactor facing the light source are exposed to higher light intensities and are prone to photoinhibition, while microbial cells in the photobioreactor's interior receive less light and are prone to becoming photolimited. The prohibitive combination of photoinhibition and photolimitation hinders biomass accumulation and biofuel productivity. This issue is often accentuated at larger scales (i.e., pilot plant and industrial scales) if the photobioreactor is upscaled naively by simply increasing its diameter and or height.

Predictive mathematical models incorporating limiting cultivation variables like light intensity and attenuation can facilitate systematic photobioreactor optimal design, control and upscale. Although a vast majority of models proposed in literature achieve satisfactory prediction accuracy within the same photobioreactor scale, they fail to predict across

different scales and configurations. This limitation can be attributed to: (i) the simpler assumption of perfectly mixed bioreactor conditions, which exclude hydrodynamic coupling to the bioreaction kinetics within solvers as per the works of Merchuck et al., [24,25] via the circulation time approach, and others as reviewed by Bechet et al., [26], (ii) the lack of theoretical support in the formulations of advanced multiscale coupling of bioreaction kinetics to hydrodynamic solvers as per the recent works of Gao et al., [16,27], (iii) the prohibitively high computational cost in resolving all micro-scale intracellular reactions kinetics and the macro-scale cell growth and hydrodynamic simulations as reported by Gao et al., [16,28].

The cellular activities are strongly coupled to local environmental conditions (e.g., light attenuation, nutrient and pH gradients). Therefore, models that are independent of spatial dimensions (i.e., (i) above) cannot predict the impact of increasing the photobioreactor's spatial dimensions (i.e., diameter and/or height). In contrast, models incorporating spatial dimensions (i.e., (ii) above) can account for the influences of changing the photobioreactor's diameter and /or height. However, current sophisticated approaches like those in the recent works of Gao et al., [27] first simulate the intracellular reaction kinetics over the spatio-temporal dimension and then separately compute the volume average cellular growth rate at regular time intervals. This is then used to calculate the photobioreactor's local light intensity distribution in other time intervals over the simulation period. However, this approach is only valid over short simulated time step sizes where the change in biomass concentration is negligible, so it is computationally expensive to simulate large-scale photobioreactors this way. This approach also assumes that the intracellular reaction kinetics occur in free suspension outside the microbial cell walls, violating biological knowledge. As per the latter models (i.e., (iii)), exploiting the Lagrangian simulation framework for thousands of particles over a sufficiently long period to estimate the cell light exposure history and then embed them into the intracellular reaction kinetics has proven both computationally expensive and numerically unstable. This is because of the increasing number of particles that must be simulated to ensure statistical significance for the larger computational domains of upscaled photobioreactors. In addition, the unphysical trapping of simulated particles in the boundary layers of photobioreactor walls due to the unavailability of submicron grid resolution was reported by Gao et al., [16,28] to affect the numerical accuracy of such approaches.

Therefore, there is an urgent need for high-fidelity multiscale photo-bioreactive transport models capable of considering the macroscopic scale (e.g., hydrodynamics, nutrients, cell

growth and by-product formation) and the microscopic scale (e.g., intracellular metabolic reactions, fluxes of light intensity and heat) with minimum computational cost. Such a model would enable optimal photobioreactor design and scaleup, contributing to the effective commercialisation of third-generation biofuels. This greater goal motivates the formulation of the aims and objectives for this PhD research, as presented in Section 1.3.

1.3 Thesis aims and objectives

To address the aforementioned challenges, this PhD research aims to develop high-fidelity multiscale photo-bioreactive transport models capable of integrating the biochemical reaction kinetics (i.e., micro-scale intracellular kinetics and macro-scale cell growth and by-product formation kinetics) with the macro-scale bioreactor fluid dynamics and light transport with minimal computational cost. The validated multiscale photo-bioreactive transport models are to be exploited to investigate the bioprocess performance and identify primary limiting factors affecting the design, optimisation, control and scale-up of different photobioreactors scales and configurations. To achieve the central aim of this PhD research, the following five objectives were formulated:

1. To incorporate the influence of macro-scale hydrodynamics into the original micro-scale three-state photosynthetic factory unit proposed by Eilers and Peeters [29]. However, the simultaneous simulation of both the micro and macro scales poses significant numerical challenges and is computationally infeasible. Therefore, theoretical derivations will be utilised to reduce model complexity without compromising simulation accuracy. If successful, the new model will be able to simulate the impact of light gradients within the bioreactor and mixing-induced light/dark cycles on macro-scale biomass growth and secondary metabolite (e.g., biohydrogen) production. There will be flexibility for incorporating additional cultivating variables like temperature and bioreactor biohydrogen partial pressure.

2. To exploit Computational Fluid Dynamics (CFD) in building a PDE solver that simulates the bioreactor fluid dynamics, light transmission, photosynthetic cell growth and secondary metabolite production at different photobioreactor scales and configurations. For this, ANSYS-Fluent, a commercial software used in the industry, was the CFD code of choice. Nonetheless, successfully coupling the bioreaction and light transport models developed under objective one requires the model parameters to be first identified. Due to the stiffness, nonlinearity, and complexity of the constructed models, stochastic swarm intelligence-based and derivative-based algorithms will be exploited for dynamic parameter estimation when appropriate. To

embed the photo-bioreaction kinetics within the commercial CFD solver, advanced programming skills are needed in programming languages C and Scheme to customise the CFD solver with User-Defined Functions and communication via Text User Interface to the Fluent solver cortex.

3. To investigate the computational efficiency of the multi-scale Eulerian CFD solver and propose efficient simulation strategies for enabling the realisation of the large-scale bioprocess optimisation. The two-step literature approach would recommend that the hydrodynamics are first solved to convergence, the converged flow fields frozen in place, and the slower bioreaction kinetics simulated over larger time steps. However, when simulating multiple state variables (i.e., biomass, substrate, and secondary metabolite production such as biohydrogen), even this approach is exorbitantly expensive (i.e., taking a few weeks to months), hindering large-scale bioprocess simulation and optimisation. Therefore, advanced modelling techniques (e.g., (i) acceleration of growth kinetics, (ii) parallel computing or a combination thereof) will be investigated to accelerate the simulation time without compromising the solution quality to attain superior cost savings compared to the current literature CFD models.

4. To identify the primary limiting factors affecting the design, control and scale-up of different bioreactor configurations and then optimise the operating conditions subject to profitability and environmental concerns. The proposed cost-efficient CFD solver integrating bioreactor fluid dynamics, light transmission and bioreaction transport will serve as the mechanistic surrogate of the true bioprocess. This will enable the design of *in-silico* experiments to test formulated hypotheses quickly, such as the influence of photo-bioreaction model parameter uncertainties under hydrodynamic coupling via Monte Carlo simulation, which is previously unanswered in literature.

5. To establish external collaborations with other international groups and leverage the collaborative network to generate experimental data. Although CFD solvers returns qualitative and quantitative predictions of the velocity, biomass, substrate (e.g., glycerol) and biohydrogen concentration contours, the results cannot be trusted without validation against data collected using accurate experimental methods like Laser Doppler Anemometry (LDA), High-Performance Liquid Chromatography (HPC) and Gas Chromatography (GC).

1.4 Thesis structure

This thesis is written and presented in a "journal format" style and features three original paper publications, which are compiled into three separate chapters. The novelty and research contributions made within each chapter are summarised as follows:

Chapter 3 – Synergising Biomass Growth Kinetics and Transport Mechanisms to Simulate Light/Dark Cycle Effects on Photo-production Systems.

Status: Published 6th February 2021- DOI: https://doi.org/10.1002/bit.27707.

- Presented the first mechanistic model directly integrating the effect of light/dark cycles on biomass growth kinetics without expensive external computation of cell light exposure history.
- Proposed a new parameter, the *effective light coefficient*, to account for the effect of culture mixing and an original nonlinear correlation linking the *effective light coefficient* to the photobioreactor gas inflow rate.
- Developed an efficient multiscale photo-bioreactive transport modelling strategy that coupled bioreactor fluid dynamics with biomass growth kinetics and light transmission.
- Enabled the control and optimisation of photobioreactor gas inflow rate to alleviate light attenuation and maintain a high biomass growth rate.

Chapter 4 – Dynamic Modelling of *Rhodopseudomonas palustris* Biohydrogen Production: Perturbation Analysis and Photobioreactor Upscaling.

Status: Published 26th October 2021- DOI: https://doi.org/10.1016/j.ijhydene.2021.08.162.

- Unified the complex influences of light intensity, light attenuation and temperature on biomass and biohydrogen production, previously not unified for photosynthetic bacteria.
- Exploited perturbation analysis to identify critical parameters influencing model prediction accuracy across two types of PBR: the Schott bottle-based and vertical tubular-based PBR.
- Proposed two parameters, the *effective light coefficient* and the *biohydrogen enhancement coefficient*, both linked to photobioreactor transport phenomena for model prediction recalibration during PBR scale-up and/or across PBR configurations.

- For the first time, mechanistically described the observed enhancement of biohydrogen production rate by improved culture mixing and gas removal rate.

Chapter 5 – A CFD Coupled Photo-Bioreactive Transport Modelling of Tubular Photobioreactors Mixed by Peristaltic Pump.

Status: Accepted by Chemical Engineering Science, currently in press.

- Proposed a cost-saving CFD-integrated photo-biokinetic framework for modelling externally pumped-recirculated photobioreactors.
- Combined accelerated growth kinetics and parallel computing to reduce computation time, enabling Monte Carlo simulation for a CFD-based framework for the first time.
- Excellent agreement with experimental tracer dye studies and bioreaction data to within 10 % error for simulated velocities and similar output uncertainties for the coupled CFD-photo-bioreaction and pure photo-bioreaction models.
- Using the model, undesirable regions with poor radial mixing were identified. Hence, static mixers were suggested to enhance the PBR's radial mixing (i.e., eliminating stagnant regions) to improve light/dark cycles, biomass growth and biohydrogen production.

Finally, general conclusions to the work done herein and recommendations for future work are presented in Chapter 6.

Chapter 2

Literature Review

In this Chapter, the background knowledge and concepts supporting the original contributions within this PhD research are presented. This is structured into seven sub-chapters with the first six being: fundamentals of microbial photosynthesis and biohydrogen production; photobioreactors: a choice of closed over open systems for microbial cultivation; mathematical modelling of biochemical reaction kinetics; dynamic model parameter estimation; mathematical modelling of photobioreactor fluid dynamics; multi-scale modelling of photobioreactor fluid dynamics and bioreactions. Finally, a summary of the first six sub-chapters (i.e., summary of the literature review Chapter) is presented as the seventh sub-chapter in addition to the PhD research objectives.

2.1 Fundamentals of microbial photosynthesis and biohydrogen production

Photosynthesis is broadly a multi-step process by which plants, macroalgae (e.g., seaweed), microalgae (including cyanobacteria) and photosynthetic bacteria can store light energy into various chemical forms such as carbohydrates and other metabolites like proteins and lipids, just to highlight a few, while using a carbon source (e.g., CO_2) as illustrated by Akkerman et al., and Berberoglu et al., [30,31] in Eq. (2.1). The sugars and metabolites constitute the building blocks of biomass whereby the microbial cells (e.g., microalgae) are reported to fix a higher biomass per unit carbon source than their plants (e.g., trees or sugar cane) or macroalgae (e.g., seaweed) counterparts. For instance, on a fixed surface area, microalgae alone can produce 30 times more oil than terrestrial oilseed crops as reported by Pilon et al., and Chisti [3,13], and the production occurs in facilities not requiring arable land, thus not competing for agricultural production as discussed by Mills et al., [32]. These greater photosynthetic fixing efficiencies are associated to their simpler cellular structure, the readily availability of low-cost carbon sources like flue gases (e.g., 4-14 vol% CO_2 from power plants stated by Pilon et al., [3]), and the other various dissolved nutrients in fresh and saltwater bodies. Therefore, the exploitation of microbial photosynthesis by industrial biotechnologist and bioprocess engineers presents a more promising route to attain some of these value-added bio-products of industrial importance such as organic compounds (e.g., isoprene [33]), amino acids (e.g., mycoporine-like amino acid [34]), and biofuels (e.g., biohydrogen [35]).

$$\mathrm{nCO_2 + nH_2O \xrightarrow{light} [CH_2O]_n + nO_2} \quad (2.1)$$

The subscript n in the general photosynthetic reaction in Eq. (2.1) can take any positive integer illustrating the chemical composition of the photosynthesised sugars. Also, Eq. (2.1) can be further decomposed into two separate reactions, namely light dependent reactions: generation of adenosine triphosphate (ATP) and nicotinamide adenine dinucleotide phosphate (NADPH), and light independent (i.e., dark) reactions: carbon fixation via Calvin-Benson-Basshan cycle to produce glyceraldehyde-3-phosphate [36]. In Eqs. (2.2) and (2.3) which are representations of the former and latter, the light and dark reactions are observed to interact via the ATP and NADPH but occurring in different cellular components, and time scales as reviewed by Carvalho et al., [36], depending on the species of the microorganisms under investigation.

$$\text{Light reactions: } \mathrm{2H_2O \xrightarrow{light} 4[NADPH + e^-] + O_2 + ATP} \quad (2.2)$$

$$\text{Dark reactions: } \mathrm{ATP + [NADPH + e^-] + CO_2 \xrightarrow{enzymes} [CH_2O] + H_2O} \quad (2.3)$$

Regarding the different cellular components, whilst the light dependent reactions occurs in the two Photosystems (i.e.., Photosystem I and II) for microalgae (i.e., including most cyanobacteria) upon the absorption of light by chlorophyll *a* and *b* as reported by Pilon et al., and Akkerman et al., [3,30], the same reactions only occur in one Photosystem (i.e.., Photosystem II) in purple photosynthetic bacteria upon the absorption of light by bacteriochlorophyll [3,30]. As per the existence of different time scales, whilst the light dependent reactions usually last a few milliseconds, the dark reactions on the other hand are normally completed within a few seconds to minutes as reported by Carvalho et al., [36]. However, based on the amounts of exposed light intensity, the subsequent generated amounts of ATP and NADPH varies significantly thereby warranting the microorganisms to implement several regulation mechanisms to survive such light conditions. As a result, the entire microbial photosynthesis process spans over several other different time scales such as the following in Table 2.1:

(i) Photoproduction: the absorption of light and utilisation for the generation of ATP and NADPH which occurs within milliseconds.

(ii) Photoinhibition: the photo-oxidative damages of the photosynthetic apparatus's pigment molecules due to extreme high light intensities and often proceeds between minutes to hours.

(iii) Photoregulation or Non-photochemical quenching: the short-term adjustment of the light absorbing pigment molecules for the efficient light reactions by dissipating excess photons as heat energy. This usually occurs within a few seconds to minutes.

(iv) Photoacclimation: just like in (iii) but are long-term adjustments which occur within hours to days.

Table 2.1: Analysis of the microbial photosynthetic time scales.

	Time scales	**ms**	**s**	**min**	**hr**	**day**	**Reference**
(i)	Photoproduction	**X**					[36,37]
(ii)	Photoinhibition			**X**	**X**		[37–39]
(iii)	Photoregulation		**X**	**X**			[37,38]
(iv)	Photoaclimation				**X**	**X**	[38,39]

Therefore, the microbial photosynthesis is not solely a multi-step process but also a multi-time process for the various species of microbes. In addition to the light induced survival steps and time scales, the available amounts and types of other culturing conditions such as organic vs inorganic carbon sources, with and/or without oxygen, just to highlight a few, can result to different microbial growth modes: namely (i) phototrophic, (ii) heterotrophic, (iii) mixotrophic, (iv) photoheterotrophic, (v) aerobic respiration, and (vi) anaerobic respiration, as briefly reviewed in Table 2.2. The various microbial growth modes tabulated in Table 2.2 typically occur in specialised technical equipment called photobioreactors and are briefly reviewed in the next sub-chapter as Section 2.2.

Table 2.2: Various growth modes of photosynthetic microorganisms adapted from Deo et al., [40].

Growth modes	**Carbon sources**	**Energy sources**	**Remarks**
Phototrophic	Inorganic carbon e.g., CO_2	Light e.g., solar radiation	Light from solar radiation and CO_2 from factories and power plants are abundantly available. However, light attenuation is growth limiting.
Heterotrophic	Organic carbon	Organic carbon e.g., sugars	Avoids light limitation challenges often experienced in dense

	e.g., sugars (glucose, sucrose)	(glucose, sucrose)	microbial cultures. However, organic carbon is not cheaply available like inorganic carbon (e.g., CO_2 in flue gases).
Mixotrophic	Inorganic and Organic carbon	Light or organic carbon	The organic carbon source could also serve as the energy source.
Photoheterotrophic	Organic carbon e.g., sugars (glucose, sucrose)	Light e.g., solar radiation	Corn powder hydrolysate and artichoke hydrolysate are cheaper alternative to organic carbon sources such as glucose, acetate, and glycerol.
Aerobic respiration	Inorganic or Organic carbon	Light or organic carbon	Oxygen is the terminal electron acceptor
Anaerobic respiration	Inorganic or Organic carbon	Light or organic carbon	Requires a terminal electron acceptor other than oxygen (e.g., nitrogen, hydrogen sulfide, or hydrogen)

Since the efficient and sustained photobiological production of biohydrogen is the rational of this PhD research, the tabulated microbial growth modes in Table 2.2 were further analysed for those supporting the hydrogen metabolism. With the taxonomically diverse photosynthetic microorganisms (green algae, blue-green algae, and purple non-sulfur bacteria, just to highlight a few) which can support biohydrogen production, there are several enzymes (e.g., hydrogenase, and nitrogenase as reported by the authors Azwar et al., Hallenbeck-Benemann and Eroglu-Melis [41–43]) involved in the several metabolic pathways and processes (see a summarised version in Figure 2.1) catalysing hydrogen production. However, the presence of oxygen as a cultivating variable or as the resulting by-product of the photosynthesis process is known in the literature [41–43] to suppress the gene expression of these enzymes and their activities. Therefore, Table 2.3 reviews oxygenic and anoxygenic processes of biohydrogen production together with the involved reactions catalysed by the specific enzymes for the various types of photosynthetic microorganisms.

Table 2.3: Photobiological hydrogen production routes adapted from the works of Deo et al. [40].

Conditions	Process/Organism	Enzymes	Reactions
Oxygenic	Direct biophotolysis (Microalgae and Cyanobacteria)	Hydrogenase	$2H_2O \xrightarrow{light} 2H_2 + O_2$ *Hydrogenase reaction:* $2H^+ + 2e^- \rightarrow 2H_2$
	Indirect biophotolysis (Filamentous Cyanobacteria)	Nitrogenase	*In vegetative cells:* $6CO_2 + 6H_2O \xrightarrow{light} C_6H_{12}O_6 + 6O_2$ *In heterocyst cells:* $C_2H_{12}O_6 + 6H_2O \xrightarrow{light} 6CO_2 + 12H_2$ *Nitrogenase reaction:* $N_2 + 8H^+ + 8e^- + 16ATP \rightarrow 2NH_3 + H_2 + 16ADP + 16P_i$
Anoxygenic	Photofermentation (Purple non-sulfur bacteria)	Nitrogenase	*Nitrogenase reaction:* $N_2 + 8H^+ + 8e^- + 16ATP \rightarrow 2NH_3 + H_2 + 16ADP + 16P_i$ *In absence of N_2:* $8H^+ + 8e^- + 16ATP \rightarrow 4H_2 + 16ADP + 16P_i$

Firstly, hydrogenase activities during the direct biophotolysis within Table 2.3 is inhibited by the release of oxygen from splitting water into protons and electrons. Therefore, very low yields of biohydrogen can be obtained and therefore requiring several circumventing strategies like (i) oxygen removal with inert gases and with haemoglobin, (ii) genetic modification for cells to consume any produced oxygen, (iii) sulfur removal from growth media to inhibit protein accumulation and cell growth, thus producing lesser oxygen, just to highlight a few, as reviewed by the authors Hellenbeck-Benemann and Eroglu-Melis [42,43]. Due to these insurmountable oxygen sensitivity challenges, research attention has been shifted towards filamentous cyanobacteria which undergoes hydrogen production via the indirect biophotolysis process. Even though water splitting, and oxygen evolution happens during the indirect biophotolysis, these reactions occur within spatially differentiate

cell compartments: the (i) vegetative cells responsible for photosynthetic growth (indicated in Figure 2.1 with pale green colour), from the (ii) heterocyst cells responsible for nitrogen fixation thereby containing nitrogenase enzymes (indicated in Figure 2.1 with blue colour), thus eliminating oxygen-induced nitrogenase repression. Therefore, the indirect biophotolysis process produces higher biohydrogen yields but the authors Hallenbeck-Benemann [42] reviewed the economics as questionable due to the cost of photobioreactor design, and its performances.

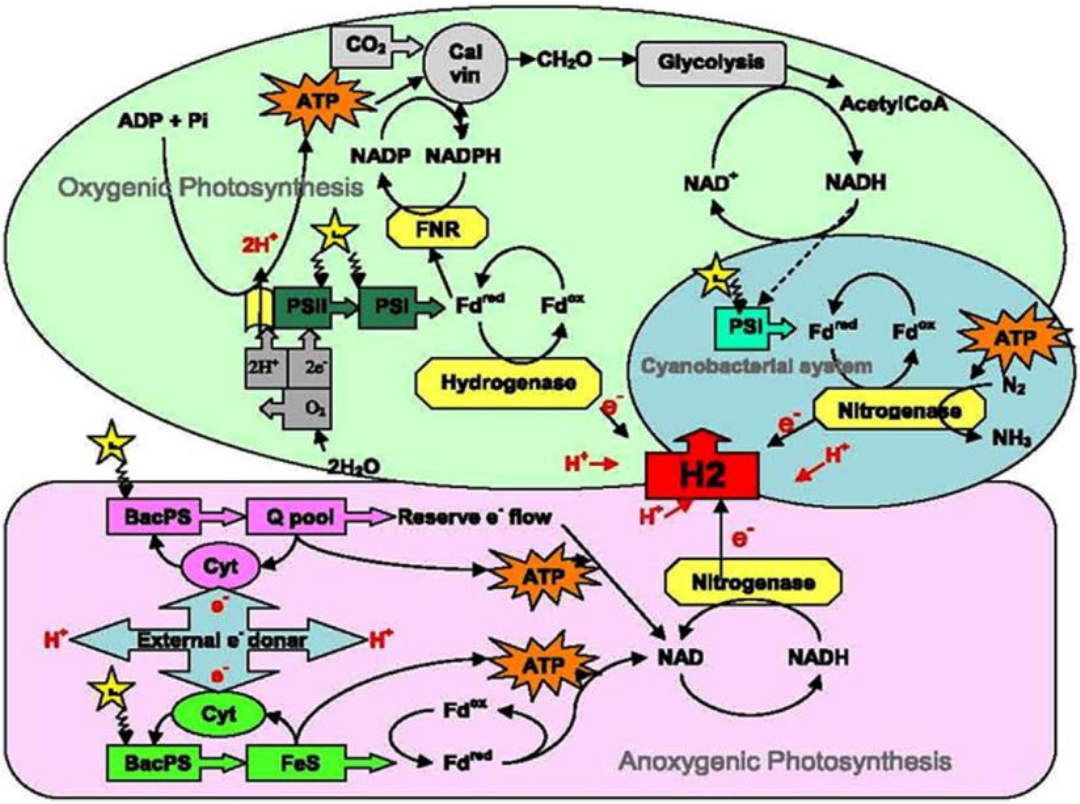

Figure 2.1: Schematics of electron flow during the photobiological hydrogen production process of both oxygenic and anoxygenic microorganisms as reproduced from the works of Azwar et al. [41]. Notice the spatially separated vegetative cells in pale green colour as to the heterocyst cells in blue colour within the oxygenic process. The anoxygenic process is indicated in purple colour.

On the other hand, the photofermentative route of biohydrogen production by purple non-sulfur bacteria occurs under the absence of oxygen and is catalysed by the nitrogenase enzymes as illustrated in Figure 2.1 with a purple colour. Interestingly, four more times of hydrogen is produced under nitrogen limiting conditions (see Table 2.3) for the same amount of ATP energy requirement in the nitrogen rich conditions. Just like in the indirect biophotolysis with filamentous cyanobacteria, the photobioreactor economics with photofermentation can be addressed as questionable, thus hindering large scale

photobiological hydrogen production. Therefore, the next sub-chapter (i.e., Section 2.2) focuses on reviewing these photobioreactor designs.

2.2 Photobioreactors: a choice of closed over open systems for microbial cultivation

Photobioreactors (PBRs) are technical systems within which the cultivation of photosynthetic microorganisms (e.g., microalgae, cyanobacteria, and photosynthetic bacteria) takes place. These PBRs mainly differ from classical bioreactors due to their additional light supply requirements to support the microbial photosynthetic process in the presence of other growth substrates as defined by Anye Cho and Pott [44]. These PBRs have been around since the 1950s and can be designed to be either open or cut-off from the atmosphere. Hence, they are therefore categorised into (i) open systems such as: natural ponds, lakes, lagoons, artificial ponds (raceway ponds), just to highlight a few as illustrated in Figure 2.2 and Figure 2.3 [45–47], and (ii) closed systems such as: continuous stirred tank PBR [48–50], flat plate PBR [14,51,52], torus PBR [53], airlift driven tubular PBR [54–56], thermosiphon PBR [44], bubble column tubular PBR [57–59], annular PBR [60], semi-partitioning PBR [61], and taylor-couette PBR [27,28,62] as illustrated in Figure 2.4.

Figure 2.2: Raceway open ponds reproduced from Yen et al., [46]

Figure 2.3: Circular open ponds reproduced from Waldrop [63]

Among the categories, open systems are mainly used commercially because of their simplicity, low capital, operational, and production costs [45,64,65]. Despite these advantages, open systems experience several drop backs such as (i) large land requirements, (ii) significant evaporative loss, (iii) poor light transfer and utilisation by photosynthetic microbial cells, (iv) carbon dioxide (CO_2) diffusion to the atmosphere, (v) poor mass transfer rates due to inefficient mixing/stirring mechanism, (vi) contamination and pollution by predators or other fast growing heterotrophs, and (vii) uncontrolled culture growth parameters such as pH levels, temperature, and nutrient supplies [45,64,66–68]. On the other hand, closed PBR systems can provide a balance of these growth parameter requirements while enabling their better control. However, this is often expensive due to the high capital and operational costs in conjunction with high maintenance costs as reported by Posten [69].

Nonetheless, closed PBR systems are particularly favorable for producing pharmaceutical grade value-added products, and gaseous secondary metabolites such as biohydrogen, whereby oxygen in the open systems would inhibit nitrogenase activity (i.e., biocatalyst for biohydrogen production) as discussed by Dasgupta et al., [70]. Regarding the latter biohydrogen productivity, if any or very little is produced within the open systems, it will simply escape into plein-air and therefore pointless. Therefore, closed PBR systems were chosen over open PBR systems for this PhD research.

Figure 2.4: Various scales of closed PBRs: lab scale PBRs (a) to (b), pilot plant scale PBRs (c), (d) reproduced from Lindblad et al., [23] and (e) reproduced from Adessi et al., [19], and industrial scale PBR (f) reproduced from Yen et al., [46].

The illustrated PBRs in Figure 2.4 do not illustrate the biohydrogen collection units. To economically achieve this, the hydrogen insolubility in water is often exploited by researchers, for example Tamburic et al., and Skjanes et al. [68,71], to trap the produced biohydrogen in an inverted measuring cylinder submerged within a beaker container as illustrated in Figure 2.5 A) and B). Then, an initial water volume mark is noted, and any changes to the volume mark indicated by water displacement during the biohydrogen production is noted and the volume of biohydrogen produced is calculated. Alternatively, the weights of the produced biohydrogen, measured with a digital balance, can also be used for the same calculations as reported by Skjanes et al. [71] in Figure 2.5 B). Despite being conceptually simple, the biohydrogen collection unit is a crucial part of guaranteeing the continuous photobiological production process. This is due to the reaction within the

heterocyst cells in Table 2.3 restated herein as Eq. (2.4) being inherently limited by the PBR's biohydrogen partial pressure and gaseous mass transfer. Therefore, if the produced biohydrogen is not removed and collected from the PBR, the PBR's biohydrogen partial pressures increases and shifts the equilibrium constant, K_c as defined in Eq. (2.5) to the left (backward reaction), thus hindering more production. However, when removed from the PBR as illustrated in Figure 2.5, the biohydrogen partial pressures reduces and shifts K_c to the right (forward reaction), thus enhancing more production according to Le Chateliers Principle reported in the works of Li et al. [72]. Another factor shifting K_c to the right (i.e., enhancing biohydrogen productivity) is by improving the PBR's gaseous mass transfer through its mixing enhancement. However, mathematical models embedding these crucial details into their predictions and enabling the manipulation of PBR mixing to sustain long lasting biohydrogen productivity were still pending prior to starting this PhD research. This was therefore investigated in Chapter 4 for the photosynthetic bacterium *R. palustris* and addressed with the proposal of a new parameter called the *biohydrogen enhancement factor*.

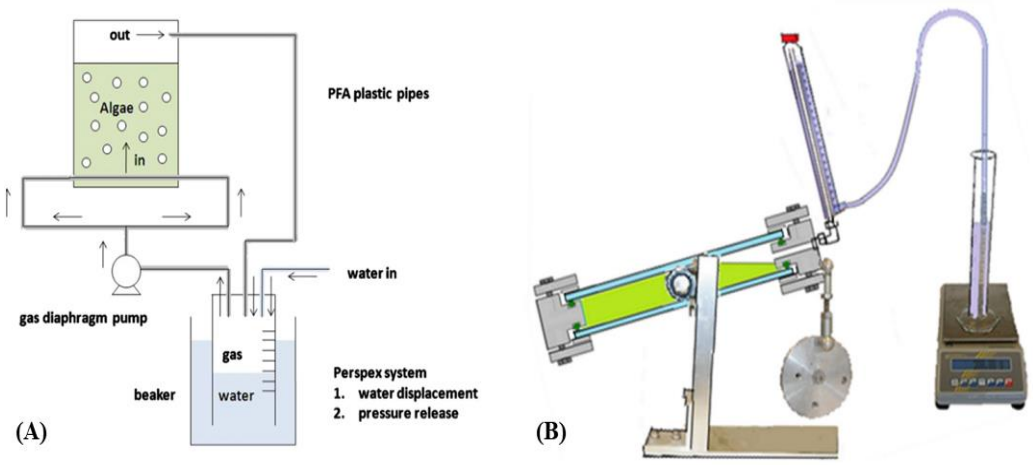

Figure 2.5: Hydrogen gas collection systems: (A) water displacement and hydrogen volume measurement as utilised by the authors Tamburic et al. [68], (B) water displacement and hydrogen volume and weight measurements as utilised by the authors Skjanes et al.[71].

$$C_2H_{12}O_6 + 6H_2O \xrightarrow{\text{light}} 6CO_2 + 12H_2 \tag{2.4}$$

$$K_c = \frac{[H_2]^{12} \cdot [CO_2]^6}{[C_6H_{12}O_6] \cdot [H_2O]^6} \tag{2.5}$$

Also, systematically upscaling the closed PBR systems form lab to pilot, and industrial scale by increasing the PBR's width and/or length as visualised in a) to f) of Figure 2.4 is not often regarded as feasible, thus contributing to the questionable economics as highlighted by the authors Hallenbeck-Benemann [42]. Specifically, the above mentioned PBR gaseous mass transfer issues coupled with the challenges associated with light attenuation are often

conspicuous in densely growing cultures, resulting in microbial cell mutual shadings. This leads to a majority of the PBR's incident light intensity being harvested by the microbial cells in the front-facing PBR section thereby leading to higher levels of photoinhibition meanwhile microbial cells in the PBR's interior will receive less light intensity and may become photolimited. These consequential effects hinders the PBR's optimal performance and upscaling are investigated in Chapters 3 and 4 respectively. Generally, to (i) effectively design, (ii) systematically scale-up, and (iii) optimally operate PBRs, careful understanding of the coupling between the biological response and environmental considerations must be captured in comprehensive mathematical models. Hence, the next sub-chapter (i.e., Section 2.3) presents a timely review of these mathematical models.

2.3 Mathematical modelling of biochemical reaction kinetics

Over the decades, several mathematical models have been developed to describe the microbial biological response and environmental considerations on the photosynthetic microbial cell growth, and secondary metabolite production in closed PBRs. Light intensity and temperature effects are the two most influencing culturing parameters commonly under review in literature, thus revisited herein.

2.3.1 Modelling the influences of light intensity, light attenuation and light/dark (L/D) cycles

Light is considered as an obligate requirement for photosynthetic microorganisms and light dependent mathematical models have been broadly categorised by Bechet et al., [26] into three main types (i.e., Type I, Type II and Type III) based on their theoretical ability to account for incident light intensity, light gradients and light/dark (L/D) cycles. Firstly, Type I and II models were looked into as they can assume same structural forms, thus jointly tabulated in Table 2.4. However, whilst Type I model predicts the photosynthetic rate of the entire microbial culture as a function of solely the PBR's incident light intensity, Type II additionally accounts for PBR's light attenuations effects. As a result, Type I models are only applicable to very thin-tube PBRs with short light path lengths and diffusively populated microbial cultures whereby the individual microbial cells are assumed to be exposed to the same incident light intensity. Meaning they have no commercial feasibilities for scale-up applications and will not be further reviewed.

On the other hand, Type II models account for the impact of light gradients on the local photosynthetic rate, thus applicable for upscaled PBRs with larger light path lengths and of commercial feasibilities [73–77]. However, they neglect the L/D cycles experienced by the individual microbial cells when cycling from the PBR's front-to-back sections due to mixing

of the PBR, except for the last hyperbolic structural model in Table 2.4 (derived from Type III model) proposed within this PhD research by Anye Cho et al., [52]. As such, when applied in densely growing microbial cultures, the previous Type II models overestimate the impact of light-inhibition on the local photosynthetic rate under the light gradient. Since, high biomass growth rate is the target for industrial cultivations, the strength of the proposed model by Anye Cho et al., [52] lies in the abilities of integrating the effects of culture mixing into the biomass growth kinetics via a new parameter, the *effective light coefficient, η* as mathematical derived from Type III models and validated in Chapter 3 of this PhD thesis.

Table 2.4: Published photosynthesis light response Type I and Type II models. Whereby $\mu(I)$: specific growth rate, μ_{max}: maximum specific growth rate, I: light intensity, I_0: incident light intensity, I_{opt} : optimum light intensity, I_{av} : average light intensity, K^*_s : light affinity constant (at $I = K^*_s$, μ is not μ_{max} /2), (Ks, I_K, K): light saturation constant (at $I = Ks$, I_K, K, $\mu = \mu_{max}$ /2), K_I : light inhibition constant, (n, a, b, c, K_{CI}, K_1, K_2): constants, η: effective light coefficient.

SN	Model structural form	Equations	Reference
1	Linear	$\mu(I) = \mu_{\max} \cdot \frac{I}{K^*_S}$	[78,79]
2	Quadratic	$\mu(I) = \mu_{\max} \cdot \frac{I}{K^*_S} \cdot \left(1 - \frac{I}{4K^*_S}\right)$	[78,80]
3	Exponential	$\mu(I) = \mu_{\max} \cdot \frac{I}{K^*_S} \cdot \exp\left(1 - \frac{I}{K^*_S}\right)$	[78,81]
		$\mu(I) = \mu_{\max} \cdot \left(1 - \frac{2}{\exp\left(2 \cdot \frac{I}{K^*_S}\right) + 1}\right)$	[78,80]
		$\mu(I) = \mu_{\max} \cdot \left(1 - \exp\left(-\frac{I}{K^*_S}\right)\right)$	[78,82]
4	Power	$\mu(I) = \mu_{\max} \cdot \frac{I^n_{av}}{I^n_K + I^n_{av}}$	[26,83–85]
		$\mu(I) = \mu_{\max} \cdot \frac{I^n_{av}}{I^n_K + I^n_{av}} - \lambda$	[26,86]
		$\mu(I) = \mu_{\max} \cdot$	[26,84]

		$\mu(I) = \mu_{\max} \cdot \frac{I_{\mathrm{av}}^{\left(\frac{\mathrm{n}_2}{I_0}\right)}}{\left[K_{\mathrm{I}} \cdot \left(1 + \left(\frac{I_0}{K_{\mathrm{I}}'}\right)^{\mathrm{n}_1}\right)\right]^{\left(\frac{\mathrm{n}_2}{I_0}\right)} + I_{\mathrm{av}}^{\left(\frac{\mathrm{n}_2}{I_0}\right)}}$	[26,86]
		$\mu(I) = \mu_{\max} \cdot \frac{I_{\mathrm{av}}^{\left(\frac{\mathrm{n}_2}{I_0}\right)}}{\left[K_{\mathrm{I}} \cdot \left(1 + \left(\frac{I_0}{K_{\mathrm{I}}'}\right)^{\mathrm{n}_1}\right)\right]^{\left(\frac{\mathrm{n}_2}{I_0}\right)} + I_{\mathrm{av}}^{\left(\frac{\mathrm{n}_2}{I_0}\right)}} - \lambda$	[83,85]
		$\mu(I) = \mu_{\max} \cdot \frac{I_{\mathrm{av}}^{\left(\mathrm{b}+\frac{\mathrm{c}}{I_0}\right)}}{\left[K_1 \cdot \left(1 + \left(\frac{I_0}{K_2}\right)^{\mathrm{a}}\right)\right]^{\left(\mathrm{b}+\frac{\mathrm{c}}{I_0}\right)} + I_{\mathrm{av}}^{\left(\mathrm{b}+\frac{\mathrm{c}}{I_0}\right)}}$	
5	Hyperbolic	$\mu(I) = \mu_{\max} \cdot \frac{I}{I + K_{\mathrm{S}}}$	[78,87]
		$\mu(I) = \mu_{\max} \cdot \frac{I}{\left(I^2 + K_{\mathrm{S}}^{*2}\right)^{0.5}}$	[78,88]
		$\mu(I) = \mu_{\max} \cdot \frac{I}{I + K_{\mathrm{S}} + \frac{I^2}{K_{\mathrm{I}}}}$	[78,83,86,89]
		$\mu(I) = \mu_{\max} \cdot \frac{I_{\mathrm{av}}}{K_s + I_{\mathrm{av}} + \frac{I^2}{K_{\mathrm{I}}}}$	[84]
		$\mu(I) = \mu_{\max} \cdot \frac{I}{I + K_{\mathrm{S}} + \frac{I_{\mathrm{av}}^2}{K_{\mathrm{I}}'}} - \lambda$	[15,84]
		$\mu(I) = \mu_{\max} \cdot \frac{I}{(I^{\mathrm{n}} + K_{\mathrm{S}}^{*\mathrm{n}})^{\frac{1}{\mathrm{n}}}}$	[78,83,90]
		$\mu(I) = \mu_{\max} \cdot \frac{I}{(I^{\mathrm{n}} + K_{\mathrm{S}}^{*\mathrm{n}})^{\frac{1}{\mathrm{n}}}} - \mathrm{m}$	[78,91]
		$\mu(I) = \mu_{\max} \cdot \frac{I}{I + \mathrm{K}_{\mathrm{S}}^{*} \cdot \left(\frac{I}{I_{\mathrm{opt}}} - 1\right)^2}$	[78,92]
		$\mu(I) = \mu_{\max} \cdot \frac{I - K_{CI}}{I + K_{\mathrm{CI}} + K_{\mathrm{S}} - K_{CI}}$	[78]
		$\mu(I, \eta) = \mu_{\max} \cdot \frac{I}{I\left(\frac{1}{\eta}\right) + K_{\mathrm{S}} + \frac{I^2}{K_{\mathrm{I}}\left(\frac{1}{\eta}\right)}}$	in this work [52]

6	Hyperbolic tangent	$\mu(I) = \mu_{\max} \cdot \tanh\left(\frac{I}{K_I}\right)$	[26,84,93]

Unlike typical Type II models, Type III models generally describe the photosynthetic rate by accounting for both the light gradient and L/D cycles experienced by the individual microbial cells within the PBR as stated by Bechet et al., and Kroumov et al., [26,84] and are timely reviewed in Figure 2.6. As seen, they are mechanistic models based on the concepts of photosynthetic units (PSUs): the simplest functional unit of the photosynthetic apparatus as defined by Papadakis et al., and Han [94,95]. This enables researchers to formulate different hypothesis around the PSUs with mostly 3 or 4 states being featured in different published model structures. For instance, the most widely revisited model in literature is the three state model according to Eilers and Peeters [29] which is summarised in Eqs. (2.6) to (2.9) and forms the backbone from which most of the variant PSU models in Figure 2.6 were constructed. The model assumes the PSUs in the inactive/resting/open state (x_1) to be paused but moves upon activation via the absorption of photons into the active/excited/closed state (x_2). In the active state they can either utilise the absorbed energy to start photo-production, and then return to the inactive state (x_1) or absorb an extra photon becoming inhibited (x_3). Finally, the PSUs in the inhibited state can recovery back to the inactive state [26,29,95]. Hence, the rate of change for these states are respectively described by the ordinary differential equations: Eqs. (2.6) to (2.8).

$$\frac{dx_1}{dt} = -\alpha I x_1 + \gamma x_2 + \sigma x_3 \tag{2.6}$$

$$\frac{dx_2}{dt} = \alpha I x_1 - \gamma x_2 - \beta I x_2 \tag{2.7}$$

$$\frac{dx_3}{dt} = \beta I x_2 - \sigma x_3 \tag{2.8}$$

With unity probability of states as defined in Eq. (2.9).

$$x_1 + x_2 + x_3 = 1 \tag{2.9}$$

Together with the microbial specific growth rate being directly proportional to PSUs in the active state as expressed in Eq. (2.10) and κ being the constant of proportionality.

$$\mu = \kappa \gamma x_2 \tag{2.10}$$

Whereby the light dependent reactions are characterised by the rate constants (α, and β) which are 1st order with respect to the absorbed light intensity. Similarly, the dark reactions are characterised by the rate constants (γ and σ) which are 0th order with respect to the light intensity.

$$\mu = \kappa\gamma x_2 - Me \tag{2.11}$$

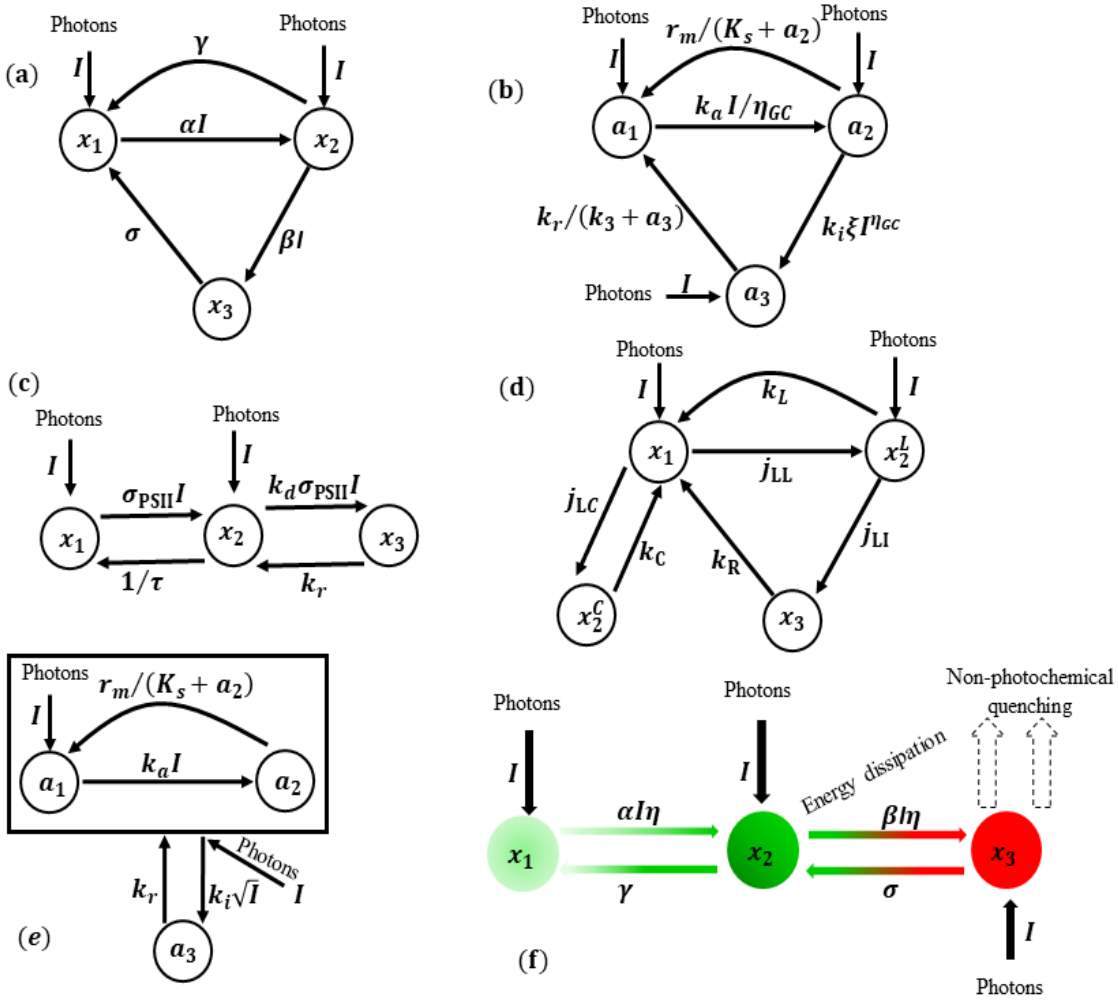

Figure 2.6: Schematic diagrams of the PSU model and variants adapted from Gao et al. [16]: (a) Eilers-Peeters model [29] with x_1, x_2, and x_3 representing the PSU in inactive, active and inhibited states respectively; (b) the Garcia Camacho et al., model [38]; (c) the Han model [95–97] and Nikolalou model [39,98]; (d) the Papadakis et al. model [94]; (e) the Camacho Rubio et al. model [99] and similarly the Bernardi model [100] with a_1, a_2 and a_3 representing the PSU in inactive, active and inhibited states respectively; (f) the Anye Cho et al. model [52] in this work with η denoting the *effective light coefficient*.

To incorporate more physics, some of the literature modifications and advancement of the original three state model by Eilers-Peeters [29] include: (i) the incorporation of a maintenance term (i.e., Me) in Eq. (2.10) leading to Eq. (2.11) by Wu and Merchuk [101] to account for the negative photosynthesis rate at relatively low or no light intensity as a result of metabolic aspiration, widely accepted and used in other studies, for example Gao et al., and Bernardi et al. [16,100]; (ii) the 0^{th} and 1^{st} order reactions with respect to light intensity for the dark reactions (i.e., γ) and photoinhibition (i.e.,βI) were reformulated as enzyme-

mediated process obeying Michealis-Menten kinetics for the former (i.e., ., $\gamma = \frac{r_m}{(k_s+a_2)}$) and a square root dependence to light intensity for the later (i.e., $\beta I = k_i\sqrt{I}$) by Camacho Rubio et. al. [99], also widely implemented in other studies, for example Garci-Camacho et al., and Bernardi et al. [38,100]; (iii) the incorporation of effective absorption cross-section of PSUs (i.e., σ_{PSII}) and the turn over time (i.e., τ) for electron transfer chain from the water donor side of PSII to terminal electron acceptors by Han [95], as well widely utilised in other studies [96–98]; and most recently (iv) embedding of an *effective light coefficient* (i.e., η) to account for the effects of culture mixing, thus L/D cycles by Anye Cho et. al. [52].

Whilst the aforementioned literature modifications and advancements (i.e., (i) to (iv)) led to a satisfactory micro-scale simulations by capturing the intracellular response to extracellular stimuli, the coupling of the first-three (i.e., (i) to (iii)) models to macro-scale hydrodynamic simulations for the PBR's engineering upscaling investigations poses significant numerical and bio-physical challenges. All these shall be reviewed separately under Section 2.3.4.

2.3.2 Modelling the influences of temperature

Temperature is an environmental culturing parameter which is well known to affect the growth and secondary metabolite production of photosynthetic microorganisms via their enzymatic, metabolic and electron transport efficiencies. When cultivated at appropriate temperatures, the microbial growth and secondary metabolite products are promoted, whereas at a high temperature, the microbial growth and secondary metabolite productions would decrease primarily due to the denaturing of essential proteins/enzymes in addition to inhibitory effects on microbial cellular physiology as stated by Yen et al., [46]. However, only a handful of studies have been reported in literature, as tabulated in Table 2.5, investigating the temperature effects on the stoichiometric coefficients of mathematical models like specific growth rate, specific decay rate, and yield coefficients, just to name a few. The models in Table 2.5 can be broadly categorised into Arrhenius-type models and statistical-type models whereby the former is often preferred due to its better mechanistic interpretation and knowledge, thus ranked top on the list (i.e., **SN**:1 to 4). Hence, the latter is not of interested to this PhD research and was therefore not reviewed further. Since most literature studies featured the first-three Arrhenius-type models on Table 2.5, they were further discussed due to their relevance to this PhD research.

Starting with Table 2.5's SN. 1, the model assumes an exponential increase of the microbial growth rate with rising temperature. Although very reliable at sub optimal temperature conditions, the model fails once the cultivating temperature increases and exceeds the

microorganism's optimum temperature. Since it cannot represent the decrease in growth rates at higher temperatures beyond the optimal culturing temperature like models of SN. 2 and 3 in Table 2.5. A common term between SN. 2 and 3, is the $A_2 \cdot \exp\left(-\frac{E_{a2}}{RT}\right)$ representing the deceleration of $\mu(T)$ at increasing T beyond the optimal T whereby A_2 (h^{-1}) and E_{a2} (J mol^{-1}) are the pre-exponential factor and activation energy for thermal denaturing processes respectively.

Table 2.5: Literature review of temperature model structures with either activating and/or deactivating effects. Whereby $\mu(T)$: growth rate dependence on temperature, μ_{max}: maximum specific growth rate, A and A_1: pre-exponential factor, A_2: post-exponential factor, E_a and E_{a1} : activation energy, E_b and E_{b2} : de-activation energy, R: universal gas constant and T: absolute temperature, T_{min}: minimum temperature, T_{max}: maximum temperature, T_{opt}: optimum temperature, b_1,b_2, and C_2: model constants.

SN	Temperature model	Reference
1	$\mu(T) = A \cdot \exp\left(-\frac{E_a}{RT}\right)$	[102]
2	$\mu(T) = A_1 \cdot \exp\left(-\frac{E_{a1}}{RT}\right) - A_2 \cdot \exp\left(-\frac{E_{a2}}{RT}\right)$	[102–104]
3	$\mu(T) = \frac{A_1 \cdot \exp\left(-\frac{E_{a1}}{RT}\right)}{1 + A_2 \cdot \exp\left(-\frac{E_{a2}}{RT}\right)}$	[26,102]
4	$\mu(T) = \exp\left(-\left(\frac{E_a}{RT} - \frac{E_a}{RT_a}\right)\right) - \exp\left(-\left(\frac{E_b}{RT} - \frac{E_b}{RT_b}\right)\right)$	[105]
5	$\mu(T) = \frac{(T - T_{max})(T - T_{min})^2}{(T_{opt} - T_{min})} \cdot \frac{1}{\left((T_{opt} - T_{min})(T - T_{opt}) - (T_{opt} - T_{max})(T_{opt} + T_{min} - 2T)\right)}$	[26]
6	$\mu(T) = \mu_{max} \cdot \exp\left(\frac{-(T - T_{opt})^2}{2\sigma^2}\right)$	[106,107]
7	$\mu(T) = \left(b_1(T - T_{min})\right)^2$	[108]
	$\mu(T) = \left(b_2(T - T_{max})\left[1 - \exp\left(C_2(T - T_{max})\right)\right]\right)^2$	

Having highlighted the pros and cons of each Arrhenius-type models, it is important to mention that the choice of one over another is mostly subjective and context-dependent: (i) available operating temperature conditions, (ii) type of mathematical model construction (i.e., static vs dynamic), and (iii) methodology of parameter estimation and software solvers. These aspects were further exploited in Chapter 4 of this PhD thesis.

2.3.3 Modelling the influences of light intensity, light attenuation, and temperature on secondary metabolite production

As the previous two sub sections of Chapter 2 already reviewed the effects of light intensity and light attenuation as $\mu(I)$, and effects of temperatures as $\mu(T)$, on the microbial growth, this sub section considers the combined effects of $\mu(I,T)$ on the microorganism's secondary metabolite productions. Generally, the formation of microbial secondary metabolite products are expressed by the specific product formation rate, α_{prod} which is dependent on whether the bioproduct is: (i) growth associated, if its production rate is directly proportional to the cell growth rate (i.e. $\alpha_{\text{prod}} = \alpha_p \cdot \mu$), ii) non growth associated, if it is produced at a constant rate during the stationary phase of the cell growth curve (i.e. $\alpha_{\text{prod}} = \beta_p$), or iii) mixed growth associated, if its production occurs during both linear (i.e. (i)) and stationary (i.e., (ii)) growth phases.

A review of the various structural forms of the secondary metabolite production models are presented in Table 2.6 such that if $\alpha_p = 0$, the bioproduct formation is non-growth associated, if $\beta_p = 0$), the bioproduct formation is growth-associated and if both are non-zero (i.e., $\alpha_p, \beta_p \neq 0$), the bioproduct formation is mixed growth-associated.

Table 2.6: Review of published secondary metabolite production model structures.

SN	Model type	Equations	Reference
1	Growth associated	$\alpha_{\text{prod}} = \alpha_p \cdot \mu$	[109]
		$\alpha_{\text{prod}}(I) = \alpha_p \cdot \mu(I)$	[110]
		$\alpha_{\text{prod}}(I,T) = \alpha_p \cdot \mu(I) \cdot \mu(T)$	[105]
2	Non growth associated	$\alpha_{\text{prod}} = \beta_p$	[109]
		$\alpha_{\text{prod}}(I) = \beta_p(I)$	n/a
		$\alpha_{\text{prod}}(I,T) = \beta_p(I,T)$	n/a
3	Mixed growth associated	$\alpha_{\text{prod}} = \alpha_p \cdot \mu + \beta_p$	[35,60]
		$\alpha_{\text{prod}}(I) = \alpha_p \cdot \mu(I) + \beta_p(I)$	n/a

$\alpha_{\text{prod}}(I,T) = \alpha_p \cdot \mu(I) \cdot \mu(T) + \beta_p(I,T)$	in this work [2]

n/a: not available

As seen in Table 2.6, mathematical models accounting for the combine light intensity, light attenuation, and temperature effects on the stoichiometric coefficients representing the growth and non-growth associated bioproduct formation rates of photosynthetic microorganisms were previously not available (i.e., n/a) until realised in this PhD research by Anye Cho et al., [2]. The mathematical derivation, model parameter estimations, and prediction validations for the modelling of biohydrogen production by the photosynthetic bacterium *Rhodopseudomonas palustris* was thoroughly dealt with in Chapter of 4 of this PhD thesis.

2.3.4 Light attenuation simulation in photobioreactors

Under the special considerations of fixed abiotic factors and well mixed PBR systems, the photosynthetic microbial growth rate becomes a function of the transmitted local light intensity regimes to which the microbial cells are subjected to, inside the PBR. This phenomenon is characterised by several parameters including: (i) microbial cell morphology - cell diameter and shape, (ii) microbial cell concentration, (iii) PBR light-path length, (iv) cell pigment fractions, (v) bubbles if present, and (vi) the PBR wall properties [3,83,111,112]. Therefore, these factors must be incorporated into the mathematical models aimed at the robust PBR design, upscaling to industrial scale PBR systems, as the appropriate intensity, duration, and wavelength of light must be supplied. As a result, different numerical methods and sub models has been proposed in literature studies, ranging from the most complex (solving radiation transport equations), to the simplest (empirical Beer-Lambert Law and its variant). These methods are reviewed below:

2.3.4.1 Radiation transport equation (RTE)

The complete radiation transport equation (RTE) for an absorbing, emitting, and scattering medium at position $\boldsymbol{r}$ in the direction $\boldsymbol{s}$ is governed by Eq. (2.12). Without simplifications, the RTE equation is too complex to be solve together with dynamic cell growth kinetics, thus only a handful of literature studies have numerically solved the complete RTE in commercial Partial Differential Equation (PDEs) software like ANSYS-Fluent [3,31,112–115]. Although the studies achieved superior results in comparisons to studies not solving RTE, the computational expense of the methodology was prohibitively high. Hence, it is therefore computationally infeasible to simulate larger scale PBRs (i.e., pilot plant to industrial scale) for dynamic optimisation. These disadvantages are the main motivations paving the way forward for the utilisation of sub RTE models (i.e., Two-flux approximation,

Beer-Lambert model, and variants) which fairly approximates the complete RTE but are computational efficient (i.e., Computational Fluid Dynamics (CFD) -friendly) to be exploited for the PBR designs, optimisation and upscaling. Hence, they are subsequently reviewed.

$$\frac{dI_\lambda(\boldsymbol{r},\boldsymbol{s})}{ds} + \left(a_\lambda + \sigma_{\lambda,s}\right)\cdot I_\lambda(\boldsymbol{r},\boldsymbol{s}) = \frac{a_\lambda \cdot n^2 \cdot \sigma \cdot T^4}{\pi} + \frac{\sigma_{\lambda,s}}{4\pi} \times \int_0^{4\pi} I_\lambda(\boldsymbol{r},\boldsymbol{s_i}) \cdot \Phi_\lambda \cdot (\boldsymbol{s_i},\boldsymbol{s}) \cdot d\Omega_i \quad (2.12)$$

Where $I_\lambda(\boldsymbol{r},\boldsymbol{s})$ represents the wavelength (λ) radiation intensity, in the light path direction $\boldsymbol{s}$, and position vector $\boldsymbol{r}$, wavelength dependent absorption coefficient a_λ, light path length $\boldsymbol{s}$, scattering direction $\boldsymbol{s_i}$,wavelength dependent scattering coefficient $\sigma_{\lambda,s}$, refractive index n, Stefan-Boltzmann constant σ, local temperature T, and solid angle $d\Omega_i$.

2.3.4.2 Two flux approximation model

Unlike the complete RTE model, there is a significant decrease in computational expense with using the two-flux approximation model proposed by Cornet et al., [116] as reported in Eq. (2.13). The model accounts for both the cell absorption and scattering phenomena for highly dense microbial cultures within PBRs and has been used in several studies where the cell scattering effects cannot be neglected [3,116,117]. However, experimentally measuring the cell mass scattering coefficient is somehow challenging and for some special scenarios where its contributions are minimal, that is $\alpha_1 = 1$ and $E_s = 0$, Eq. (2.13) reverts into the classical Beer-Lambert law (i.e., Eq. (2.14)).

$$\frac{I(z)}{I_0} = \frac{4 \cdot \alpha_1}{(1+\alpha_1)^2 \cdot \exp^{\alpha_2} - (1-\alpha_1)^2 \cdot \exp^{-\alpha_2}} \quad (2.13)$$

Where $\alpha_1 = \sqrt{E_a/(E_a+E_s)}$, $\alpha_2 = \alpha_1 \cdot X_b \cdot z \cdot (E_a + E_s)$, with E_a and E_s being the mass absorption and scattering coefficient respectively [118].

2.3.4.3 The Beer-Lambert law and its variants

The Beer-lambert law remains the most widely used light transfer model in literature because of its simplicity and accuracy in describing the physics of light attenuation in PBRs due to microbial cell absorption as stated in Eq. (2.14) [3,49,65,77,83,111].

$$I(z) = I_0 \cdot \exp^{-K_0 \cdot Z} \quad (2.14)$$

Where $I(z)$ and I_0 represents the local and incident light intensity respectively, the overall spectral attenuation coefficient, $K_0 = K_b \cdot X_b + K_w$, K_b and K_w being the microbial and water mass extinction coefficients while X_b and z are the microbial biomass concentration and light path length respectively.

This empirical Beer-lambert law is valid for only (i) monochromatic and collimated light, (ii) well-mixed and transparent medium, and (iii) no light scattering as reported by Krujatz et al., and Cornet et al., [67,116]. However, this is not always the case in PBRs especially when the cell biomass concentration exceeds 1.0 gL^{-1} and the light attenuation coefficient K_0 is reported by Suh-Lee [119] to deviate from linearity with cell biomass concentration. Hence, variants of the Beer-Lambert law have been proposed in literature with K_0 having a hyperbolic correlation as seen in Krujatz et al. and Suh-Lee [67,119] with Eq. (2.15) whereby K_{max} and K corresponds to the maximum possible attenuation and constant respectively.

$$K_0 = \frac{1}{z} \cdot \frac{K_{max} \cdot X_b}{K + X_b} \tag{2.15}$$

Even so, the model does not account for light scattering effects which is often significant in PBRs harbouring gas bubbles. To incorporate this into the Beer-Lambert law for sparging PBRs, a variant model was published in the works of Zhang et al., [105,120] as seen in Eq. (2.16) which accounted for light scattering by gas bubbles within the PBR. These modifications were found to produce satisfactory predictions for the modelling of a wide range of biomass concentrations in PBRs, thus adopted in Chapter 3 of this PhD thesis.

$$I(z) = I_0 \cdot \exp^{\left(-\left(\frac{3 \cdot \varepsilon}{d} + \tau \cdot X_b\right) \cdot z\right)} \tag{2.16}$$

Where ε is bubble (gas phase) volume fraction, and d is the bubble diameter (m) and τ is the light absorption coefficient (L g^{-1} m^{-1}).

2.4 Dynamic model parameter estimation

The constructed mathematical models as seen in Section 2.3 have several model parameters which must be identified for the accurate bioprocess simulations. Depending on how noisy the experimental data sets are, the estimation procedure is fundamentally based on the weighted least squares minimisation of the error between the model response and actual system's response as illustrated in Eq. (2.17a) to (2.17e). These equations (i.e., Eq. (2.17a) to (2.17e)) can be solved with derivative-based and derivative-free methods. Among the methods, derivative based approaches which compute the first and second order derivatives of the objective function with respect to the model parameter(s) are regarded as the most accurate and robust since the gradient information is preserved. Therefore, derivative based methods have been used for several dynamic parameter estimation studies of biokinetic mathematical models [35,121–126] and was exploited in Chapter 4 and 5 of this thesis. The approach decomposes the non-linear optimisation problem into four steps, namely (i) direct transcription (time-discretisation or orthogonal collocation [126]) of the differential systems of equations into algebraic equations, (ii) formulation of the objective function into standard

form, (iii) formulation of the barrier function and relaxation of the inequality constraints, and (iv) solving the algebraic system of equations for optimality while satisfying the constraints via an appropriate non-linear optimisation solver (e.g. interior point solver, IPOPT or APOPT[126]).

$$\min_{P} \Phi(\boldsymbol{P}) = \sum_{i=1}^{NP} \left(\frac{\hat{y}_i - y(t_i, \boldsymbol{P})}{\hat{y}_i} \right)^2 \cdot W_i \tag{2.17a}$$

Subject to:

$$\frac{d\boldsymbol{y}}{dt} = f(\boldsymbol{y}(t), P)\,, \qquad t \in [t_0, t_f] \tag{2.17b}$$

$$\boldsymbol{y}_{lb} \leq \boldsymbol{y} \leq \boldsymbol{y}_{ub} \tag{2.17c}$$

$$\boldsymbol{P}_{lb} \leq \boldsymbol{P} \leq \boldsymbol{P}_{ub} \tag{2.17d}$$

$$\boldsymbol{y}(t_0) = \boldsymbol{y}_0 \tag{2.17e}$$

Where $\boldsymbol{P}$ is a vector of parameters, NP is the number of experimental data points, y is dynamic model output, $\hat{y}_i$ is experimental data point at time instant t_i, W_i is a vector of weights for data point at time instant t_i, $\boldsymbol{y}$ is a vector of state variables (e.g., biomass concentration, substrate concentration and biohydrogen production), $\boldsymbol{y}_{lb}, \boldsymbol{y}_{ub}, \boldsymbol{P}_{lb}$ and $\boldsymbol{P}_{ub}$ are the lower and upper bounds for the state variables and parameters respectively, $\boldsymbol{y}_0$ is the initial concentration of the state variables.

The framework is summarised in Figure 2.7 whereby collocation transcription over finite difference method was used since it has been reported by Nicholas et al., [127] to produce a significantly more accurate algebraic approximation. The implementation is carried out in Pyomo.DEA and executed by: (i) breaking the continuous domain (i.e., $t \in [t_0, t_f]$) into $N - 1$ finite elements, (ii) using a polynomial function of order $K + 1$ to approximate the differential variable $y(t)$ over each profile i, (iii) defining the polynomial function using K collocation points as additional discretisation points within each finite element, and (iv) enforcing continuity at the boundaries of the finite elements over the differential variable, $y(t)$ [127]. This is illustrated bellow (see Eqs. (2.18b) to (2.18f)) for any given derivative function and associated constraints in the form of Eq. (2.16a) as published by Nicholson et al., [127].

$$\left(\frac{dy(t)}{dt}, f\big(y(t), \mu(t)\big) \right) = 0, \qquad t \in [0, T] \tag{2.18a}$$

The application of collocation description to Eq. (2.16a) is given by:

$$\left.\frac{dy}{dt}\right]_{t_{ij}} = \frac{1}{h_i}\sum_{j=0}^{K} y_{ij}\frac{dl_j(\tau_K)}{d\tau}, \quad K = 1, \dots K, i = 1, \dots., N-1 \tag{2.18b}$$

$$0 = g\left(\left.\frac{dy}{dt}\right]_{t_{ij}}, (y_{iK}, \mu_{iK})\right), \qquad K = 1, \dots K, i = 1, \dots., N-1 \tag{2.18c}$$

$$y_{i+1}, 0 = \sum_{J=0}^{K} l_j(1) y_{ij}\ , \qquad i = 1, \dots., N-1 \tag{2.18d}$$

Where $t_{ij} = t_{i-1} + \tau_j h_i, y(t_{ij}) = y_{ij}$, and the solution to $y(t)$ is interpolated as per Eqs. (2.18e) and (2.18f).

$$y(t) = \sum_{j=0}^{K} l_j(\tau) y_{ij}, \qquad t \in [t_{i-1}, t_i], \qquad \tau \in [0,1] \tag{2.18e}$$

$$l_j(\tau) = \prod_{K=0,\neq j}^{K} \frac{(\tau - \tau_K)}{(\tau_j - \tau_K)} \tag{2.18f}$$

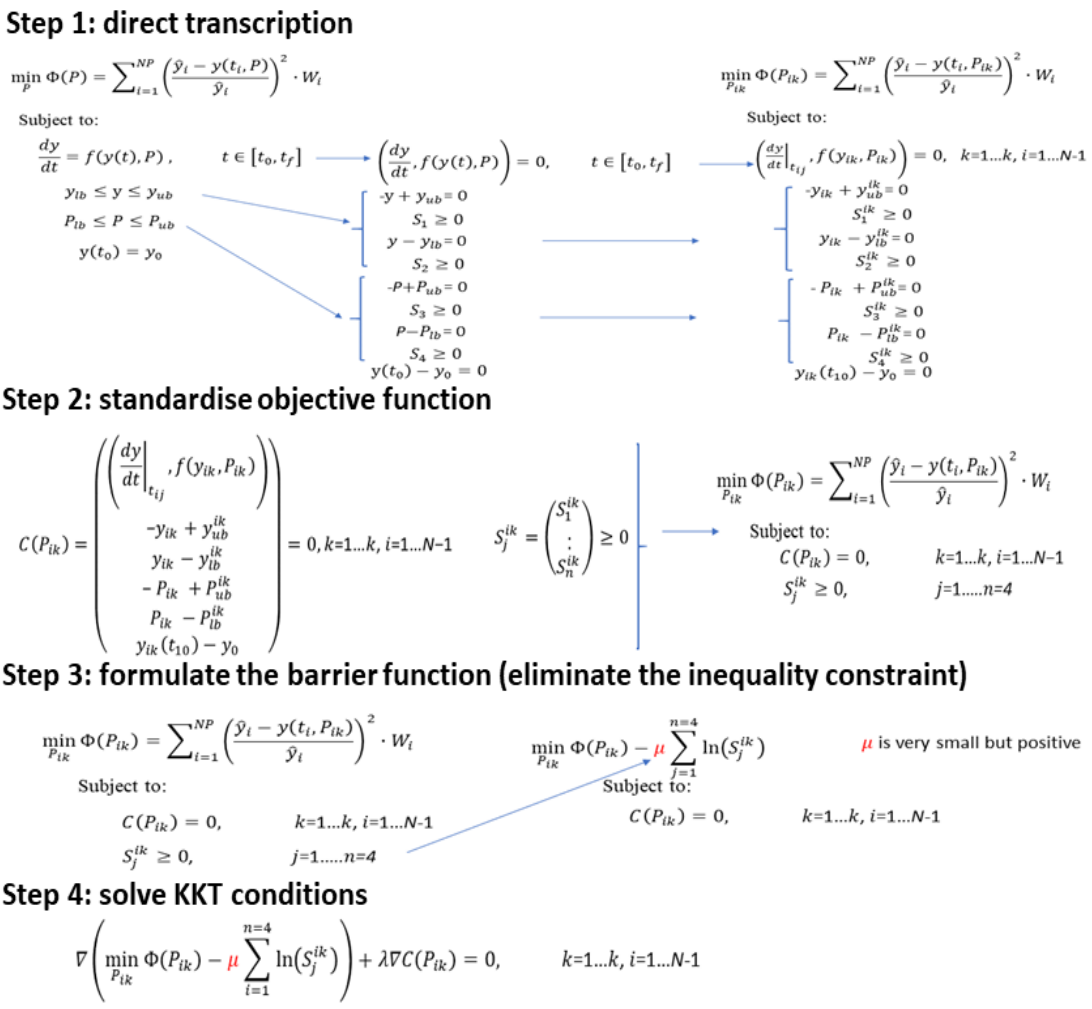

Figure 2.7: Summary of dynamic nonlinear programming (NLP) estimation framework with interior point solvers.

The resulting hundreds of thousands to millions of variables and constraints are then solved using interior point-based solvers such as IPOPT or APOPT. The solvers implement an active set strategy with a filter-based line-search that approaches the optimal solution from within the feasible region as illustrated in Figure 2.8.

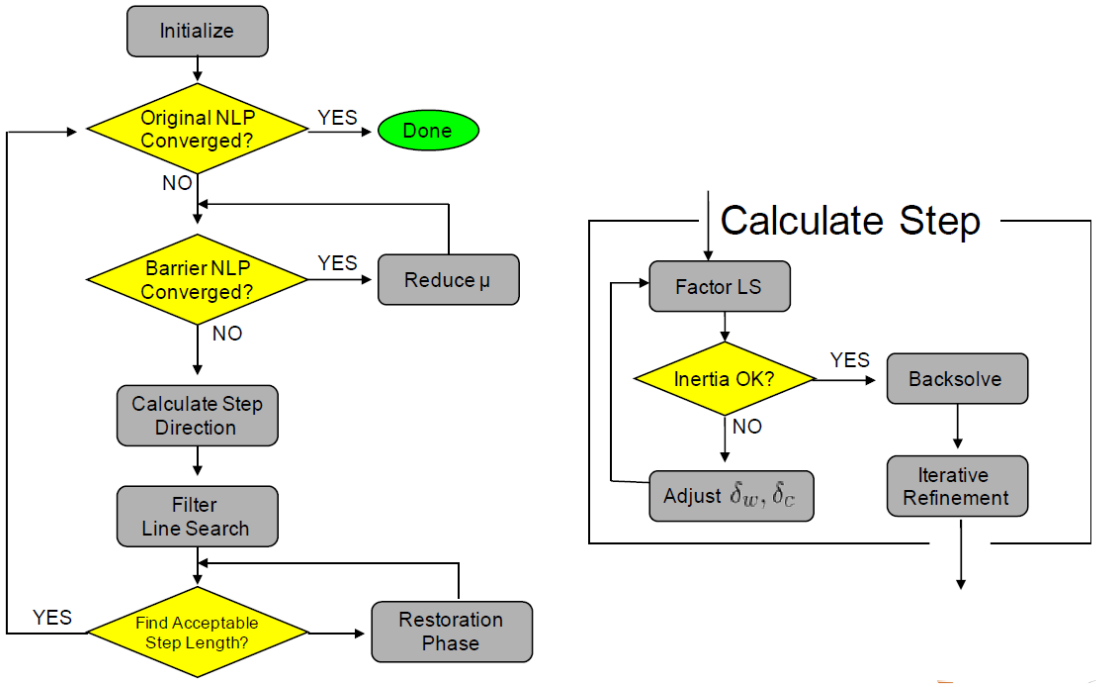

Figure 2.8: Schematic representation of the IPOPT algorithm flow sheet reproduced from Sandia National Laboratories [128].

However, whenever the constructed biokinetic models are too structurally complex, stiff, and multimodal in nature as seen in Chapter 3, the derivative-based approaches yield sub-optimal solutions. To guarantee global optimality, derivative-free methods which are broadly classified into evolutionary-based algorithms and swarm intelligence-based algorithms are often exploited to solve these non-linear optimisation problems. The former evolutionary-based algorithms are among the oldest in literature featuring Genetic Algorithms [129–131], Genetic Programming, for example Cheema et al., [132], Evolutionary Strategy, for example Roubos et al., [133] and Evolutionary Programming, for example Simutis et al., [134]. More recently, the latter swarm intelligence-based algorithms inspired by the collective behaviour of social insect in their colonies and other animal societies, have been developed and are attracting the interest of many research scientist. For example Particle Swarm Optimisation (PSO) [135,136], Artificial Bee Colony (ABC) [137], Artificial Ant Colony [138], to name a few. Among them, the PSO and ABC algorithms are the better algorithms employing fewer control parameters but capable of finding the near-optimal solutions of difficult optimisation problems. The reader is encouraged to revisit the

works of Karaboga-Akay [137] for a comprehensive literature on the individual algorithms as only a brief background has been provided herein. In PSO, the interacting agents are particles whose position correspond to a possible solution to the optimisation problem. The particles move in the search space upon updating their velocities (i.e., $\vec{v}(t)$) by following the current optimum particles (i.e., local best $\vec{p}(t)$) and changing their positions (i.e., $\vec{x}(t)$) at every time step *t*, to find the optima (i.e., global best $\vec{g}(t)$) as described in Eq.(2.19) to (2.21).

$$\vec{x}(t+1) = \vec{x}(t) + \vec{v}(t+1) \tag{2.19}$$

$$\vec{v}(t+1) = \omega\vec{v}(t) + \phi_1 \text{rand}(0,1)\big(\vec{p}(t) - \vec{x}(t)\big) + \phi_2 \text{rand}(0,1)\big(\vec{g}(t) - \vec{x}(t)\big) \tag{2.20}$$

$$\vec{v}_{min} \leq \vec{v}(t) \leq \vec{v}_{max} \tag{2.21}$$

Whereby the parameter ω, is an inertia weight to control the magnitude of the old velocity during the calculation of a new velocity, whereas ϕ_1 and ϕ_2 regulates the significance of $\vec{p}(t)$ and $\vec{g}(t)$ respectively, and the velocity is constraint to $\vec{v}_{max}$ but randomly initialised within the bounds in Eq. (2.21) at the start.

As per ABC, the position of a food source represents a possible solution to the optimisation problem meanwhile the nectar amount of that food source corresponds to the quality (fitness) of that solution. By using bees of three categories, namely employed bee, onlooker bee, and scout bee, as the interacting agents, the algorithm exploits their foraging abilities to memomerise local information and tests the nectar amount (fitness value) of new food sources (potential solutions). If the nectar amount of a food source is higher than that of the previous one, the bee memorises the position and forgets the old one, otherwise the positon of the previous one is retain in their memories. Starting by randomly generating the initial food source positions, x_i corresponding to the number of employed bees, SN (i.e., $x_i(i = 1,2, \ldots . SN)$), a new food source is chosen by an onlooker bee depending on the associated probability value, P_i with that food source as defined in Eq. (2.22). To forget the position of old food source in the bee's memory, new ones are explored with Eq. (2.23) whereby ϕ_{ij} is a random number in the range $[-1,1]$ and controls the production of new neighborhood food source around x_{ij} by comparing two food source positions (i.e., x_{ij} and x_{kj}). Once the nectar of a food source is abandoned due to no improvements after a predetermined number of cycles (i.e., *limit for abandonment*), the scout bee discovers a new food source for replacement with Eq. (2.24). The ABC algorithm terminates after a predetermined number of repeated cycles.

$$P_i = \frac{fit_i}{\sum_{n=1}^{SN} fit_n} \tag{2.22}$$

$$v_{ij} = x_{ij} + \phi_{ij}(x_{ij} - x_{kj}) \tag{2.23}$$

$$x_i^j = x_{min}^j + \text{rand}[0,1](x_{max}^j - x_{min}^j) \tag{2.24}$$

Where fit_i is the fitness value of a solution i (i.e., amount of nectar in the food source position i), $k \in \{1,2,\ldots.SN\}$ and $j \in \{1,2,\ldots.D\}$ are randomly chosen indexes and D is a dimensional vector.

Table 2.7: The swarm intelligence-based algorithms implemented in the hybrid PSO-ABC algorithm adapted from the works of Karaboga-Akay [137].

Particle Swarm Optimisaion (PSO)	**Artificial Bee Colony (ABC)**
1: Initialise population	**1:** Initialise population
2: **Repeat**	**2:** **Repeat**
3: Calculate fitness values of particles	**3:** Place the employed bees on their food sources
4: Modify best particles in the swarm	**4:** Place the onlooker bees on the food sources depending on their nectar amounts
5: Choose the best particles	**5:** Send the scouts to the search area for discovering new food sources
6: Calculate the velocities of particles	**6:** Memorise the best food source found so far
7: Update the particles positions	**7:** **Until** requirements are met
8: **Until** requirements are met	

Table 2.7 lists the pseudo codes of these swarm intelligence-based algorithms and Chapter 3 employs a combination of these two algorithms in a parallelised hybrid PSO-ABC algorithm as demonstrated in Figure 2.9. The strength of the proposed hybrid PSO-ABC algorithm lies in its ability to penalise the premature convergence of the PSO algorithm, a major literature limitation as stated in the works of Diogo et al., [136] by utilising the explorative characteristics of ABC to further explore the search space of worse inputs, thus finding potentially good solutions for the model parameters of the proposed highly non-linear multiscale photo-bioreactive transport model.

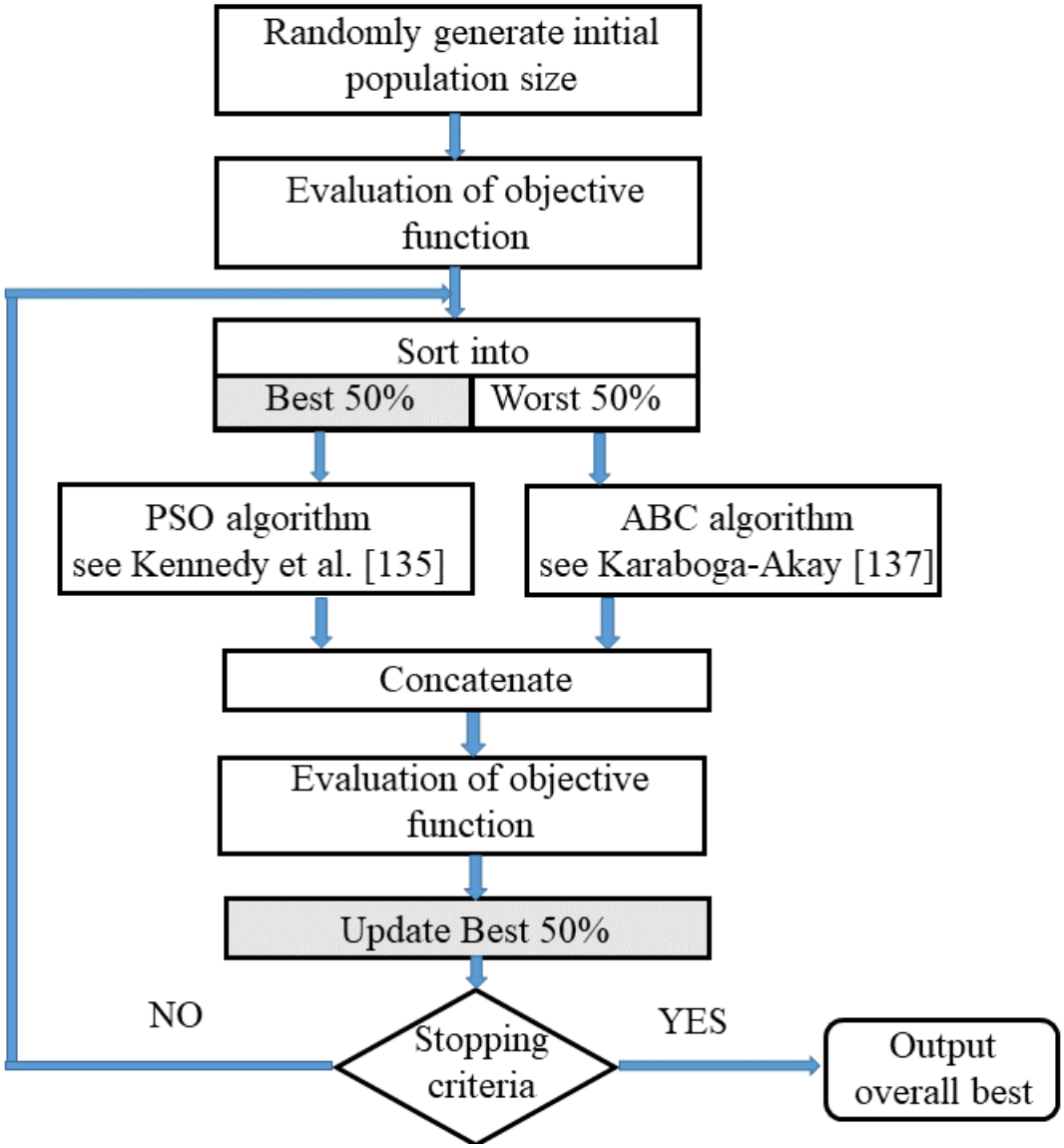

Figure 2.9: Hybrid hybrid PSO-ABC swarm intelligence-based algorithm.

2.5 Mathematical modelling of photobioreactor fluid dynamics

The mathematical modelling of photobioreactor fluid dynamics is achieved in a separate discipline called Computational Fluid Dynamics (CFD) which merges the theories of (i) fluid mechanics, (ii) mathematics (i.e., fundamental governing equations for the conservations of mass, momentum, and energy), and (iii) computer science (i.e., software tools e.g., solvers, pre and post processing utilities) as per the book of Versteeg-Malalasekera [139]. This methodology presents a powerful numerical tool for solving and obtaining approximate solutions (i.e., qualitative predictions) for complicated photobioreactor fluid flow, heat and mass transfer, reaction kinetics, and other related phenomena which cannot be done experimentally or analytically. As a result, CFD has been widely implemented in literature to study PBR fluid flows since satisfactory mixing conditions can minimise temperature and nutrient gradients, enhance gas-liquid mass transfer, maintain microbial

cells in free suspension (i.e., prevent sedimentation) and decrease the cell mutual shading phenomena. Therefore, the simulations of photobioreactor hydrodynamics, and turbulences are briefly reviewed herein in the subsequent two sub-chapters.

2.5.1 Photobioreactor hydrodynamic simulations

The commonly used methodologies for PBR hydrodynamic simulations in CFD solvers include (i) Volume of Fluid (VOF), (ii) Eulerian-Lagrangian, and (iii) Eulerian-Eulerian as reviewed by Gao et al., and Versteeg-Malalasekera [16,139]. Beginning with the VOF methodology, they are mainly applied for the modelling of immiscible fluid systems whereby there's a defining interface separating the individual fluids, for example, between atmospheric air and culture media. For this reason, they are particularly attractive for the modelling of open PBR systems (see Figures 2.2 and 2.3) whereby a single set of momentum equations are solved and then the volume fraction of the individual fluids through the domain are tracked. Since this work focuses on closed PBR systems, the VOF method was therefore not reviewed further.

Now looking at the Eulerian-Lagrangian (E-L) approach, it treats the primary phase (e.g., liquid/water phase) as a continuum and solves the Navier-Stokes equations, while particle tracking is used to solve for the secondary phase (e.g., gas phase) by tracking large number of gas bubbles for gas-liquid multiphase flows. The E-L approach allows for the primary and secondary phase interaction via the exchange of mass, momentum, and energy. Therefore, the E-L approach is attractive for the modelling of both open and closed PBR systems and has been used to study liquid-gas flows in several photobioreactors [15,28,49,140,141]. However, the E-L approach is limited by its prohibitively high computational expense associated to the computation of thousands of particle trajectories over a sufficient long time. For this reason, the Eulerian-Eulerian (E-E) approach is an appealing alternative due to the reduced computational resource requirements. Unlike E-L, the E-E approach treats both primary and secondary phases as interpenetrating continuums, and continuum equations are solved for both phases with an appropriate interaction between them. As a result, it has been widely implemented in the literatures [20,27,52,57,142] to obtain approximate solutions to the general mass (Eq. (2.25)), momentum (Eq. (2.26)), and species transport equations (Eq. (2.27)) as stated below:

$$\frac{\partial}{\partial t}(\alpha_k \rho_k) + \nabla \cdot (\alpha_k \rho_k \boldsymbol{u}_k) = S_{pk} \tag{2.25}$$

$$\frac{\partial}{\partial t}(\alpha_k \rho_k \boldsymbol{u}_k) + \nabla \cdot (\alpha_k \rho_k \boldsymbol{u}_k \boldsymbol{u}_k) = -\alpha_k \nabla p + \nabla \cdot \left(r_k \mu_{k,e} \left[\nabla \boldsymbol{u}_k + (\nabla \boldsymbol{u}_k)^T - \frac{2}{3} \mathrm{I} (\nabla \cdot \boldsymbol{u}_k) \right] \right) + \rho_k \alpha_k \boldsymbol{g} + \boldsymbol{F}_{lk} \tag{2.26}$$

$$\frac{\partial}{\partial t}\left(\alpha_k \rho_k Y_k^i\right) + \nabla \cdot \left(\alpha_k \rho_k \boldsymbol{u}_k Y_k^i\right) = -\nabla \cdot \alpha \boldsymbol{J}_k^i + S_{pk}^i \tag{2.27}$$

Whereby the subscript $k = S, L, G$ stands for solid, liquid and gas phases for multiphase simulations. The $\alpha_k, \rho_k,$ and $\boldsymbol{u}_k$ terms correspond to the phase volume fraction, density, and velocity, respectively. S_{pk} is the source term mass transfer rate from phase p to phase k. The pressure and gravity force are represented as $p, \boldsymbol{g}$ respectively. $\mu_{k,e}$ is the effective viscosity which is a combination of molecular viscosity, $\mu_{k,m}$ and turbulent viscosity $\mu_{k,T}$ as reported by Gao et al., and Luo-Al-Dahhan [27,54] in Eq. (2.28). The interphase momentum forces are lumped in $\boldsymbol{F}_{lk}$ meanwhile Y_k^i is the mass fraction of the conversed species i. These interphase momentum forces can be decomposed into at least five independent interphase forces as presented by Gao et al., [27,56] in Eq. (2.29) corresponding to: drag ($\boldsymbol{F}_D$), lift ($\boldsymbol{F}_L$), virtual mass ($\boldsymbol{F}_{VM}$), wall lubrication ($\boldsymbol{F}_W$), and turbulent dispersion ($\boldsymbol{F}_T$), respectively. Among them, the drag effects are often more dominating in the literature as reported by Gao et al., and Luo-Al-Dahhan [27,54] and are accounted for with Eq. (2.30).

$$\mu_{k,eff} = \mu_{k,Lam} + \mu_{k,Turb} \tag{2.28}$$

$$\boldsymbol{F}_{lK} = \boldsymbol{F}_D + \boldsymbol{F}_L + \boldsymbol{F}_{VM} + \boldsymbol{F}_W + \boldsymbol{F}_T \tag{2.29}$$

$$\boldsymbol{F}_{l,k} = \boldsymbol{F}_D = \frac{3}{4} \frac{C_D}{d_b} r_G \rho_L |\boldsymbol{u}_G - \boldsymbol{u}_L| (\boldsymbol{u}_G - \boldsymbol{u}_L) \tag{2.30}$$

In Eq. (2.30), d_b is the gas bubble diameter while C_D is the drag coefficient required to calculate the drag $\boldsymbol{F}_D$. The Schiller-Naumann drag model (i.e., Eq. (2.31)) is among the widely used correlations in multiphase studies in bubble column PBRs as indicated by Luo-Al-Dahhan [54] and was adopted in Chapter 3 of this PhD thesis.

$$C_D = \frac{24}{Re_b}(1 + 0.15 Re_b^{0.678}) \tag{2.31}$$

Where the bubble Reynolds number Re_b, is defined as Eq. (2.32)

$$Re_b = \frac{\rho_L |\boldsymbol{u}_G - \boldsymbol{u}_L| d_b}{\mu_L} \tag{2.32}$$

The fluid flow and mixing regimes within these photobioreactors usually vary from laminar, to transitional, and turbulent regimes depending on the Reynolds number, Re ($\boldsymbol{u}L/v$ whereby $\boldsymbol{u}$ and L are the mean flow's velocity and characteristic length of scale, and v is the

kinematic viscosity) as defined in Versteeg-Malalasekera [139]. For low Re (< 2,000), the flow is laminar, with well-ordered movements and smooth sliding layers of fluid over other layers. Hence, the changes of velocity and pressure fields are smooth in both time and space thereby leading to a cancellation of the turbulent viscosity term (i.e., $\mu_{k,T} = 0.0$) as reported by Lapin et al., [143] in Eq. (2.28). This is further exploited in Chapter 5 for modelling the vertical tubular photobioreactor's single phase flow (i.e., $k = L$) with Eqs. (2.25) to (2.26) and scalar transport with Eq. (2.27).

However, in high Re (> 2,000), the flow develops chaotic and stochastic movements which are characterised by eddies and swirls. Under such transitional and turbulent regimes, the velocity and pressure fields changes rapidly with space and/or time leading to a non-zero turbulent viscosity term (i.e., $\mu_{k,T} \neq 0.0$) in Eq. (2.28). As consequence of these fluctuations, the flow fields experience additional stresses, the so-called Reynolds stresses as well-defined by Versteeg-Malalasekera [139]. This is derived by firstly decomposing the instantaneous fields as a sum of the mean and the fluctuating components, the former is denoted by an overbar $\bar{}$ and the latter by $'$ in Eqs. (2.33a) and (2.33b) in the so-called Reynolds decomposition as detailed by Versteeg-Malalasekera [139]. This is then embedded into the instantaneous continuity and momentum equations, followed by taking time average which then yields the time-averaged Navier-Stokes equations (i.e., Eqs. (2.34) to (2.35)) whereby the additional term in the momentum equation corresponds to the Reynolds stresses (i.e.,$-\rho\overline{\acute{\boldsymbol{u}}_\iota \acute{\boldsymbol{u}}_\iota}$) [139]. These represent the turbulent frictions in the flow which are caused by the mixing of the turbulent eddies. The modelling strategies to close the problem is therefore discussed below in the next sub-chapter.

$$\boldsymbol{u}_i = \bar{\boldsymbol{u}}_i + \acute{\boldsymbol{u}}_i \tag{2.33a}$$

$$\rho = \bar{\rho} + \acute{\rho} \tag{2.33b}$$

$$\frac{\partial \rho}{\partial t} + \frac{\partial}{\partial x_i}(\rho \bar{\boldsymbol{u}}_i) = 0 \tag{2.34}$$

$$\begin{aligned} &\frac{\partial}{\partial t}(\rho \bar{\boldsymbol{u}}_i) + \frac{\partial}{\partial x_j}(\rho \bar{\boldsymbol{u}}_i \bar{\boldsymbol{u}}_i) \\ &\qquad = -\frac{\partial \bar{\rho}}{\partial x_i} + \frac{\partial}{\partial x_j}\left[\mu\left(\frac{\partial \bar{\boldsymbol{u}}_i}{\partial x_j} + \frac{\partial \bar{\boldsymbol{u}}_i}{\partial x_i} - \frac{2}{3}\delta_{ij}\frac{\partial \bar{\boldsymbol{u}}_m}{\partial x_m}\right)\right] \\ &\qquad + \frac{\partial}{\partial x_j}\left(-\rho\overline{\acute{\boldsymbol{u}}_\iota \acute{\boldsymbol{u}}_\iota}\right) \end{aligned} \tag{2.35}$$

Where i=1, 2, 3 are the coordinate components.

2.5.2 Photobioreactor turbulence simulations

The Reynolds Averaged Navier-Stokes (RANS) as presented above considers the time-averaged properties of the flow as satisfactory and is often applied for most photobioreactor turbulent computations. This is due to superior computational cost saving in comparison to the literature counterparts: Numerical Simulations (DNS) and Large Eddy Simulation (LES) as reported by Versteeg-Malalasekera [139]. DNS approach resolves all the various scales of turbulence (i.e., big and small eddies) by directly solving the instantaneous Navier-Stokes equations meanwhile the LES approach resolves the behaviour of the larger eddies and then model the effects of the smaller ones [139]. As a result, the computational demand for DNS is prohibitively high whereas the computations and volume of storage for LES are still very large, thus they are unattractive for most photobioreactor turbulence computations. However, the appearance of extra terms in Eq. (2.35) of the RANS technique due to the interactions between various turbulent fluctuations are to be modelled with additional transport equations. Depending on the number of additional transport equations, the RANS turbulence models are classified into a family of models as tabulated in Table 2.8.

Table 2.8: Classification of turbulence calculation methodologies adapted from Versteeg-Malalasekera [139].

Number of additional transport equations	Name of model
0	Mixing length
1	Spalart-Allmaras
2	$k-\varepsilon$
2	$k-\omega$
2	SST
7	Reynolds stress

A recent review by Gao et al., [16] showed the family of models with 2 additional transport equations as the most widely used models for photobioreactor turbulence studies. Within the category, $k-\varepsilon$ and $k-\omega$ tops the list but $k-\varepsilon$ features in many more studies because of its simplicity and lesser computational resource requirements [16] and therefore of interest to this PhD research. As Chapters 3 utilises the RANS equations and $k-\varepsilon$ model for modelling the respective fluid flows and turbulence of a Flat-plate PBR, the formulations of $k-\varepsilon$ equations are therefore revisited herein. The model introduces the turbulent kinetic energy, K as a sum of the three fluctuating velocity components as defined in Eq. (2.36) and then models the turbulent kinetic energy (Eq. (2.37) with its dissipation rate, ε (Eq. (2.38))

as the two respective additional transport equations. This is then embedded into the turbulent viscosity $\mu_{k,T}$ in Eq. (2.28) via in Eq. (2.39).

$$K = \sqrt{\left(\overline{\acute{\boldsymbol{u}}^2} + \overline{\acute{\boldsymbol{v}}^2} + \overline{\acute{\boldsymbol{w}}^2}\right)} \tag{2.36}$$

$$\frac{\partial}{\partial t}(\alpha_k \rho_k K_k) + \nabla \cdot (\alpha_k \rho_k \boldsymbol{u}_k K_k) = \nabla \cdot \left(\alpha_k \left(\mu_{k,Lam} + \frac{\mu_{k,Turb}}{\sigma_K}\right) \cdot \nabla K_k\right) + \alpha_k (P_k - \rho_k \varepsilon_K) \tag{2.37}$$

$$\frac{\partial}{\partial t}(\alpha_k \rho_k \varepsilon_K) + \nabla \cdot (\alpha_k \rho_k \boldsymbol{u}_k \varepsilon_K) = \nabla \cdot \left(\alpha_k \left(\mu_{k,Lam} + \frac{\mu_{k,Turb}}{\varepsilon_K}\right) \cdot \nabla \varepsilon_K\right) + \alpha_k \frac{\varepsilon_K}{K_k} (C_{\varepsilon 1} P_k - C_{\varepsilon 2} \rho_k \varepsilon_K) \tag{2.38}$$

$$\mu_{k,Turb} = C_\mu \rho_k \left(\frac{K_k^2}{\varepsilon_K}\right) \tag{2.39}$$

Where C_μ, $C_{\varepsilon 1}$, $C_{\varepsilon 2}$, σ_K, and ε_K, are constants (see Table 2.9) meanwhile P_k is the turbulence production term for phase k.

Table 2.9: Values of the constants in the $k - \varepsilon$ model

C_μ	$C_{\varepsilon 1}$	$C_{\varepsilon 2}$	σ_K	ε_K	Reference
0.09	1.44	1.92	1.0	1.3	[20,49,144,145]

2.6 Multi-scale modelling of photobioreactor fluid dynamics and bioreactions

The (i) nanoscopic (or atomic) (~10^{-9} m), (ii) microscopic (~ 10^{-6} m), (iii) mesoscopic (~ 10^{-4} m), and (iv) macroscopic (~10^{-2} m) scales are the four distinguished scales in the context of numerical simulations as reviewed by Jebahi et al., [146]. Among these scales, multi-scale mathematical modelling of photobioreactors considers the engineering problem at the macroscopic scale (e.g., hydrodynamics, nutrients, cell growth and bioproduct formation, just to highlight a few) while considering the complexity of the microscopic scale (e.g., intracellular metabolic reactions, fluxes of light intensity and heat, just to highlight a few) with minimum simulation costs. A recent review of the comprehensive multi-scale coupling methodologies for photobioreactors by Gao et al., [16] categorised these methodologies into three main approaches: (i) Circulation time approach, (ii) Lagrangian simulation approach, and (iii) Eulerian simulation approach.

2.6.1 Circulation time approach

This strategy is different from the others as no hydrodynamic solver is used, instead the fluid flow patterns are assumed a priori. For instance, Eq. (2.40) was utilised by Wu and Merchuk [25] to describe the radial position of microbial cells within a bubble column photobioreactor as a cosine function of time. This was then coupled with the Beer-Lambert law to calculate the microbial cell light exposure history and then biomass growth within the PBR column. Similarly, the same authors applied this approach to approximate the liquid velocities of each region (riser, downcomer and separator) of an internal loop airlift PBR to calculate the algae biomass growth [24]. Even though satisfactory results were achieved in comparison with experimental data, the definition of circulation time was reported in the investigations of Gao et al., [16] to be physically unrealistic and difficult to estimate in photobioreactors with complex geometries and flow dynamics. Therefore, this approach is not suitable for the design applications and scale-up studies of industrial scale-PBRs. Consequently, the circulation time approach was not further reviewed

$$r = \frac{R}{2}\left(1 - cos\frac{2\pi}{T}t\right) \tag{2.40}$$

Where R is the column radius and T is the cycle time as obtained from a surface renewal model by Wu and Merchuk [25].

2.6.2 Lagrangian simulation approach

Just like the circulation time approach which focuses on the computation of microbial cell light exposure history, the Lagrangian simulation approach performs the same task with additional consideration such as (i) influences of the local fluid flow velocities on the particle position via Newton's law of motions, and (ii) incorporation of other interfacial forces such as drag, buoyancy, virtual mass, and lift. For example, Eq. (2.41) as defined in the works of Sato et al., [141] captures the drag force and additional particle acceleration as represented in the x-direction of a cartesian coordinate system.

$$\frac{d\boldsymbol{u}_p}{dt} = \boldsymbol{F_D} \cdot \left(\boldsymbol{u} - \boldsymbol{u}_p\right) + \frac{\boldsymbol{g}_x \cdot \left(\rho_p - \rho\right)}{\rho_p} + \boldsymbol{F_x} \tag{2.41}$$

whereby $\boldsymbol{u}_p$ and ρ_p are the particle velocity and density $\boldsymbol{F_D} \cdot \left(\boldsymbol{u} - \boldsymbol{u}_p\right)$ is the drag force per unit particle mass and $\boldsymbol{F_x}$ is an additional acceleration (force/unit particle mass) term [141].

As a result, the Lagrangian simulation approach has been widely used for both two and three phase Eulerian-Eulerian-Lagrangian simulations [15,28,49,141,147]. Although this approach produces satisfactory results when compared to experimental measurements, its major limitation arose from the enormous computational expense associated to the

computation of thousands of particle trajectories over a sufficient long time as reviewed by Gao et al., [16]. This is done to obtain statistically meaningful information for the cell light exposure history, but the high associated cost hinders their application for large scale PBR optimisation studies. Therefore, Lagrangian simulation approach was not adopted in this PhD research.

2.6.3 Eulerian simulation approach

The Eulerian simulation approach enables the decomposition of the comprehensive multi-scale coupling into a two-stage simulation: (i) computation of the velocity fields and turbulence distribution for the multiphase system till convergence, and (ii) using the hydrodynamic information from (i), together with light transport to compute the volume average biomass productivity of the Photobioreactor. This approach has been implemented by Gao et al., and Anye Cho et al., [27,52]. The major benefit of this approach is that a larger time step can be used for the second step (i.e., (ii)) simulations (up to 24 hrs in the paper of Amini et al., [142]) thereby minimising the computational expense over extended periods of simulation time. For this reason, the Eulerian simulation approach has been widely applied for several studies involving the coupling of macroscale (i.e., hydrodynamic) to models of similar scales (e.g., Type II biokinetic models [20,52,142]) or other scales. The other scale models features microscale biokinetic models like the Type III biokinetic models as per the works of Gao et al., [16,27,28,56] and Nauha and Aloaeus [57,148].

Among the hydrodynamic and Type III biokinetic model coupling studies, only few (less than 5 to the author's knowledge) features in literature. This reflects the difficulties of the implementation as these studies were realised within the last 7 years despite the fast pace development of this research area. The implementation formulates the specie transports equation (i.e., Eq. (2.27)) for each of the PSU states. By so doing, each PSU state is assigned convection and diffusion terms as illustrated in Eqs. (2.42) to (2.43) and then, the dry biomass concentration is externally computed with Eq. (2.45) as per the works of Gao et al., [27,56]. When applied to simulate the cultivation of the algae *Chlorella vulgaris* at different rotations per minutes (rpm) in a taylor vortex PBR, the approach yielded satisfactory results in comparison to 5 days experimental measured biomass concentration. However, the multi-scale coupling strategy was interpreted herein as (i) lacking theoretical support, and (ii) computationally expensive for large scale PBR simulation and optimisation. The former (i.e., (i)) assignment of convection and diffusion terms to the PSU states implies that they are in free suspension within photobioreactor and are outside of the microbial cell walls which defies biological laws. The latter (i.e., ii) external computations of dry biomass concentration implies no direct coupling between intracellular kinetics and fluid dynamics, which results

in a high computational cost for the valid smaller time step sizes, thereby severely limiting the applications in PBR design, optimisation and scale up.

$$\frac{\partial}{\partial t}(\alpha_s \rho_s x_1) + \nabla \cdot (\alpha_s \rho_s \boldsymbol{u}_s x_1) = -\nabla \cdot (\alpha_s \rho_s D_e \nabla x_1) + \alpha_s \rho_s (-\alpha I x_1 + \gamma x_2 + \sigma x_3) \tag{2.42}$$

$$\frac{\partial}{\partial t}(\alpha_s \rho_s x_2) + \nabla \cdot (\alpha_s \rho_s \boldsymbol{u}_s x_2) = -\nabla \cdot (\alpha_s \rho_s D_e \nabla x_2) + \alpha_s \rho_s (\alpha I x_1 - \gamma x_2 - \beta x_2) \tag{2.43}$$

$$D_e = D_{s,L} + \frac{\mu_t}{\rho_s Sc_t} \tag{2.44}$$

$$\frac{dX}{dt} = \bar{\mu} \cdot X \tag{2.45}$$

Where D_e is the effective turbulent diffusivity of the solid phase (microalgae), $D_{s,L}$ is the larmina difussivity of the solid phase, Sc_t is the turbulent schimdt number and $\bar{\mu}$ is the mean specific growth rate.

These simulation cost challenges motivated the development of a robust multi-scale coupling strategy with significant computational cost savings in Chapters 3 and 4 of this PhD thesis. For this, two advanced modelling techniques, namely (i) acceleration of growth kinetic, and (ii) parallel computing, are exploited within this PhD thesis to accelerate the simulation time without compromising the solution quality. The former technique considers the biokinetic model in Eq. (2.46) producing the typical sigmoid shape of bioprocesses in Figure 2.10 A) as scalable by two of its model parameters (i.e., μ_m and u_d). Therefore, by scaling these parameters with a factor (e.g., by 8640 as proposed in our works Anye Cho et al. [52]), the entire simulated bioprocess kinetics would be accelerated from a 6 days (144 hrs) simulation into a 60 s simulation without compromising the sigmoid shape as demonstrated in Figure 2.10 B). This technique presents a massive simulation cost reduction of the orders of months since the stage two Eulerian CFD photo-biokinetic simulation will be now performed for 60 s instead of the previously 6 days (144 hrs) computations. In addition, the latter parallel computing technique splits the computational domain into multiple compartments and assigns compute nodes to each of them. Depending on the available computational processing power (e.g., 10 logical processors computer) and the user allocated number of parallel computing processors (e.g., 8 processors), the 8 compartments will be solving simultaneously meanwhile the results are assembled and communicated to the host node which outputs the results. This presents a massive cost reduction compared to solving with serial mode whereby the entire domain is solved as just one compartment.

$$\frac{dX}{dt} = \mu_m \cdot \frac{1}{z} \cdot \left(\int_0^L \frac{I}{k_s + \frac{I}{1} + \frac{I^2}{k_i}} dz \right) \cdot X - u_d \cdot X^2 \qquad (2.46)$$

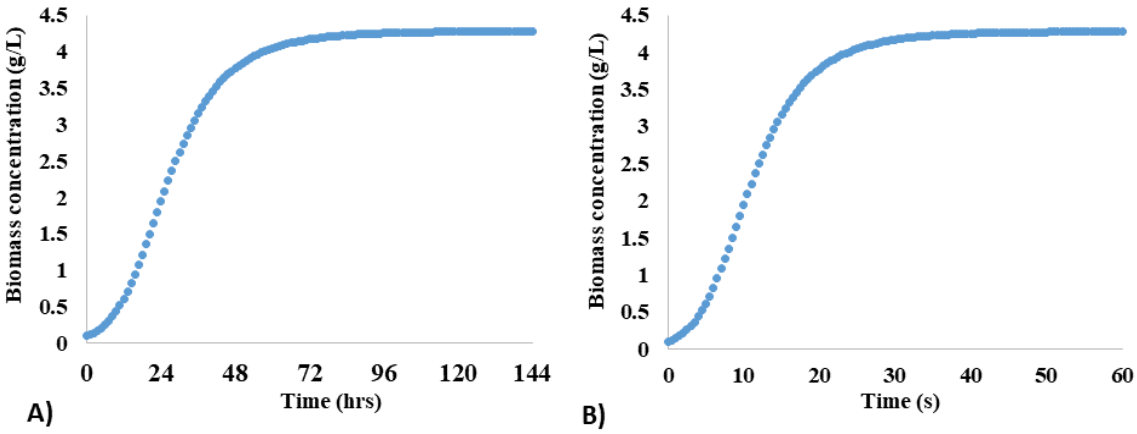

Figure 2.10: Accelerated growth kinetic strategy: A) 6 days (144 hrs) simulation turned into a B) 60 s simulations without compromising the sigmoid shape growth profile.

Therefore, the combination of accelerated growth kinetic and parallel computing techniques would provide simulation cost savings surpassing the current literature attainable standards as thoroughly discussed in Chapters 3 and 4.

2.7 Summary of literature review and PhD objectives

The literature review chapter firstly begins in Section 2.1 with the fundamentals of microbial photosynthesis and biohydrogen production by reviewing the involved multi-steps reactions, enzymes, and time scales. With references to microalgae (including cyanobacteria) and photosynthetic bacteria as exemplary photosynthetic microorganisms, the order of time scales were shown to range from milliseconds to days. In addition, the differing growth modes and hydrogen production metabolisms were also covered. In Section 2.2, the specialised piece of cultivating bioreactor equipment, which requires light supply and therefore termed photo-bioreactors, was reviewed. At this point, a case for choosing closed photobioreactors over open ones for this PhD research was elucidated as well as the upscaling bottlenecks. Thereafter, the literature mathematical models incorporating the influences of intensity, light attenuation, light/dark cycles, and temperature on biomass growth and secondary metabolite production were thoroughly reviewed in Section 2.3. These literature models were reported to (i) overestimate the impacts of light-inhibition on the local photosynthetic rate with Type II models, and (ii) exhibit multi-scale coupling challenges with Type III models, to hydrodynamic solvers. These were the identified gabs to be firstly addressed in addition to combining the complicated influences of light intensity, light

attenuation, light/dark cycles, and temperature effects to both the growth and non-growth associated bioproduct formations (e.g., biohydrogen) kinetics presented.

For this, the various thesis Chapters addressing the literature limitations with new constructed mathematical models were indicated. However, these constructed models have several model parameters to be identified and Section 2.4 was therefore focused on the dynamic parameter estimation methodologies. Both derivative-based and derivative-free methods were briefly reviewed for handling stiff and highly nonlinear problems. Once the model parameters are identified, the proposed models can now perform accurate bioprocess simulations without a hydrodynamic solver. As mixing conditions can minimise temperature and nutrient gradients, prevent cell sedimentation, and enhance gas-liquid mass transfer, just to highlight a few benefits, Section 2.5 therefore reviewed the literature hydrodynamic and turbulence models, as well as their implementation methodologies in CFD solvers. To couple the hydrodynamic and turbulence simulations to bioreaction kinetics, Section 2.6 reviewed the literature multiscale coupling approaches: (i) Circulation time simulation, (i) Lagrangian simulation, and (iii) Eulerian simulation. Among them, the latter two-steps Eulerian simulation approach with reduced computational resource requirements was adopted. Also, Section 2.6 pointed out the theoretical inconsistencies and computational costly coupling of Type III models to photobioreactor hydrodynamics thereby signalling the advent of new robust coupling approaches. This led to the brief review of accelerated growth kinetic and parallel computing techniques implemented within this PhD research for the reduction of simulation cost.

The presented summary pointed out some pertinent challenges to be addressed which aligns with the objectives of this PhD research. Therefore, the formulated objectives in Section 1.3 are restated below in context of the above-mentioned summary.

1. To incorporate the influence of macro-scale hydrodynamics into the original micro-scale three-state photosynthetic factory unit proposed by Eilers and Peeters [29] in 1988. By theoretical derivations, the resulting Type III model will be structurally reduced to Type II model without compromising its multi-scale simulation accuracy. This should address the (i) literature reported overestimation of light-inhibition impact on the local photosynthetic rate with previous Type II models, and (ii) multi-scale coupling challenges of Type III models to hydrodynamic solvers. Also, the model's flexibility will enable the coupling of temperature effects to the complicated influences of intensity, light attenuation, light/dark cycles on biomass growth and secondary metabolite (e.g., biohydrogen) production as flagged above in Section 2.3.

2. To exploit Computational Fluid Dynamic (CFD) in building a PDE solver that simulates the bioreactor fluid dynamics, light transmission, photosynthetic cell growth and secondary metabolite production (e.g., biohydrogen) at different photobioreactor scales and configurations. Firstly, both derivative-based algorithms and stochastic swarm intelligence-based algorithms shall be investigated for the model's dynamic parameter estimation. This is to handle the stiffness, and nonlinearities of the constructed photo-bioreactive models from objective 1, thus enabling the accurate bioprocess simulations outside of the CFD solver. Secondly, the Eulerian- Eulerian cost-efficient simulation approach together with RANS and $k-\varepsilon$ turbulence models will be employed. This will robustly couple the simulations of bioreactor fluid dynamics, light transport and photo-bioreactive models within the CFD solver. At this point, the CFD simulation cost of this PhD research levels with literature attained standards, and now paves the way forward for further cost improvements.

3. To investigate the computational efficiency of the multi-scale Eulerian CFD solver and propose efficient simulation strategies for enabling the realisation of large-scale bioprocess optimisation. Despite the reported simulation cost reduction from months to a few days with the two steps Eulerian-Eulerian approach, biomass growth is mostly the only literature simulated state variable. In the simulation of additional state variables like substrate consumption and biohydrogen production herein, the cost is expected to scale up to a few weeks or months, thus hindering large-scale bioprocess simulation and optimisation. Therefore, advanced modelling techniques (e.g., (i) acceleration of growth kinetic, (ii) parallel computing, or a combination thereof) will be investigated to accelerate the simulation time without compromising the solution quality to attain superior cost savings compared to the current literature CFD models.

4. To identify the primary limiting factors affecting the design, control and scale-up of different bioreactor configurations and then optimise the operating conditions subject to profitability and environment concerns. For this, several *in-silico* experiments will be designed to test formulated hypotheses quickly, such as the influences of photo-bioreaction model parameter uncertainties under hydrodynamic coupling via Monte Carlo simulations, which is previously unanswered in literature. This will bridge the literature gab of unavailable superior cost-efficient CFD integrated biokinetic solvers.

5. To establish external collaboration with other international groups and leverage the collaborative network to generate experimental data. Although CFD solvers returns qualitative and quantitative predictions of velocity, biomass, substrate (e.g., glycerol) and biohydrogen concentration contours, the results cannot be trusted without validation data collected using accurate experimental methods like Laser Doppler Anemometry (LDA), High-Performance Liquid Chromatography (HPC), and Gas Chromatography (GC).

Chapter 3

Synergising Biomass Growth Kinetics and Transport Mechanisms to Simulate Light/Dark Cycle Effects on Photo-production Systems

3.1 Preface

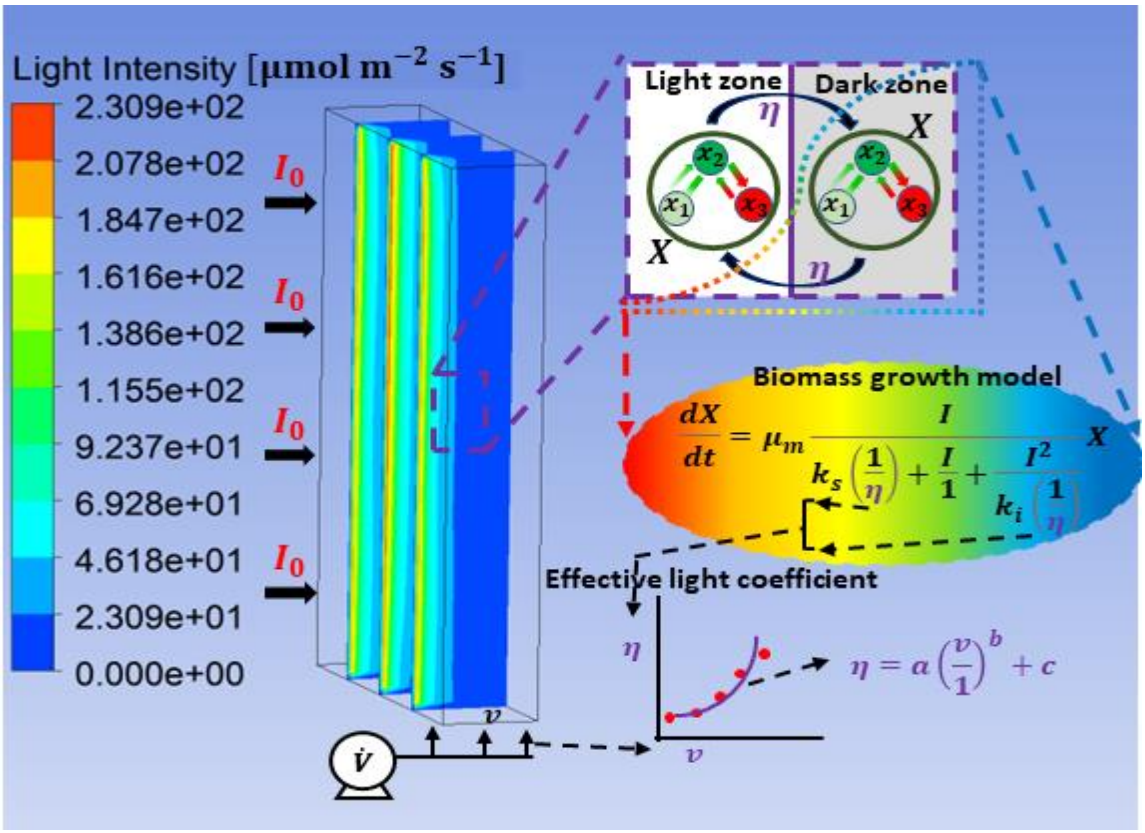

Figure 3.1: Graphical abstract illustrating the integration of light/dark cycles into biomass growth kinetics via new parameter, the *effective light coefficient, η* without the expensive external computation of cell light exposure history.

Light attenuation, a phenomenon responsible for the decreasing light transmission within photobioreactors due to cellular absorption and scattering, is a key challenge limiting the upscaling of photobioreactors for sustainable bio-productions. Under severe light attenuation, microbial cells in the photobioreactor's front-facing and interior sections are exposed to higher (photic zones) and lower (dark zones) light intensities respectively. If too long, the microbial cells are prone to photoinhibition and photolimitation consequentially affecting the overall biomass growth. However, intense culture mixing can reduce the microbial cells' residence time in the photic and dark zones, thus preventing the

photosynthetic proteins from over-reduction and over-oxidation thereby enhancing biomass growth.

Therefore, Chapter 3 focuses on the development of the first mechanistic model which directly integrates the consequential effects of light/dark cycles into biomass growth kinetics without the expensive external computation of cell light exposure history. Through theoretical derivation based on the intracellular reaction kinetics from the original three-state PSU model by Eilers and Peeters [29], modifications were made by embedding a new parameter, the *effective light coefficient* to account for the effects of culture mixing on the macro-scale biomass growth kinetics. To estimate the value of the proposed *effective light coefficient*, a new cost-efficient multiscale photobioreactive transport modelling strategy was developed to couple fluid dynamics with biomass growth kinetics and light transmission. From the simulation results, an original nonlinear correlation was proposed to link the *effective light coefficient* with photobioreactor gas inflow rate, enabling its control and optimisation to alleviate light attenuation and maintain a high biomass growth rate, this has not been done before.

The published paper presented herein as Chapter 3 is structured as follows: Section 3.1 introduces the study; Section 3.2 presents the methodologies for mechanistic model development, *in-silico* design of experiments, and parameter estimation; Section 3.3 then presents the *in-silico* validations results, discussions for correlating the *effective light coefficient* with photobioreactor gas inflow rate, and strategy the photobioreactor's optimal control; finally, Section 3.4 concludes the current study.

3.2 Publication 1

Bovinille Anye Cho[1], Miguel Ángel de Carvalho Servia[1], Ehecatl Antonio del Río Chanona[2], Robin Smith[1], Dongda Zhang[1]. Synergising biomass growth kinetics and transport mechanisms to simulate light/dark cycle effects on photo-production systems. Biotechnol Bioeng 2021;118:1932–42. https://doi.org/10.1002/bit.27707.

1. Department of Chemical Engineering and Analytical Science, University of Manchester, the Mill, Sackville Street, Manchester, M1 3AL, UK.
2. Department of Chemical Engineering, Imperial College London, South Kensington Campus, London SW7 2AZ, UK.

Bovinille Anye Cho's contributions included construction of the multiscale model, modelling methodology development and implementation, drafting of the manuscript and manuscript revision for important intellectual content. Miguel Ángel de Carvalho Servia's contributions include dynamic model parameter estimation and drafting of the manuscript. Ehecatl Antonio del Río Chanona and Robin Smith involved critical revision of the manuscript for important intellectual content as well as the final approval of the article. Dongda Zhang involved in the critical revision of the manuscript as well as the final approval of the article. He also had critical overview of the direction of the project and the development strategy of this paper.

Abstract

Light attenuation is a primary challenge limiting the upscaling of photobioreactors for sustainable bio-production. One key to this challenge, is to model and optimise the light/dark cycles so that cells within the dark region can be efficiently transferred to the light region for photosynthesis. Therefore, this study proposes the first mechanistic model to integrate the light/dark cycle effects into biomass growth kinetics. This model was initially constructed through theoretical derivation based on the intracellular reaction kinetics, and was subsequently modified by embedding a new parameter, effective light coefficient, to account for the effects of culture mixing. To generate *in silico* process data, a new multiscale reactive transport modelling strategy was developed to couple fluid dynamics with biomass growth kinetics and light transmission. By comparing against previous experimental and computational studies, the multiscale model shows to be of high accuracy. Based on its simulation result, an original correlation was proposed to link effective light coefficient with photobioreactor gas inflow rate; this has not been done before. The impact of this study is that by using the proposed mechanistic model and correlation, we can easily control and optimise photobioreactor gas inflow rates to alleviate light attenuation and maintain a high biomass growth rate.

Keywords: light/dark cycle; multiscale modelling; photobioreactor design; kinetic modelling; biomass cultivation.

3.1 Introduction

Bio-renewable products ranging from biofuels to more valuable components such as pigments and antioxidants have placed the cultivation of photosynthetic microorganisms, for example, microalgae and cyanobacteria in photobioreactors (PBRs) at the spotlight of biotechnological research. However, the economic viability of this biotechnology is hurdled by its high capital, operational and maintenance cost due to difficulties in designing and upscaling of PBRs [44,64,144,149]. In an attempt to bridge this gap, constructing advanced mathematical models to analyse the underlying process plays a vital role. At present, different types of models integrating microscopic and/or macroscopic biokinetics with light transmission and/or fluid dynamics have been proposed to assess the performance of PBRs. On the one hand, macroscopic models that combine the Monod-type empirical biokinetic equations with light transmission functions as viewed in Socher et al., [78] have been previously used to optimise the geometry of pilot-scale PBRs by Ali et al., [20] and analyse biomass productivity in different sizes of open raceway ponds as seen in Amini et al., and Park-Li [142,150]. However, effects of light/dark cycles on biomass growth and reactor design have been barely included. Light/dark cycles are induced by fluid dynamics and light attenuation. A short light/dark cycle caused by an intense culture mixing can reduce cells' residence time in the photic zone near the irradiated PBR surface and the dark zone in the PBR interior, thus preventing photosynthetic proteins from over-reduction and over-oxidation for algae and cyanobacteria species as reported by Janssen et al., and Luo-Al Dahhan [111,151]. This improves the light utilisation efficiency and microbial photosynthetic activity [97,152]. Although there have been a few studies trying to simulate this phenomenon like Li et al., and Pruvost et al., [14,15], they did not integrate light/dark cycles into the biokinetic models. Instead, external computation of cell light exposure history was performed separately and then averaged to solve the cell growth kinetic model. This simplification may introduce large errors especially when being applied to large scale PBRs. On the other hand, microscopic kinetic models derived based on photosynthetic units (PSUs) have also been embedded into computational fluid dynamics (CFD) along with light transport models to simulate spatio-temporal changes of intracellular PSU states and culture biomass growth [27,56,153]. Although these models have achieved satisfactory results when compared with experimental data, their underlying coupling strategy was computationally expensive and lacks theoretical support. This is because the PSU models are primarily developed to simulate intracellular photosynthetic reactions without the inclusion of macroscale biomass concentration changes as interpreted from the works of Gao et al., and Papacek et al., [101,154]. Thus, when embedded into the CFD model, this multiscale reactive

transport model is only valid over a small time period when biomass concentration changes are negligible. As a result, the model can only be run within a small time step to estimate the spatial ratio between different PSU states under the current light intensity distribution. This ratio is then used to estimate a volume averaged growth rate to calculate biomass concentration. The updated concentration is finally used to calculate local intensity distribution at the next time step. Hence, the lack of direct coupling between intracellular kinetics and fluid dynamics causes a high computational cost which severely limits the application of this approach for PBR design.

Overall, at the meso/macroscale, most biokinetic models assume that fluid dynamics and light transmission are not correlated. Despite the fact that fluid dynamics directly affect the frequency of light/dark cycles, there is lack of accurate models integrating fluid dynamics into cell growth kinetics. Furthermore, theoretical connections between macroscale empirical biomass growth kinetics (e.g., Monod-type models) and intracellular photosynthetic reaction kinetics (e.g., PSU models) are still missing. It is unclear how the parameters in an empirical model are linked to the metabolic reactions. Thus, it is challenging to modify the model structure when trying to incorporate more physical/biological information.

Therefore, to address these challenges, the present study proposes a new physical model linking the synergistic effects of light/dark cycles and fluid dynamics into biomass growth kinetics. This model is proposed based on a theoretical derivation using intracellular PSU reaction mechanisms. The remainder of this paper is structured as follows: the biokinetic model derivation and CFD coupling strategy for PBR simulation are presented in Section 3.2. New correlations between gas inflow rate (indicative of fluid dynamics) and light related kinetic parameters along with their practical application are discussed in Section 3.3, followed by the final conclusion and suggestions for future work.

3.2 Methodology

3.2.1 Derivation of a kinetic model for biomass growth

The intracellular kinetics occurring at the simplest functional unit of the photosynthetic apparatus (PSU) are used here. These PSUs are assume to occur within three hypothetical states as visualised in Figure 3.2a: (i) an open state x_1, where the PSUs are inactive but move upon activation via the absorption of photons; (ii) a closed state x_2, where PSUs are light saturated thereby using the absorbed energy to begin photo-production (photochemical quenching), and (iii) an inhibited state x_3, where the PSUs are temporarily damaged under

high light intensities but can be recovered to the closed state after cellular self-reparation. This state transitioning kinetics is described by Eqs. (3.1) to (3.4).

$$\frac{dx_1}{dt} = -r_1 + r_2 = -\alpha I x_1 + \gamma x_2 \tag{3.1}$$

$$\frac{dx_2}{dt} = r_1 - r_2 - r_3 + r_4 = \alpha I x_1 - \gamma x_2 - \beta I x_2 + \sigma x_3 \tag{3.2}$$

$$\frac{dx_3}{dt} = r_4 - r_3 = \beta I x_2 - \sigma x_3 \tag{3.3}$$

$$x_1 + x_2 + x_3 = 1 \tag{3.4}$$

where α and β are reaction rate constants for light dependent reactions from x_1 to x_2 and from x_2 to x_3, respectively, and γ and σ are reaction rate constants for light independent reactions from x_2 to x_1 and from x_3 to x_2, respectively.

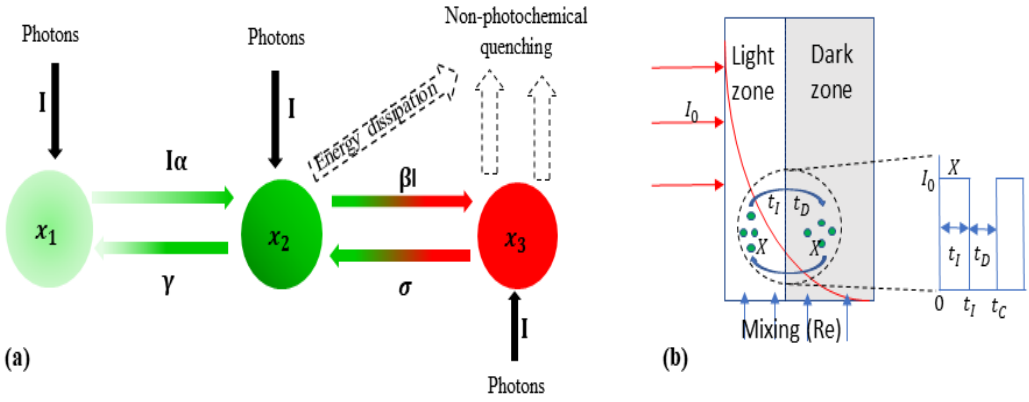

Figure 3.2: Schematic illustrations of (a) three state intracellular kinetic model (with light inhibition) inspired from Han and Nikolaou scheme [95,98] and (b) Mixing induced alternation of L/D cycles. (α, β) and (γ, σ) corresponds to the light and dark reaction coefficients respectively, I is photon, t_I and t_D are the duration of light and dark exposures in each light/dark cycle, Re is Reynolds number induced mixing.

From the literature by Wu-Merchuk [101], the rates of these reactions are in the order of seconds to minutes. For example, for red marine alga *Porphyridium* sp., the doubling time of r_1 to r_4 is 1.79 s, 4.75 s, 99 min and 24 min, respectively. Compared to the growth rate of microalgae and cyanobacteria of which the average doubling time is 26 hours as reported by Liu et al., [155] and 7-12 hours as reported by Bernstein [156], respectively, it can be assumed that these intracellular reactions are at a pseudo-equilibrium condition (i.e. $\frac{dx_1}{dt} = \frac{dx_2}{dt} = \frac{dx_3}{dt} = 0$) when estimating biomass growth. Biomass growth is exclusively dependent on the closed state, x_2, given that only cells at this state have received enough solar energy for their growth as adopted by Solimeno et al., [157]. Therefore, based on Eqs. (3.1) to (3.4) a macroscopic biomass growth kinetic model can be written as Eq. (3.5):

$$\frac{dX}{dt} = \mu_m(x_2 X) = \mu_m \frac{I}{\frac{\gamma}{\alpha} + \frac{I}{1} + \frac{I^2}{\frac{\sigma}{\beta}}} X = \mu_m \frac{I}{k_s + I + \frac{I^2}{k_i}} X \quad (3.5)$$

where μ is the maximum specific growth rate (h^{-1}), X is biomass concentration (g L^{-1}), k_s is light saturation term (μmol m^{-2} s^{-1}), and k_i is light inhibition term (μmol m^{-2} s^{-1}).

Eq. (3.5) can be exactly presented as the commonly used Aiba model which accounts for photo-limitation, photo-saturation, and photo-inhibition as formulated by Aiba in 1982 [158]. In spite of the wide application of this model, k_s and k_i are often considered as empirical terms, and their respective biological meaning has never been clarified. This derivation, therefore, filled this gap. It is seen that these terms represent the ratios of different intracellular reaction rate constants. To validate this, $k_s = \frac{0.1460}{0.001935} = 75.5$ μmol m^{-2} s^{-1}, and $k_i = \frac{0.0004796}{5.7848\times10^{-7}} = 829.1$ μmol m^{-2} s^{-1} according to the intracellular reaction rate constants for red marine alga *Porphyridium* sp., as determined by Wu-Merchuk [101]. These values of k_s and k_i falls within the respective literature ranges of 70 μmol m^{-2} s^{-1} to 250 μmol m^{-2} s^{-1} and 457 μmol m^{-2} s^{-1} to 2760 μmol m^{-2} s^{-1} for algae and cyanobacteria as reported by Zhang et al., [105] using the empirical Aiba model.

Noticeably, Eq. (3.5) does not include light attenuation, a phenomenon responsible for the decrease in light transmission within PBRs due to cellular absorption and scattering. This impacts the PBR's local light availability as more is absorbed by cells in the front (light zone) while cells in the rear (dark zone) are light deprived. Under such conditions, cells are exposed to light/dark cycles which limits biomass growth. The frequency of these light/dark cycles are largely influenced by culture mixing which is dictated by fluid dynamics. As illustrated in Figure 3.2b, at each position in a PBR with a specific local light intensity I_l, cells can move back and forth due to culture mixing, thus being exposed to either a 'lighter' region where they can absorb more light or a 'darker' region where less solar energy resource is available. Thus, the actual light intensity that cells experienced during their growth could be significantly different from the local light intensity I_l. To account for this effect, in this work, we defined a new coefficient, *effective light coefficient* η, to estimate the 'effective' local light intensity ($\eta \cdot I_l$) based on engineering principles. Therefore, Eqs. (3.1) to (3.3) are modified to Eqs. (3.6) to (3.8):

$$\frac{dx_1}{dt} = -r_1 + r_2 = -\alpha(I\eta)x_1 + \gamma x_2 \quad (3.6)$$

$$\frac{dx_2}{dt} = r_1 - r_2 - r_3 + r_4 = \alpha(I\eta)x_1 - \gamma x_2 - \beta(I\eta)x_2 + \sigma x_3 \quad (3.7)$$

$$\frac{dx_3}{dt} = r_4 - r_3 = \beta(I\eta)x_2 - \sigma x_3 \tag{3.8}$$

Solving Eqs. (3.6) to (3.8) in the same manner results in a new biokinetic model taking into account light/dark cycle as Eqs. (3.9). The effective light coefficient depends on the culture mixing which is utterly determined by the mixing energy if the PBR configuration is fixed. In practice, as mixing energy is difficult to be measure directly but is closely linked to the gas inflow rate for many PBRs (if gas inflow rate is used for culture mixing), it is more convenient to link gas inflow rate with the effective light coefficient. Hence, by changing the gas inflow rate, we can control biomass growth rate during biomass cultivation. The correlation between η and gas inflow rate will be determined in Section 3.3.4. In principle, if culture mixing in a PBR is carried out using other approaches, then gas inflow rate can be replaced by other parameters such as impeller rotation rate.

$$\frac{dX}{dt} = \mu_m \frac{I}{k_s\left(\frac{1}{\eta}\right) + \frac{I}{1} + \frac{I^2}{k_i\left(\frac{1}{\eta}\right)}} X \tag{3.9}$$

In order to estimate η and investigate how it is correlated with the PBR fluid dynamics, two *in-silico* case studies are presented in the following sections.

3.2.2 Introduction to the *in-silico* PBRs

The Flat-Plate PBRs (FP-PBRs) simulated in this study have dimensions of 100 mm × 150 mm × 25 mm (length, height and thickness). Two scenarios, scenarios 1 (see Figure. 3.3a): one centrally positioned sparger, and scenarios 2 (see Figure 3.3b): two equidistantly positioned spargers, were investigated since the geometric positioning of aeration (sparger) inlets in FP-PBR significantly contributes to the culture flow pattern and modulating the light/dark cycles as visualised in the paper of Yang et al., [159]. The air flowing through the square shape sparger of size 2 mm × 2 mm has an average bubble diameter, d_b of 3 mm as utilised by Huang et al., [55] operating under five different gas inflow rates for each scenario: scenario 1 (0.1 m s^{-1}, 0.5 m s^{-1}, 1.0 m s^{-1}, 1.5 m s^{-1} and 2.0 m s^{-1}) and Scenario 2 (0.25 m s^{-1}, 0.5 m s^{-1}, 0.52 m s^{-1}, 0.75 m s^{-1}, and 1.0 m s^{-1}) respectively, so that total volumetric gas flowrate is same in the two scenarios. The gas inflow rates selected here correspond to a typical range of superficial gas velocities used in PBR studies [55,159,160]. The PBRs were unidirectionally illuminated with fluorescent lamp source same as Wu-Merchuk [101] at an incident light intensity of 300 μmol m^{-2} s^{-1}. This intensity is often used for microalgae experimental cultivations, for example: Li et al., and Rio-chonana et al., [14,121]. Nutrient

concentration (i.e., CO_2) was assumed to be sufficient and therefore their effects are not included in the model.

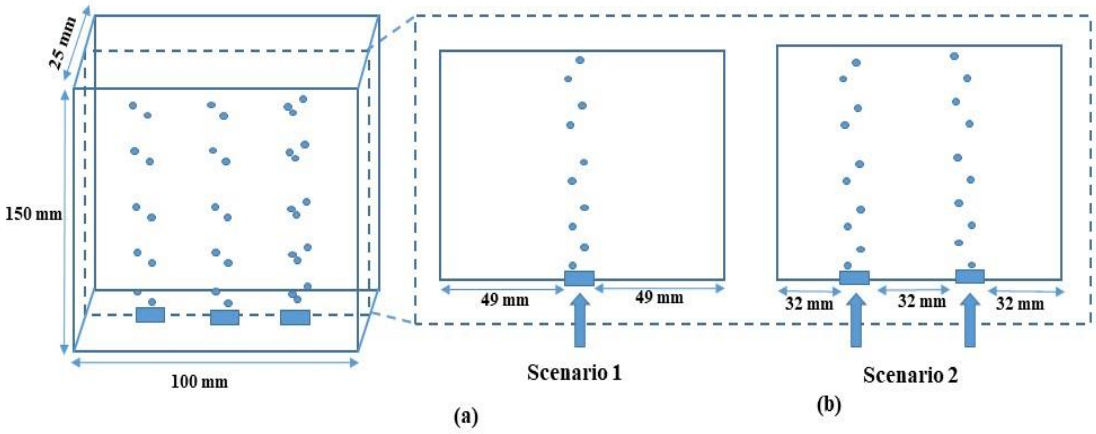

Figure 3.3: Schematic illustration of flat-plate PBR (FP-PBR) under investigation with (a) Scenario 1, and (b) Scenario 2.

3.2.3. Computational fluid dynamics simulation

Coupling CFD with biokinetic model for process data generation remains a challenge as discussed in the introduction. To solve this issue, a new approach was proposed here to save computational cost while guaranteeing a high simulation accuracy.

3.2.3.1 Selection of the gas-liquid multiphase model

A two-phase fluid (water and air) model assuming that the microbial cells follow the water phase without interference is applied for the multiphase PBR system using the classical Eulerian-Eulerian approach as indicated by Papacek et al., [62]. This results to the continuity and momentum Eqs. (3.10) and (3.11), respectively.

$$\frac{\partial}{\partial t}(\alpha_k \rho_k) + \nabla(\alpha_k \rho_k \boldsymbol{u}_k) = 0\,, (k = L, G) \tag{3.10}$$

$$\begin{aligned} &\frac{\partial}{\partial t}(\alpha_k \rho_k \boldsymbol{u}_k) + \nabla(\alpha_k \rho_k \boldsymbol{u}_k \boldsymbol{u}_k) = -\alpha_k \nabla p + \alpha_k \rho_k \boldsymbol{g} \\ &+\nabla\left(\alpha_k \mu_{k,e}\left[\nabla \boldsymbol{u}_k + (\nabla \boldsymbol{u}_k)^T - \frac{2}{3}\mathrm{I}(\nabla \boldsymbol{u}_k)\right]\right) + \boldsymbol{F}_{l,k}\,, (k = L, G) \end{aligned} \tag{3.11}$$

where subscript $k = L, G$ stands for liquid or gas phase, $\alpha_k, \rho_k, \boldsymbol{u}_k$ corresponds to the phase volume fraction, density, and velocity vector, respectively. The pressure and gravitational vector are denoted as $p, \boldsymbol{g}$ respectively. $\mu_{k,e}$ is effective viscosity which includes both molecular viscosity, $\mu_{k,m}$ and turbulent viscosity $\mu_{k,T}$. $\mu_{k,T}$ is modelled using the standard $k-\varepsilon$ turbulence model [161]. I is the unit tensor. Drag effect being more dominant is the

only interphase momentum force $\boldsymbol{F}_{l,k}$ which is considered herein. It was modelled with the Schiller-Naumann drag model as it is widely used in bubble column PBRs, for example: Nauha-Alopaeus [57]. Detailed formulations of the standard $k-\varepsilon$ turbulent model and the Schiller-Naumann drag model can be found in Rampure et al., [162] and Luo-Al Dahhan [111].

3.2.3.2 Rigorous biomass transfer model

To account for both light limitation and inhibition, the three-PSU-state kinetic model is used in this case. The mass transport model for biomass concentration accounting for both time and spatial dimensions is therefore expressed as Eq. (3.12). The first term on the left stands for biomass accumulation, the second term on the left denotes biomass convection, the first term on the right denotes biomass diffusion, and the second term on the right represents biomass growth. Attention must be paid to the fact that Eq. (3.12) does not need to include the effective light coefficient η, as this equation captures the instantaneous biomass growth at each time and each location inside a PBR. In addition, a decay term is also added in Eq. (3.12) in same fashion as Rio-chanona et al., [121]. Practically, the decay rate constant μ_d is a function of culture shear stress which is also dependent on fluid dynamics. As the current study only investigates biomass growth, the decay rate constant is set fixed. This assumption is found to be true as long as the shear stress does not exceed a threshold, beneath which shear stress has negligible effect on cell decay [163].

$$\frac{\partial X}{\partial t}+\nabla(\boldsymbol{u}_L X)=\nabla\left(\left(D_L+\frac{\mu_{k,T}}{\rho_L Sc_t}\right)\nabla X\right)+\left(\mu_m\frac{I_l}{k_s+I_l+\frac{I_l}{k_i}}X-\mu_d X^2\right) \tag{3.12}$$

where $\boldsymbol{u}_L$ and ρ_L are the culture velocity and density (using water density), respectively, D_L = 5.5×10^{-10} m^2 s^{-1} is biomass viscosity, $Sc_t=0.7$ is turbulent Schmidt number taken from Gao et al., [27], $\mu_{k,T}$ is turbulent viscosity. Values of biological kinetic parameters are modified from literature for demonstration purpose: $\mu_m=0.225$ h^{-1} is maximum specific growth rate, $\mu_d=6.87\times10^{-3}$ L g^{-1} h^{-1} is the death rate constant taken from Rio-chanona et al., and Zhang et al., [105,121], $k_s=\frac{\gamma}{\alpha}=82.84$ µmol m^{-2} s^{-1}, and $k_i=\frac{\sigma}{\beta}=$ 910.21 µmol m^{-2} s^{-1} [101], I_l is the local light intensity calculated by Eq. (3.13).

$$I_l=I_0\cdot\exp\left[-\left(\frac{3\cdot\varepsilon_G}{d_b}+\tau\cdot X\right)z\right] \tag{3.13}$$

Eq. (3.13) is a variant Beer-Lambert's law accounting for both light absorption and gas bubble light scattering formulated by Zhang et al., [105]. In this work, $I_0=300$ µmol m^{-2} s^{-}

[1] is the incident light intensity, ε_G is the gas volume fraction, $d_b = 0.003$ m is gas bubble diameter, $\tau = 126$ m^2 g^{-1} is the light absorption coefficient, and z is the light penetration length.

3.2.3.3 Multiscale model coupling strategy

In this work, CFD simulations were executed using ANSYS FLUENT 19.2. The 3D PBR geometries were meshed with structured grid amounting to 62,500 volumes after grid test with time step sizes. Higher resolution areas were identified to be the PBR bottom section with bubble inlets and the PBR top sections with reverse flow of the liquid phase due to the presence of a free surface (pressure outlet/degassing zone). Therefore, additional grid refinement was conducted in these areas in comparison to the PBR centre section.

To couple the biomass transport model (Eq. (3.12)) with the hydrodynamics model (Eqs. (3.10) to (3.11)), a two-step approach is proposed. Initially, a time step size of 0.005 s and a simulation time of 60 s were used to solve Eqs. (3.10) to (3.11). Upon convergence, Eq. (3.12) was solved with a time step size of 0.005 s for 100 s, with biomass growth and death rates being accelerated by 8640 times such that the 100-second simulation result is representative of the process behaviour for 10 days of biomass cultivation. This approximation is attributed to the fact that fluid dynamics converges more rapidly (order of seconds as reported Papacek et al., [62]) than cell growth (e.g., doubling time at an order of days as reported by Benstein and Liu et al., [155,156]). Even by accelerating biomass growth kinetics up to an order of minutes or hours, cells would have still experienced the light/dark cycles hundreds of times. Hence, the effect of light/dark cycles on biomass growth will be similar to that estimated using the true biomass growth parameters (where cells experienced light/dark cycles over thousands of times). Through this approximation, the computational time cost can be greatly reduced.

To couple the biomass transport model with the light attenuation model (Eq. (3.13)), a User Defined Memory for recording the accumulation of biomass was inserted into the first term on the left of Eq. (3.12) and was then passed into Eq. (3.13) at every iteration during the simulation. All User Defined Functions were written in C programming language, compiled, and inserted into the CFD solver. In this way, biomass growth kinetics and transport, light transmission, and fluid dynamics can be fully coupled and solved simultaneously.

3.2.4 Parameter estimation of the dynamic model for the effective light coefficient

Once data is generated from the rigorous multiscale model, it is used to estimate η in Eq. (3.9). The effective light coefficient represents the effect of light/dark cycles on the biomass

growth kinetics, and this equation can be served as a mechanistic surrogate model to enable efficient process simulation and real-time control. To include light attenuation and cell decay, Eq. (3.9) is modified as Eq. (3.14), which can be further approximated as Eq. (3.15) to eliminate the spatial dimension effect (light transmission) just like Zhang et al., [105]. In this way, overall biomass concentration inside a PBR as well as its correlation with light/dark cycles can be calculated.

$$\frac{dX}{dt} = \mu_m \cdot \frac{1}{z} \cdot \left(\int_0^L \frac{I}{k_s\left(\frac{1}{\eta}\right) + \frac{I}{1} + \frac{I^2}{k_i\left(\frac{1}{\eta}\right)}} dz \right) \cdot X - u_d \cdot X^2 \tag{3.14}$$

$$\frac{dX}{dt} = \frac{u_m}{20} \cdot \sum_{n=1}^{9} \left(\frac{I_0}{I_0 + \frac{k_s}{\eta} + \frac{I_0^2}{\frac{k_i}{\eta}}} + \frac{2 \cdot I_{\frac{n \cdot L}{10}}}{I_{\frac{n \cdot L}{10}} + \frac{k_s}{\eta} + \frac{I_{\frac{n \cdot L}{10}}^2}{\frac{k_i}{\eta}}} + \frac{I_L}{I_L + \frac{k_s}{\eta} + \frac{I_L^2}{\frac{k_i}{\eta}}} \right) \cdot X - u_d \tag{3.15}$$

$$\cdot X^2$$

where L is the PBR width (total light transmission length).

However, Eq. (3.15) is a highly nonlinear ordinary differential equation, imposing great obstacles when performing parameter estimation to calculate the value of η under different gas inflow rate using gradient based optimisation algorithms. Therefore, a stochastic hybrid optimisation algorithm was used to estimate the value of η. This hybrid algorithm utilises the particle swarm optimisation (PSO) and the artificial bee colony (ABC) algorithms in parallel. The hybrid algorithm is initialised with a discrete number of inputs, which are evaluated with the objective function (negative log-likelihood) and sorted into different groups. A specified percentage (50% in this study) of the best inputs are used by the PSO, with the rest used by the ABC as per Karaboga-Akay [137]. This process is repeated over a specified number of iterations (10 iterations in this study), and the best input found is returned. The advantage of this hybrid algorithm is that it uses the explorative characteristics of ABC to explore the search space of the worse inputs (thus finding potentially good solutions) and uses the exploitative characteristics of PSO reported by Kennedy et al., [135] to exploit the search space of the better inputs. The computational time to attain the solution is 2.5 min in this study.

3.3 Results and discussion

3.3.1 Computational cost analysis

All the CFD simulations were executed on a workstation. The time cost for each test case was 12.3 hours and amounted to 111.4 hours for all the cases investigated in this study. This presented a significant reduction in computational cost given that the small time step size of 0.005 s was maintained in both stage one (converging the fluid dynamic equations) and stage two (solving the biomass transport model). Solving steps one and two under the same time step size ensures numerical stability and retains essential information of light/dark cycles for PBR simulation. Hence, it is advantageous in comparison to the previous studies whereby the time step size for stage two is increased dramatically such as from 0.01 s to 3,600 s over 3 weeks of cultivation by the authors Amini et al., [142] and from 0.0005 s to 10 s over 120 hours of cultivation by Gao et al., [27].

3.3.2 In silico experimental data validation

To examine the current multiscale modelling strategy, several properties were analysed to compare with the literature observations. Figure 3.4 a-c show typical instantaneous water displacement for Scenario 1 displayed on a cross sectional plane (x-y) at z = 0.0125 m, for better visualisation. It is seen that a dynamic vertical motion from the bottom (sparger) to the centre top PBR sections with randomly oscillating plume was observed similar to that of Huang et al., Yang et al., and Yu et al., [55,159,160]. This was intepreted to be generated by the raising plume of air-volume fractions which induces vortical structures in the liduid phase thereby displacing it chaotically. In addition, as seen in Figure 3.4 d-f, the Turbulence Kinetic Energy (TKE) distribution were found to be well correlated with the chaotic mixing patterns induced by the rising plume. Hence, regions with high TKE values within the flow filed correlated well with the appearance of bubbles in the FP-PBR which is in agreement with the results of other researchers, for example Yang et al., Yu et al., and Zhao etal., [159,160,164].

To check for the flow regime induced by the rising bubbles within the FP-PBR, a Reynolds number Re is defined using Eq. (3.16) which was reportedly used by Pfleger et al., [161] for 3D multiphase CFD simulation of FP-PBR:

$$Re = \frac{\rho_L \cdot \boldsymbol{u}_g \cdot Z}{\mu_L} \tag{3.16}$$

In this study, the value of Re is 10,366 for the lowest gas inflow rate and 15,192 for the highest gas inflow rate, thus indicating turbulent flow regimes and validating the selection of the multiphase turbulent flow model (Eq. (3.11)). This supports the chaotic velocity flow

pattern observed inside the FP-PBR as visualised in Figure 3.4 a-c. The same analysis was also carried out to evaluate the data accuracy in Scenario 2, thus not repeated here.

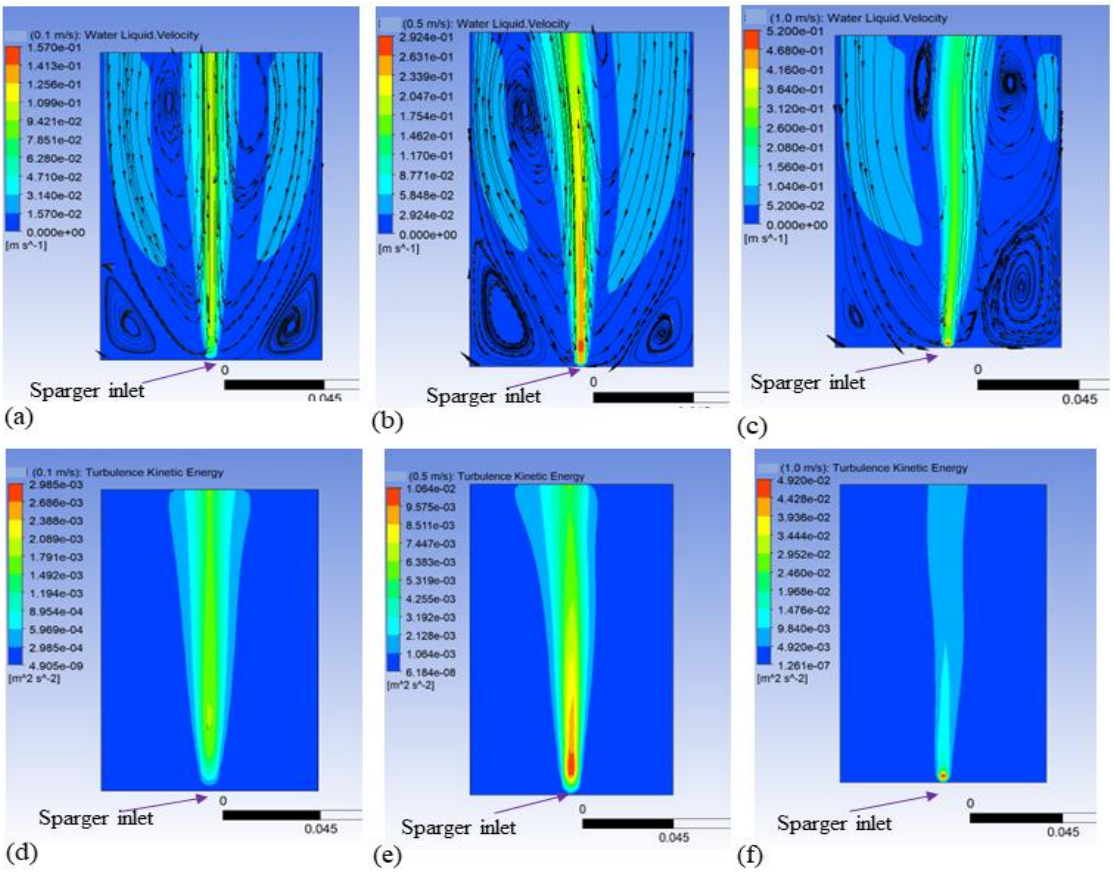

Figure 3.4: Scenario 1 contour plots of water flow patterns ((a), (b), (c)) and Turbulence Kinetic Energy (TKE) ((d), (e), (f)) distribution inside the FP-PBR for three test cases: (0.1 m s^{-1}), (0.5 m s^{-1}), and (1.0 m s^{-1}).

3.3.3 Effect of gas inflow rate on biomass growth

Only biomass growth for the first 144 hours of cultivation is presented since there was no observable change in biomass concentration after this time (stationary phase). Figure 3.5a shows the biomass evolution-time profiles of all test cases in Scenario 1. These profiles are observed to attain a saturation biomass concentration ranging from 4.2 g L^{-1} to 5.0 g L^{-1} which is realistic for a batch photo-production process operated under good aeration conditions [56,164,165]. The maximum biomass concentration increased by 16.7 % from a gas inflow rate of 0.1 m s^{-1} to 2.0 m s^{-1}. This was expected as increasing gas inflow rate leads to a better culture mixing and a more frequent light/dark cycle for cells to absorb solar energy, in alignment with previous experimental observations by Grobbelaar, Janssen et al., and Richmond [151,165,166]. This can be further proved given that the liquid phase velocity along the light transmission direction increases by 307.7% with the increasing gas inflow rate from 0.1 m s^{-1} to 2.0 m s^{-1} (see Figure 3.5b), shortening the light/dark cycles as reported

in Huang et al., [55]. The increase of biomass concentration under different cases also proves the accuracy of the multiscale model coupling strategy proposed in this study.

Most importantly, it is expected that maximum biomass concentration will only increase mildly when increasing the gas inflow rate as observed in Zhao et al., [164]. This is because biomass growth kinetics does not directly depend on fluid dynamics, but culture mixing can affect the light exposure history that cells experienced during their growth. As a result, an intensified culture mixing will not increase biomass concentration as dramatic as what observed when changing other key factors such as temperature, pH, or nutrient supply. Finally, Scenario 2 also yields a similar conclusion as Scenario 1, thus not presented here.

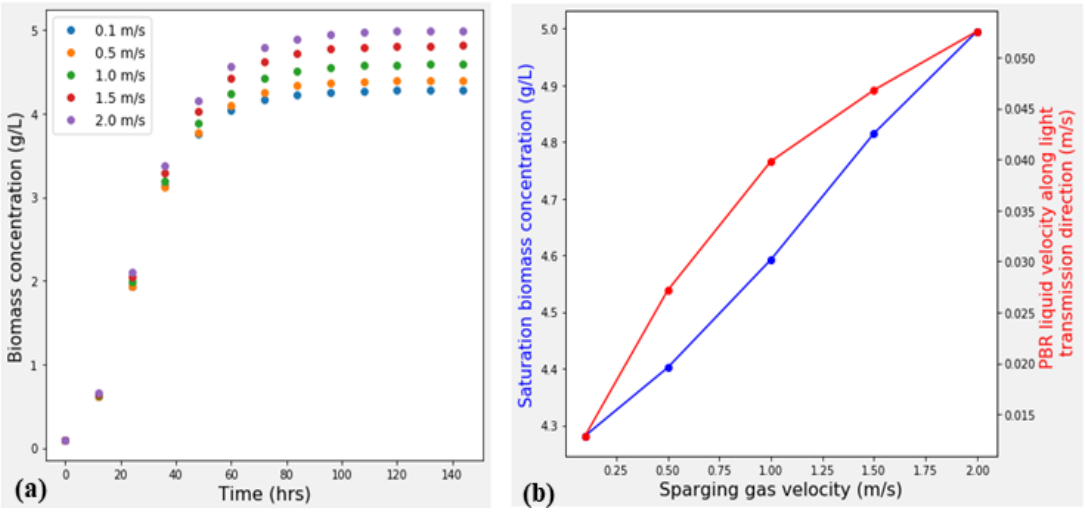

Figure 3.5: Scenario 1 CFD prediction for (a) biomass evolution with time, and (b) biomass growth dependence on liquid velocity along the light transmission direction

3.3.4 Correlating the effective light coefficient with gas inflow rate

The estimated values of effective light coefficient, η for all test cases in Scenario 1 and 2 are summarised in Table 3.1 while the fitting results are presented in Figure 3.6. It is observed that the model fits all the experimental data, indicating that the currently proposed biokinetic model (Eq. (3.15)) can well simulate the effect of light/dark cycles on biomass growth. Specifically, two main observations were drawn from Table 3.1. Firstly, the value of η is greater than 1 in both Scenario 1 and 2. This suggests a higher "effective" local light intensity as $(\eta \cdot I_l) > I_l$, implying that cells suspended in the dark region in fact have absorbed more light for their growth due to culture mixing, and that purely using a light attention equation to calculate a PBR's 'apparent' dark region may overestimate the effect of light attenuation on biomass growth kinetics and PBR upscaling. This greater effective local light intensity also suggests a better light utilisation efficiency since culture mixing also prevents cells exposed within the light zone from being over-oxidised due to the long-term absorption of excessive photons (e.g., photo-inhibition).

Table 3.1: Estimated values of the effective light coefficient, η

Scenario 1		Scenario 2	
Test case	effective light coefficient, η	Test case	effective light coefficient, η
0.1 m s^{-1}	1.395	0.25 m s^{-1}	1.315
0.5 m s^{-1}	1.560	0.5 m s^{-1}	1.338
1.0 m s^{-1}	1.969	0.52 m s^{-1}	1.412
1.5 m s^{-1}	2.711	0.75 m s^{-1}	1.580
2.0 m s^{-1}	3.625	1.0 m s^{-1}	2.457

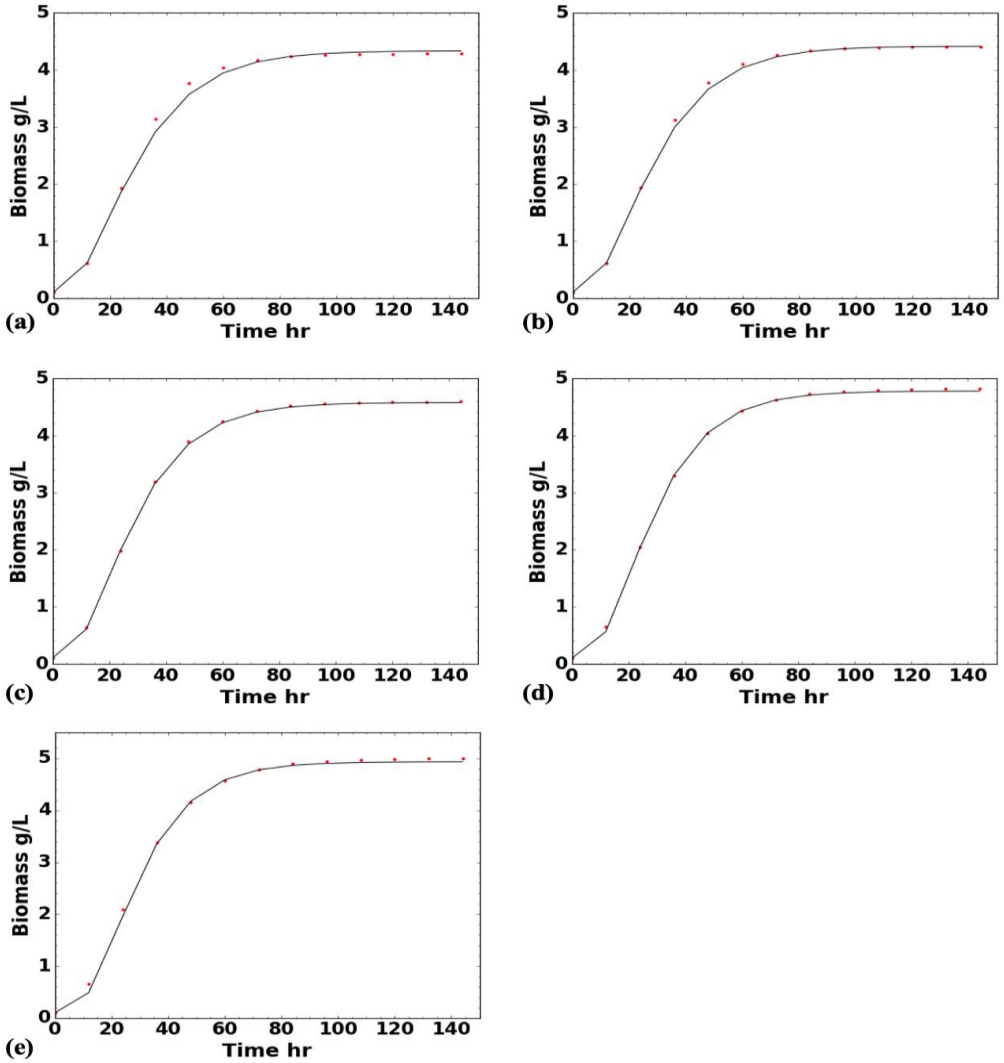

Figure 3.6: Effective light coefficient estimation results for all test cases in scenario 1. Line: model fitting results, points *in-silico* process data. Scenario 2 showed similar fitting, thus not repeated here.

Secondly, the effective light coefficient η increases with an increasing gas inflow rate in each scenarios: a 159.8% increase from 0.1 m s^{-1} to 2.0 m s^{-1} in Scenario 1 and an 86.9%

increase from 0.25 m s^{-1} to 1.0 m s^{-1} in Scenario 2. This implies that η is positively correlated with an increased liquid phase velocity and a shortened light/dark cycle, both induced by the increasing gas inflow rate. When comparing the two scenarios, it is seen that the correlation between η and gas inflow rate is also dependent on the PBR geometry. This is understandable as fluid dynamics are influenced by the reactor configuration.

In theory, it is more appropriate to correlate the effective light coefficient with *Re*. However, as it is difficult to directly calculate *Re* for a multiphase system, in practice it is more convenient to correlate the effective light coefficient with gas inflow rate which fundamentally governs the PBR fluid dynamics. Therefore, Eqs. (3.17) and (3.18) are proposed from the fitting results of Figure 7a and b to correlate effective light coefficient η and gas inflow rate u for the two scenarios respectively.

$$\eta = 0.606 \cdot \left(\frac{u}{u_0}\right)^{1.890} + 1.387 \tag{3.17}$$

$$\eta = 1.128 \cdot \left(\frac{u}{u_0}\right)^{5.095} + 1.328 \tag{3.18}$$

where $u_0 = 1$ m s^{-1} is the reference gas inflow rate.

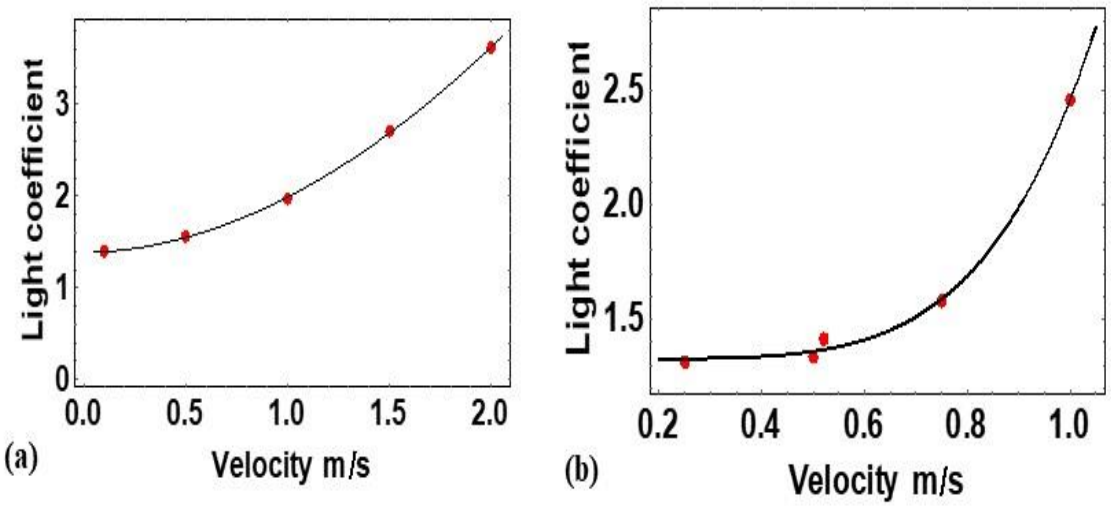

Figure 3.7: Curve fitting result of the correlation between effective light coefficient η and gas inflow rate u for (a) Scenario 1 and (b) Scenario 2. Line: model fitting results, points: process data.

From Eqs. (3.17) and (3.18) and Figure 3.7, three important observations are drawn. Firstly, the correlations between η and u follow a power law expression in both scenarios. This is similar to most correlations used in the field of transport phenomena. For example, power laws are commonly used to correlate mass transfer coefficient with gas inflow rate for gas-liquid reactor simulation as seen in Fujasova et al., and Muocha et al., [167,168], and the power index is determined by the momentum and mass transfer behaviours at a molecular level. Physically speaking, the effective light coefficient represents the significance of local

light transmission (local photons mass transfer) and microbial cells mass transfer, thus the correlation between effective light coefficient and gas inflow rate should obey a power law expression. Secondly, parameters in the two correlations are different as they are dependent on the PBR geometry and power input. This is also similar to the mass transfer coefficient in a gas-liquid reactor as the power index corresponding to gas inflow rate and power input can vary over twice if the impeller configuration is different as interpreted from Fujasova et al., [167]. Thus, calibration must be carried out when applying the current correlation to other PBRs (e.g., different configurations, scale and sizes, and operational parameters like light intensity, bubble diameter). Finally, although they are not estimated in this study, there exists an upper bound of gas inflow rate beyond which the correlation will be invalid. This is either attributed to the fact that an increasing gas inflow rate will cause a higher shear stress which in turn leads to cell decay as investigated by Leupold et al., [163], or the fact that the culture mixing pattern has been changed. Therefore, future work should also pay attention to the valid range of this correlation.

3.3.5 Controlling PBR operation

Increasing incident light intensity (offsetting light attenuation) and enhancing culture mixing (shortening light/dark cycles) are two strategies to facilitate biomass growth in a PBR as reported by Schulze et al., [169]. Although model based optimal control of light intensity has been reported previously by Del Rio-chanona et al., and Koller et al., [170,171], optimal control of gas inflow rate to enhance culture mixing has never been achieved as such a model was never proposed before.

Therefore, by using Eq. (3.15) it is now possible address this problem. In fact, based on this model, the maximum attainable biomass growth rate for varying light intensity occurs at an optimal effective light coefficient $\eta_{opt} = \sqrt{\frac{k_s k_i}{I_{opt}^2}}$ (see Appendix A). During biomass cultivation, as biomass concentration keeps increasing, the average light intensity I_{ave} inside a PBR becomes time-dependent. To ensure a maximum biomass growth rate, the optimal gas inflow rate can be controlled by using the power law correlation (e.g., Eq. (3.17)) with a given $\eta_{opt} = \sqrt{\frac{k_s k_i}{I_{ave}^2}}$. Biomass concentration and average light intensity can be directly calculated using Eqs. (3.15) and (3.13), respectively. In this way, cells can always maintain a high growth rate and the presence of dark region will not significantly restrict biomass growth.

3.4 Conclusion

In this study, the biological meaning of k_s and k_i in the Aiba model are clarified. Based on this knowledge, an effective light coefficient was proposed and embedded into a macroscopic biokinetic model to account for the effect of light/dark cycles on biomass growth. To estimate its value, a novel multiscale modelling strategy was developed to greatly reduce the computational time cost, meanwhile guaranteeing high simulation accuracy. Most importantly, the physical insight, practical applicability, and current limitations of the proposed effective light coefficient were thoroughly discussed. By correlating the effective light coefficient with PBR gas inflow rate, it is now feasible to optimally control the gas inflow rate at each time to maximise cell growth and mitigate light attenuation for biomass cultivation. Considering the early stage of this research and simplifications (e.g., sufficient nutrient supply, constant culture physical properties, fixed PBR configurations) used for theoretical derivation, more thorough investigation will be conducted in the future work to generalise the applicability of current work for PBR design, upscaling and real-time control.

Acknowledgement

Mr. B. Anye Cho is fully funded by the Commonwealth Scholarship Commission, United Kingdom.

Appendix A: derivation of the optimal effective light coefficient, η_{opt}

Using Eq. (3.9), the optimal effective light coefficient, η_{opt} is identified where the biomass growth rate is at the optimum , μ_{opt} (i.e., $\frac{\mathrm{d}\mu}{\mathrm{d}I} = 0$ at I_{opt})

$$\mu = \mu_m \frac{I}{k_s\left(\frac{1}{\eta}\right) + \frac{I}{1} + \frac{I^2}{k_i\left(\frac{1}{\eta}\right)}} \tag{A1}$$

$$\frac{\mathrm{d}\mu}{\mathrm{d}I} = \frac{\mu_m\left[k_s\left(\frac{1}{\eta_{opt}}\right) + \frac{I_{opt}}{1} + \frac{I_{opt}^2}{k_i\left(\frac{1}{\eta_{opt}}\right)}\right] - \mu_m I_{opt}\left[1 + \frac{2I_{opt}}{k_i\left(\frac{1}{\eta_{opt}}\right)}\right]}{\left[k_s\left(\frac{1}{\eta_{opt}}\right) + \frac{I_{opt}}{1} + \frac{I_{opt}^2}{k_i\left(\frac{1}{\eta_{opt}}\right)}\right]^2} = 0 \tag{A2}$$

$$\mu_m\left[k_s\left(\frac{1}{\eta_{opt}}\right) + \frac{I_{opt}}{1} + \frac{I_{opt}^2}{k_i\left(\frac{1}{\eta_{opt}}\right)}\right] = \mu_m I_{opt}\left[1 + \frac{2I_{opt}}{k_i\left(\frac{1}{\eta_{opt}}\right)}\right] \tag{A3}$$

$$k_s\left(\frac{1}{\eta_{opt}}\right) = \frac{I_{opt}^2}{k_i\left(\frac{1}{\eta_{opt}}\right)} \tag{A4}$$

$$\eta_{opt} = \sqrt{\frac{k_s k_i}{I_{opt}^2}} \tag{A5}$$

In Eq. (A5), I_{opt} is calculated with Eq. (3.13) by integrating over the PBR's light path length, z resulting in the following equation:

$$I_{opt} = I_{ave} = \frac{I_0}{\left(\frac{3 \cdot \varepsilon_G}{d_b} + \tau \cdot X\right) \cdot Z}\left(1 - exp\left[-\left(\frac{3 \cdot \varepsilon_G}{d_b} + \tau \cdot X\right) \cdot Z\right]\right) \tag{A6}$$

Chapter 4

Dynamic Modelling of *Rhodopseudomonas palustris* Biohydrogen Production: Perturbation Analysis and Photobioreactor Upscaling

4.1 Preface

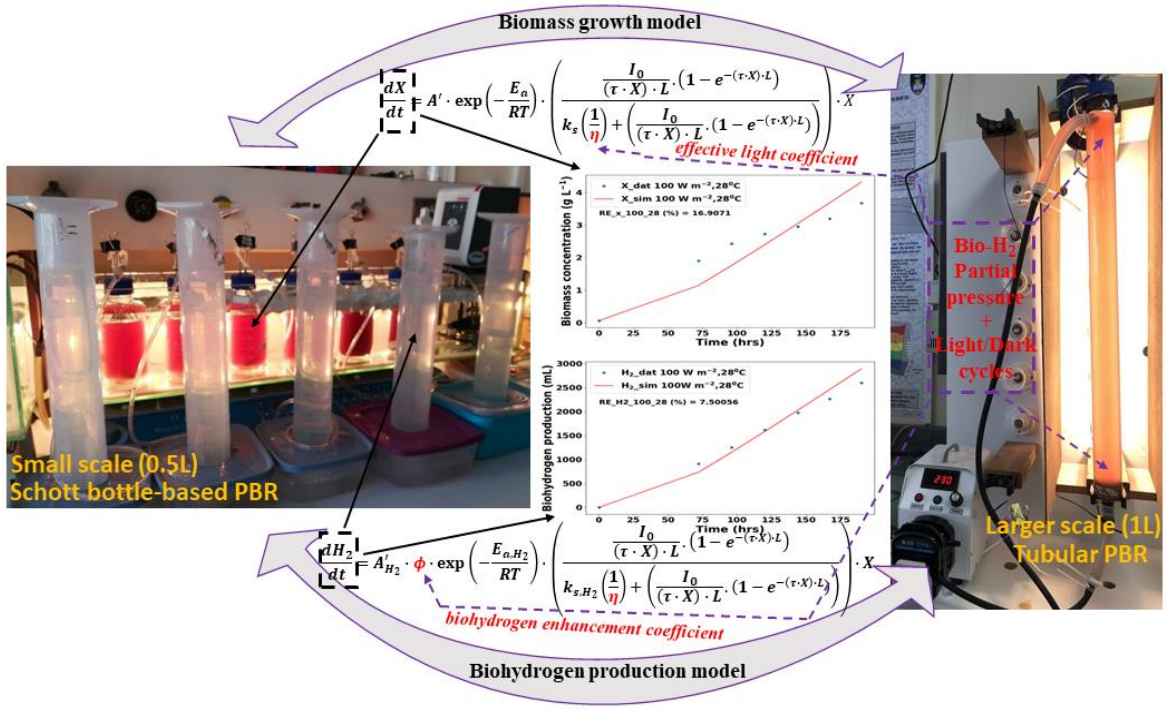

Figure 4.1: Graphical abstract illustrating the model-based across the scale and upscaling prediction capabilities. The smaller scale schott bottle-based photobioreactor is mixed by magnetic stirrers meanwhile the larger scale tubular-based photobioreactor is mixed by peristaltic pumps.

Biohydrogen is a promising alternative to fossil-based fuels (*circa* 80% world's energy consumption) meant for providing clean and renewable energy which is usable for: (i) transportation, (ii) electricity generation, and (iii) heating [1]. Among the several photosynthetic microorganisms which can photosynthesise biohydrogen, the versatile metabolic repertoire of purple-non-sulfur photosynthetic bacterium *Rhodopseudomonas palustris* (referred to as *R. palustris* thereafter) promotes the continuous synthesis in all growth phases, lasting significantly longer than microalgae and cyanobacteria counterparts, thus a promising candidate for upscaling. However, developing biokinetic models for *R.*

palustris under the complicated influences of (i) light intensity, (ii) light attenuation and (iii) temperature, and within different photobioreactors (PBRs) configurations and scales poses a significant challenge.

Therefore, Chapter 4 investigates *R. palustris*'s growth and biohydrogen production in two types of PBRs: schott bottle-based (smaller scale ~ 500 mL) and vertical tubular-based (larger scale ~ 1 mL) as seen in Figure 4.1. From this, a mechanistic model unifying (i) to (iii) for the first time in *R. palustris* and for any other photosynthetic bacteria was proposed. Perturbation analysis was exploited to identify critical parameters influencing the model's accuracy, and two parameters: the *effective light coefficient* (contribution from Chapter 3) and the *biohydrogen enhancement coefficient* (Chapter 4's contribution), both linked to the PBR's transport phenomena were theoretically derived and put forward for recalibrations during PBR scale-up predictions. As well, the systematic approach was valid for when making predictions across different PBR configurations.

The comprehensive details of the published paper as presented in Chapter 4 is structured as follows: Section 4.1 introduces the study; Section 4.2 presents the experimental setup and methodologies for biokinetic model construction, model parameter estimation, perturbation analyses and upscaling predictions; Section 4.3 then presents the model validation results and discussions for *R. palustris*'s higher biohydrogen production yields and upscaling predictions; finally, Section 4.4 concludes the current study.

4.2 Publication 2

Bovinille Anye Cho[1], Brandon Sean Ross[2], Jan-Pierre du Toit[2], Robert William McClelland Pott[2], Ehecatl Antonio del Río Chanona[3], Dongda Zhang[1]. Dynamic modelling of *Rhodopseudomonas palustris* biohydrogen production: Perturbation analysis and photobioreactor upscaling. Int J Hydrogen Energy 2021;46:36696–708. https://doi.org/10.1016/j.ijhydene.2021.08.162

1. Department of Chemical Engineering and Analytical Science, University of Manchester, the Mill, Sackville Street, Manchester, M1 3AL, UK.
2. Department of Process Engineering, University of Stellenbosch, Banghoek road, Stellenbosch, 7599, South Africa.
3. Department of Chemical Engineering, Imperial College London, South Kensington Campus, London SW7 2AZ, UK.

Bovinille Anye Cho's contributions included construction of the mechanistic model, dynamic model parameter estimations, proposing design of experiments, analysing of the generated data and results, and drafting of the manuscript and manuscript revision for important intellectual content. Brandon Sean Ross, Jan-Pierre du Toit, and Robert William McClelland Pott performed the *R. palustris* cultivation experiments at different light intensity and temperatures. Robert William McClelland Pott also revised the manuscript. Ehecatl Antonio del Río Chanona revised the manuscript and provided valuable insights into the project development strategy. Dongda Zhang critically revised the manuscript for important intellectual content, oversaw the project direction, and gave the final approval of the article.

Abstract

Developing kinetic models to simulate *Rhodopseudomonas palustris* biohydrogen production within different configurations of photobioreactors (PBRs) poses a significant challenge. In this study, two types of PBRs: schott bottle-based and vertical tubular-based, were investigated, and three original contributions are presented. Firstly, a mechanistic model was constructed to simulate effects of light intensity, light attenuation, and temperature on biomass growth and biohydrogen synthesis, previously not unified for photosynthetic bacteria. Secondly, perturbation analysis was exploited to identify critical parameters influencing the accuracy of the model. Thirdly, two parameters: *effective light coefficient* and *biohydrogen enhancement coefficient*, both linked to the PBR's transport phenomena were proposed for process scale-up prediction. By comparing against experimental data, the model's accuracy was confirmed to be high. Moreover, the enhancement of biohydrogen production rate by improved culture mixing and gas removal was also described mechanistically. This provides important advances for future efficient design of PBRs and process online optimisation.

Keywords: biohydrogen production; purple non-sulphur bacteria; photobioreactor; kinetic modelling; upscaling.

4.1 Introduction

Biohydrogen is one of the biofuels identified as a promising alternative to fossil-based fuels (*circa* 80% world's energy consumption) for providing clean and renewable energy meant for: (i) transportation, (ii) electricity generation, and (iii) heating [1]. The reasons include but are not limited to: (i) liberating only pure water and energy during combustion with oxygen, (ii) high energy yield per unit mass (122 KJ g^{-1}), approximately 2 to 3 times greater than that of hydrocarbons (e.g. petrol) [172,173], (iii) ambient synthesis conditions which require relatively low energy input, and (iv) able to use various waste materials which facilitate waste recycling in the process of bioremediation [172–174].

Although biohydrogen can be produced by several species of photosynthetic microorganism for example microalga *Chlamydomonas reinhardtii* [68,175,176] and cyanobacterium *Cyanothece sp*. [1,177,178], the purple-non-sulfur photosynthetic bacterium *Rhodopseudomonas palustris* (referred to as *R. palustris*) has been identified as a promising candidate. This is due to: (i) a versatile metabolic repertoire capable of consuming a wide variety of organic substrates such as simple sugars to short chain fatty acids [179], including those toxic to other microorganisms [180,181]; (ii) continuous synthesis of biohydrogen during all growth phases, including the stationary phase [35] which has been observed to last significantly longer than microalgae and cyanobacteria species under anaerobic conditions, (iii) an active photosystem even under changing daily irradiance levels and spectral bands [19], thus comparatively suitable for outdoor cultivation; and (iv) oxygen-induced nitrogenase repression is not a concern since the photo-fermentation process is anoxygenic [40].

Despite these benefits and the impending hydrogen economy, biological hydrogen production with *R. palustris* in photobioreactors (PBRs) has been mostly carried out at laboratory scale [35,149,182,183] and to a lesser extent at pilot scale [17,19], but remains pending at industrial scale. To facilitate experimental design and process upscaling, mathematical models are valuable tools that can accurately describe bioprocess kinetics under influences of cultivating factors like pH, nutrient composition, temperature, and light intensity. However, the inherent complex model structures involved when simultaneously incorporating all these factors has limited literature studies to a few factor investigations. For example, the authors Zhang et al., [35] investigated the effects of nutrient composition via the optimal ratio of nitrogen source to organic carbon source (N/C ratio) with piece-wise Droop and Contois models meanwhile the pH, incident light intensity and temperature effects on the maximum specific growth rate were investigated by Wang et al., [184] with an empirical formula for *R. palustirs.*

As per other related photosynthetic bacteria, the authors Kaftan, Bína, and Koblížek [185] investigated the temperature effects with Arrhenius models for *Rhodospirillum rubrum*, meanwhile Palamae et al., [120] investigated light intensity and light attenuation with Beer Lambert equation for *Rhodobacter sphaeroides*. Obeid et al., [186] investigated the effects of incident light intensity on biohydrogen production using *Rhodobacter capsulatus*. These studies adds to others which have approximated the curves of biomass concentration and biohydrogen production with empirical equations such as the logistic model and the Gompertz equation for *Rhodopseudomonas faecalis* [187], *Rhodobacter sphaeroides*, [188,189], *R. palustris* [60,190], and *Rhodobacter capsulatus* [191]. Despite the reported acceptable model fitting results (i.e., $R^2 > 0.9$), these investigations were laboratory based as the PBRs ranged between 100 mL to 1.1 L, and no upscaling predictions were attempted using the models developed.

A possible reason for this is that, these studies employed empirical models which are eminently challenging to be modified when trying to incorporate more physical/biological knowledge for upscaling modelling. Even so, two of the most important factors, namely temperature and light intensity [192] (including light attenuation herein - a phenomenon responsible for the decrease in light transmission within PBRs because of cellular absorption and scattering) have never been coupled in a mechanistic model of photosynthetic bacteria in general and *R. palustris* in particular. Such a detailed mechanistic model for *R. palustris* would have varying components with different time scales (e.g., slow biomass growth versus fast nutrient consumption rates), thus classified as stiff systems, whereby parameter estimation is a challenging task [35]. Although solvable with least-square principles and advanced discretisation schemes like orthogonal collocation [127], the nonlinearities associated with kinetic model structures is a reoccurring dilemma to be addressed. In the literature [105], decoupling the problem into separate parameter estimation problems (i.e., temperature versus light effects) and solving the parameters stepwise (i.e., initially excluding temperature effects to solve the light-dependent parameters followed by including temperature-dependent parameters) is recommended.

Also, scale-up studies with such mechanistic models are indispensable for fast-paced and cost-effective development of any microbial process. However, the biological activities of these microorganisms are strongly coupled to the local environmental conditions (i.e., light attenuation, nutrient and pH gradients, etc.) which are influenced by transport phenomena to a greater extent and are bioreactor scale dependent. For instance, the authors Imamoglu and Sukan [193] reported an increase of 1.8 times and 88% for biomass and bio-ethanol production, respectively, for a 10 L bioreactor compared with that of a shaken flask or

intermediary bioreactors (i.e., 2 L and 5 L) despite upscaling under constant impeller tip speed of the agitator. Similarly, Lu et al., and Ziadi et al., [17,194] also observed a comparable increase in productivity upon upscaling. These results indicate that empirical biokinetic model parameters are scale-dependent and should be re-estimated before applied for process upscaling prediction.

To resolve the aforementioned challenges, this article aims to: (i) construct an accurate kinetic model capable of simulating biomass growth and biohydrogen production of *R palustris* under the influences of light intensity, light attenuation and temperature, and (ii) evaluate its applicability when simulating process dynamics over different scales and configurations of PBRs.

4.2 Methodology

4.2.1 Experimental setup

The small (500 mL) and large (1,000 mL) scale photobioreactors (PRRs) employed, namely, the schott bottle-based PBR and vertical tubular-based PBR are illustrated in Figure 4.2, whilst details of their schematics, construction and modes of operation are provided in the respective papers [149,180]. The light path lengths of the small and large scale PBRs were 86 mm and 50 mm, respectively. The pH of the growth medium in both PBR operations were adjusted using HCl and NaOH to a fixed value of 7.0 ± 0.1. Unidirectional illumination was provided by tungsten lighting bulb (100 W) at two light intensities: 100 Wm^{-2} and 200 Wm^{-2}. These light intensities were arrived at by adjusting the distance between the tungsten lighting bulb (100 W) and the PBR front surface to the corresponding values detected by a compact spectrometer (RGB photonics Qmini VIS-NIR). The two light intensities were both used in the small scale PBR to establish the biokinetic model whilst only 100 Wm^{-2} was employed for upscaling application in the large scale PBR due to its narrower light path length. Similarly, the small-scale PBR was operated at 28℃, 30℃, 35℃ and 40℃, controlled within ±0.2℃ using a water bath whilst the large scale PBR was operated at a fixed value of 28℃ with air conditioning of the room. The experimental analytic methods and essays for quantifying (i) biomass concentration, (ii) substrate (glycerol) concentration, and (iii) biohydrogen collection and purity analysis, has already been detailed in [149,180], and are thus not repeated here.

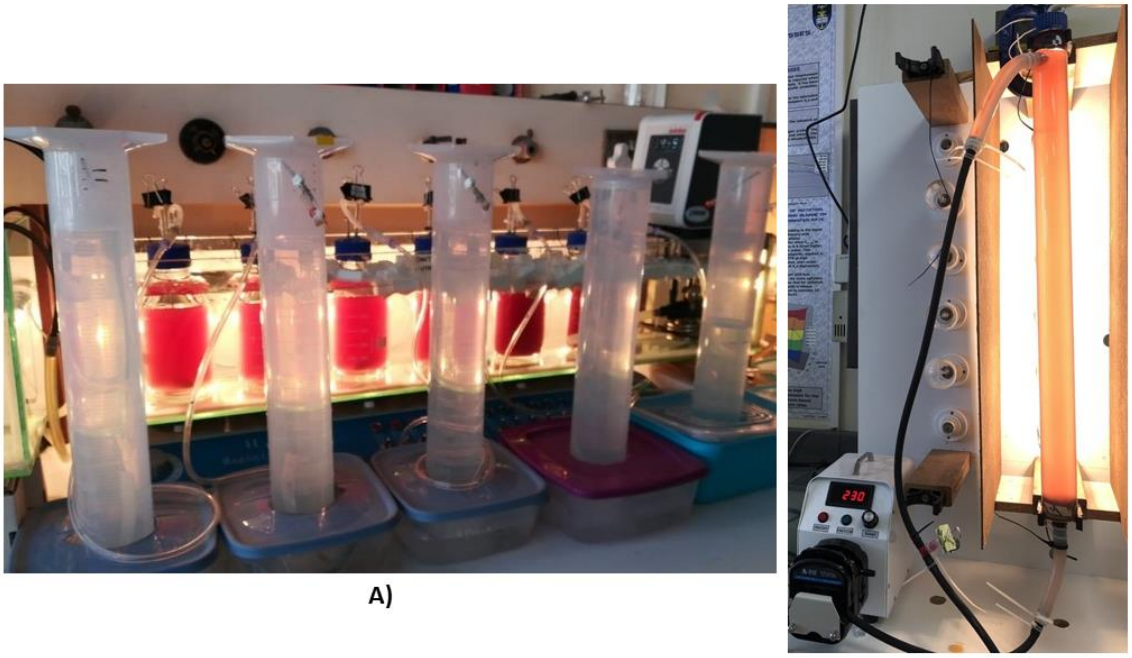

A) B)

Figure 4.2: Photobioreactor (PBR) used herein: A) small scale PBR with magnetic stirrer driven mixing, and B) large scale PBR with peristaltic pump driven mixing in the work of Ross-Pott [149] specific to only planktonic operation used herein.

4.2.2 Biokinetic model construction

The kinetic model constructed in this work will be used to simulate photo-heterotrophic biomass growth and biohydrogen production under the influences of (i) light intensity, (ii) light attenuation, and (iii) temperature.

4.2.2.1 Biomass growth

The growth rate of *R. palustris* biomass with an assumption of negligible cell death is described by Eq. (4.1). The substrate concentration S, was always in excess (i.e., > 20 mM at the end each batch) indicating that it was not a limiting factor for biomass growth. Therefore, the biomass growth rate in this study was independent of S.

$$\frac{dX}{dt} = \mu_{max} \cdot \mu(T) \cdot \mu(I) \cdot X \tag{4.1}$$

where X is the biomass concentration (g L^{-1}), μ_{max} is the maximum specific growth rate (h^{-1}), $\mu(T)$ and $\mu(I)$ denote the respective effects of temperature (T) and light intensity (I) on biomass growth.

4.2.2.2 Glycerol consumption

Substrate consumption rate is described by Eq. (4.2) and is characterised by Y_{XS} and m as the substrate yield coefficient (mmol g^{-1}) and maintenance coefficient (mmol g^{-1} h^{-1}), respectively.

$$\frac{dS}{dt} = -Y_{XS} \cdot \frac{dX}{dt} - m \cdot X \tag{4.2}$$

4.2.2.3 Biohydrogen production

Biohydrogen production by *R. palustris* and some photosynthetic bacteria are often modelled in the literature using the Luedeking-Piret model [35,60,186]. The model assumes biohydrogen formation to be linearly associated with both biomass growth rate and instantaneous biomass concentration (i.e., growth-independent) as seen in Eq. (4.3a). However, the effects of light intensity and temperature remain unaccounted for in Eq. (4.3a), leading to the construction of Eq. (4.3b) by combining Eq. (4.1) with Eq. (4.3a) when the light intensity and temperature effects are associated to Y_{XH_2} and Y_{H_2} in the form of $Y_{XH_2}(I,T)$ and $Y_{H_2}(I,T)$.The reader is referred to Appendix B of the supplementary sheet for the full derivation.

$$\frac{dH_2}{dt} = Y_{XH_2} \cdot \frac{dX}{dt} + Y_{H_2} \cdot X \tag{4.3a}$$

$$\frac{dH_2}{dt} = \alpha_{max} \cdot \alpha_{H_2}(T) \cdot \alpha_{H_2}(I) \cdot X \tag{4.3b}$$

where H_2 is biohydrogen production (mL), Y_{XH_2}(mL H_2 L g^{-1}) and Y_{H_2} (mL H_2 L g^{-1} h^{-1}) are growth-dependent and growth-independent yield coefficient, respectively, α_{max} is the maximum specific H_2 production rate (h^{-1}) while $\alpha_{H_2}(T)$ and $\alpha_{H_2}(I)$ the respective effects of temperature (*T*), light intensity (*I*) on biohydrogen production, respectively.

4.2.2.4 Simulation of temperature influences

The influences of temperature on microbial processes are commonly modelled with the Arrhenius equation (Eq. (4.4a) and (4.4b)). Although there exists an optimal temperature beyond which microbial metabolism activity will decrease, in this study, the operating temperature did not exceed this value (i.e., 313.15 K) for *R. palustris* biomass growth [180]. Thus, it is valid assuming a monotonic increase over the temperature range explored in this work.

$$\mu(T) = A \cdot \exp\left(-\frac{E_a}{RT}\right) \tag{4.4a}$$

$$\alpha_{H_2}(T) = A_{H_2} \cdot \exp\left(-\frac{E_{a,H_2}}{RT}\right) \tag{4.4b}$$

where *A* and A_{H_2} are pre-exponential coefficients (h^{-1}) for biomass growth and biohydrogen production, respectively. E_a and E_{a,H_2} are the activation energies (J mol^{-1}) for cellular multiplication and biohydrogen biosynthesis. *R* the is universal gas constant (8.3145 J $mol^{-1}K^{-1}$) and *T* is the absolute temperature (K).

When Eqs. (4.4a) and (4.4b) are substituted in Eqs. (4.1) and (4.3b), the multiplicative terms (i.e., $\mu_{max} \cdot A$ and $\alpha_{max} \cdot A_{H_2}$) are observed. As these terms are mathematically unidentifiable, they are lumped as A' (h^{-1}) and A'_{H_2}(h^{-1}), respectively, to form identifiable parameters.

4.2.2.5 Simulation of light intensity and light attenuation influences

Light is an obligate requirement for biomass growth and biohydrogen production by *R. palustris*. Its effects have been extensively studied in literature with photolimitation, photosaturation and photoinhibition being the main photo-mechanisms of interest [120]. The former occurs under low light intensity, the second under optimal light intensity and the latter under intense light intensity. The Aiba model (Eqs. (4.5a) and (4.5b)) captures the dynamic nature of these photo-mechanisms but the photoinhibition term is neglected here. This is because the light intensities investigated within this study were not higher than 200 Wm^{-2}, as photoinhibition was not observed in a similar purple non-sulfur photosynthetic bacterium *Rhodobacter sphaeroides* O.U. 001 for light intensities between 150 W m^{-2} - 250 W m^{-2} [188,195].

$$\mu(I) = \frac{I}{I + k_s + \frac{I^2}{k_I}} \approx \frac{I}{I + k_s} \tag{4.5a}$$

$$\alpha_{H_2}(I) = \frac{I}{I + k_{s,H_2} + \frac{I^2}{k_{I,H_2}}} \approx \frac{I}{I + k_{s,H_2}} \tag{4.5b}$$

where k_s and k_{s,H_2} are light saturation coefficients (W m^{-2}) for biomass growth and biohydrogen production, respectively. Similarly, k_I and k_{I,H_2} are light inhibition coefficients (W m^{-2}).

Since the PBRs were illuminated uni-directionally, the front-face section of the PBRs experienced a higher local light intensity compared to the rear, particularly as the biomass concentration increased over time. The resulting non-uniform light exposure caused by microbial absorption can be approximated using Eq. (4.6). Although light scattering can be another contributing factor, it effects were neglected in this case since the PBRs were not mixed by aeration, thus the effects of light scattering were omitted. The simplifications in Eq. (4.6) are convenient for dynamic parameter estimation without compromising the high accuracy compared to other complicated light transmission models like the two-flux approximation of the radiation transfer equation [73,196].

$$I(l) = I_0 \cdot \mathrm{e}^{(-\tau \cdot X \cdot l)} \tag{4.6}$$

where $I(l)$ and I_0 are the local and incident light intensity (Wm^{-2}), respectively, τ ($m^2\ g^{-1}$) is the light absorption coefficient, l (m) is the light path length.

Due to the PBR's cylindrical geometry and impact on Eq. (4.6) during parameter estimation (i.e., solving Eqs. (4.8a) to (4.8e) below), curvature effects were approximated by taking the rectangular cross-sectional area as reported in [120]. In addition, embedding Eq. (4.6) into Eq. (4.1) introduces a partial differential equation (PDE) given by the presence of both temporal and spatial dimensions. To simplify the model complexity, Eq. (4.6) was used to calculate the average light intensity (Eq. (4.7)) in order to eliminate the spatial dimension [197,198]. Hence, Eq. (4.7) is then substituted into Eqs. (4.5a) and (4.5b) for the remainder of the study.

$$I_{ave} = \frac{\int_0^L I(l)dl}{L} = \frac{I_0}{(\tau \cdot X) \cdot L} \cdot (1 - e^{-(\tau \cdot X) \cdot L}) \tag{4.7}$$

where L is the length of the PBR.

4.2.3 Parameter estimation

The constructed kinetic model has several parameters to be estimated. Given the high nonlinearity, parameters in the biomass growth and substrate consumption equations were first calculated, followed by those in the biohydrogen production equation. Parameter estimation was solved by a weighted nonlinear least-square regression (see Eqs. (4.8a) to (4.8e)).

$$\min_P \Phi(\boldsymbol{p}) = \sum_{j=1}^{N} \sum_{i=1}^{NP} \left(\frac{\hat{y}_{i,j} - y_j(t_i, \boldsymbol{p})}{\hat{y}_{i,j}} \right)^2 \cdot w_i \tag{4.8a}$$

Subject to:

$$\frac{d\boldsymbol{y}}{dt} = f(\boldsymbol{y}(t), p)\,, \qquad t \in [t_0, t_f] \tag{4.8b}$$

$$\boldsymbol{y_{lb}} \leq \boldsymbol{y} \leq \boldsymbol{y_{ub}} \tag{4.8c}$$

$$\boldsymbol{p_{lb}} \leq \boldsymbol{p} \leq \boldsymbol{p_{ub}} \tag{4.8d}$$

$$\boldsymbol{y}(t_0) = \boldsymbol{y_0} \tag{4.8e}$$

where $\boldsymbol{p}$ is a vector of parameters, N and NP are the number of state variables (e.g. concentrations of biomass, substrate, product) and experimental data points, respectively, $\boldsymbol{y}$ is dynamic model output, $\hat{y}_{i,j}$ is experimental data point for state variable j at time instant t_i, w_i is a weight for the data point of state variable j at time instant t_i, $\boldsymbol{y_{lb}}$, $\boldsymbol{y_{lb}}$, $\boldsymbol{p_{lb}}$ and $\boldsymbol{p_{ub}}$ are the lower and upper bounds for the state variables and parameters, respectively, t_0 and t_f

are the initial and final cultivation time while $\boldsymbol{y_0}$ is the initial concentration of the state variables.

As per the literature approach [105], temperature effects were excluded (i.e., constants: $\mu_{T=303.15\,K}$, $\mu_{T=308.15\,K}$, and $\mu_{T=313.15\,K}$) initially in order to solve for the light-dependent parameters (i.e., k_s, τ, Y_{XS} and m) using the biomass and substrate models as an example. Then, temperature-dependent parameters (i.e., A' and E_a) were estimated via nonlinear curve fitting with Eq. (4.4a) using the data from step one (i.e., $\mu_{T=303.15\,K}$, $\mu_{T=308.15\,K}$, and $\mu_{T=313.15\,K}$). This results in a complete solution of the biomass and substrate kinetic models constituting the first part of the decoupled system pending the biohydrogen model. The aforementioned methodology is then repeated for the coupled system (i.e., biomass, substrate and biohydrogen models), however, the optimal solution (estimated parameters values) of the first part is now fixed when estimating the biohydrogen model parameters.

Considering the stiffness and nonlinearity of the proposed kinetic model, orthogonal collocation over finite elements in time was used to discretise the differential equations thereby transforming them into a series of nonlinear algebraic equations [127]. The nonlinear optimisation problem was now solved with an interior point solver (i.e., IPOPT [199]) via an open-source interface Pyomo [200] within Python version 3.7 programming environment.

4.2.4 Perturbation analysis

Parameters in a biokinetic model often have large uncertainties [124]. To understand how the model's prediction uncertainty is affected by its parameters' uncertainty, perturbation analysis was carried out in this study. In Table 4.1, parameters are grouped into three classes where the input space was characterised by a lower (p_{min}) and upper (p_{max}) bound centered on the mean parameter (p_{mean}) value as defined by Eqs. (4.9a) and (4.9b). Latin Hypercube Sampling (LHS) was used for the probabilistic sampling of the input space where each sample was then used to perform dynamic model simulation. All codes were executed in Python version 3.7 using the *SMT* 1.0.0, *NumPy* and *SciPy* libraries.

Table 4.1: Parameter class and input uncertainty allocations.

Parameters	Class	Units	Expert Knowledge Justification
Y_{XS}	I	mmol g^{-1}	Reaction conversion related parameters are often well-known with great accuracy from microbiological studies [201,202].
m	I	mmol g^{-1} h^{-1}	
k_s	II	Wm^{-2}	
k_{s,H_2}	II	Wm^{-2}	

τ	II	$mm^2\ g^{-1}$	Light intensity associated parameters are often identifiable in the literature [203] to acceptable fidelity.
A'	III	h^{-1}	Arrhenius (temperature associated) parameters are poorly known in the literature. Identifiability issues are recorded, with the parameter confidence intervals rarely reported [102,204]
E_a	III	$J\ mol^{-1}$	
A'_{H_2}	III	h^{-1}	
E_{a,H_2}	III	$J\ mol^{-1}$	

$$P_{min} = (1 - \%Varation) \cdot P_{mean} \tag{4.9a}$$

$$P_{max} = (1 + \%Varation) \cdot P_{mean} \tag{4.9b}$$

2.5 Large scale PBR simulation

Transport phenomena and light transmission greatly affect the performance of PBR scale-up. Since biomass growth was independent of substrate concentration herein, local light/dark cycle frequency is the only factor influenced by transport phenomena in this study. In our recent study [52], we have found that this effect can be simulated by introducing one additional parameter, namely effective light intensity coefficient, η, which is larger than 1 if culture mixing is intensified in a PBR. Therefore, incorporating this into Eq. (4.5a) results in Eqs. (4.10a) to (4.10c) which will be used to simulate the process dynamics in the large scale PBR. The value of η is determined by PBR configuration and culture mixing intensity. It was estimated in this study via parameter estimation.

$$\frac{dX}{dt} = \mu_{max} \cdot \mu(T) \cdot \mu(I_{ave}, \eta) \cdot X \tag{4.10a}$$

$$\frac{dS}{dt} = -Y_{XS} \cdot \frac{dX}{dt} - m \cdot X \tag{4.10b}$$

$$\mu(I_{ave}, \eta) = \left(\frac{\frac{I_0}{(\tau \cdot X) \cdot L_L} \cdot (1 - e^{-(\tau \cdot X) \cdot L_L})}{k_s \left(\frac{1}{\eta}\right) + \left(\frac{I_0}{(\tau \cdot X) \cdot L_L} \cdot (1 - e^{-(\tau \cdot X) \cdot L_L})\right)} \right) \tag{4.10c}$$

In addition, the biohydrogen production rate is also known to be a function of hydrogen partial pressure since this reaction is reversible [174,205]. As a result, hydrogen removal rate and gas-liquid mass transfer will also affect overall hydrogen production rate. As the vertical tubular PBR has a better mass transfer and gas removal system than that of the schott bottle PBR, it is expected that hydrogen production rate in the tubular PBR is enhanced. Therefore, another parameter namely biohydrogen enhancement coefficient ϕ, was added in Eq. (4.3b)

to take into account this factor when simulating hydrogen production in the tubular PBR (as shown in Eqs. (4.11a) and (4.11b)).

$$\frac{dH_2}{dt} = \phi \cdot \alpha_{H_2}(T) \cdot \alpha_{H_2}(I_{ave}, \eta) \cdot X \tag{4.11a}$$

$$\alpha_{H_2}(I_{ave}, \eta) = \left(\frac{\frac{I_0}{(\tau \cdot X) \cdot L_L} \cdot (1 - e^{-(\tau \cdot X) \cdot L_L})}{k_{s,H_2}\left(\frac{1}{\eta}\right) + \left(\frac{I_0}{(\tau \cdot X) \cdot L_L} \cdot (1 - e^{-(\tau \cdot X) \cdot L_L})\right)} \right) \tag{4.11b}$$

4.3. Results and discussion

4.3.1 Parameter estimation results

Table 4.2 lists the model parameter estimation result through the two-step parameter estimation framework. As there is no previous research developing a kinetic model for *R. palustris*, the values of parameters estimated in this study are compared to other similar photosynthetic bacteria such as *Rhodobacter sphaeroides*, *Rhodobacter capsulatus* and *Rhodospirillum rubrum*. From the table, it is seen that the currently estimated kinetic parameters fall within the same range as these species except for k_s which was about 10 orders of magnitued higher than that reported by Palamae et. al., [120] for *Rhodobacter sphaeroides*.

Table 4.2: Model parameter estimates and literature validation.

Step-one optimisation		
Parameters	Estimated	Literature
$\mu_{T=303.15\,K}$ (h^{-1})	0.159	0.198 to 0.243
$\mu_{T=308.15\,K}$ (h^{-1})	0.185	[120]
$\mu_{T=313.15\,K}$ (h^{-1})	0.225	
k_s (Wm^{-2})	500.0	42.02 (i.e., 2.87×10^4 lux whereby 1 Wm^{-2} = 683 lux) [120]
τ ($mm^2\ g^{-1}$)	90.8	10.2 [120]
Y_{XS} (mmol g^{-1})	9.66	(1.1 to 10) [184,206]
m (mmol $g^{-1}\ h^{-1}$)	0.0140	(0.0 to 0.78) [35]
$\alpha_{T=303.15\,K}$ (h^{-1})	56.9	n/a
$\alpha_{T=308.15\,K}$ (h^{-1})	81.0	
$\alpha_{T=313.15\,K}$ (h^{-1})	106.0	
k_{s,H_2}(Wm^{-2})	500.0	

	Step-two optimisation	
A'(h^{-1})	8.30×10^{3}	n/a
E_a(J mol^{-1})	2.74 ×10^{4}	(1.63×10^{4} to 3.8×10^{4}) [185]
A'_{H_2}(h^{-1})	1.01×10^{10}	n/a
E_{a,H_2}(J mol^{-1})	4.78×10^{4}	
n/a: not available		

Figure 4.3 shows the model fitting result after the first parameter estimation step for 100 Wm^{-2} and 200 Wm^{-2} at 35℃ and 30℃, respectively. This constitutes half of the overall results with the remainder (i.e., 200 Wm^{-2} at 35℃ and 40℃) presented in Figure B 4.8 of the supplementary sheet. The overall average relative percentage error was ranked as 3.06%, 8.68%, and 15.47% for the substrate model, biomass model and biohydrogen model, respectively. Figure 4.4 (a) and (b) shows the model fitting result after the second parameter estimation step.

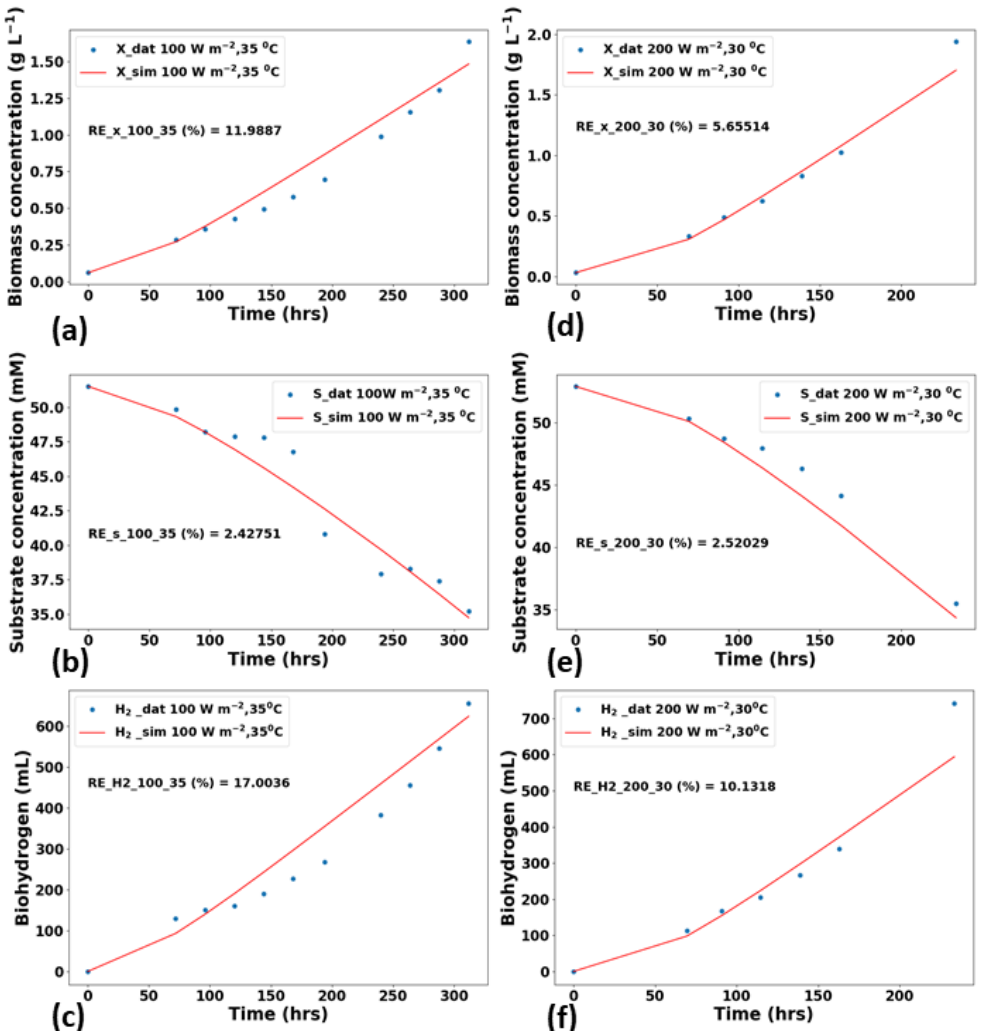

Figure 4.3: Model fitting results for the various state variables at :100 Wm^{-2} at 35℃ (a) to (c), 200 Wm^{-2} at 30℃ (d) to (f). The (a) to (c) and (d) to (f) are state variables corresponding

to the biomass, substrate and biohydrogen models respectively. Each fitting is accompanied by the percentage relative error (%RE).

It is seen in Figure 4.4 (a) and (b) that the specific production rates of biomass and biohydrogen increase with temperature. This can be attributed to temperature enhanced photosynthetic electron transport as reported by [185] from the oxidised organic substrate (i.e., glycerol herein) via the three major metabolic pathways (i) Carbon fixation, (ii) Nitrogen fixation/Hydrogen production, and (iii) biomass biosynthesis [40]. Under such conditions, the ATP flux surpasses the threshold necessary for solely biomass production, leaving the excess to activate the biohydrogen production pathway (i.e., enhanced activity of the nitrogenase) and maintain the cellular redox balance [40]. Thus, both biomass and biohydrogen biosynthesis are significantly enhanced. This finding parallels to that of [180] but now provides an in-depth mechanistic description, quantified by the estimated kinetic model parameters.

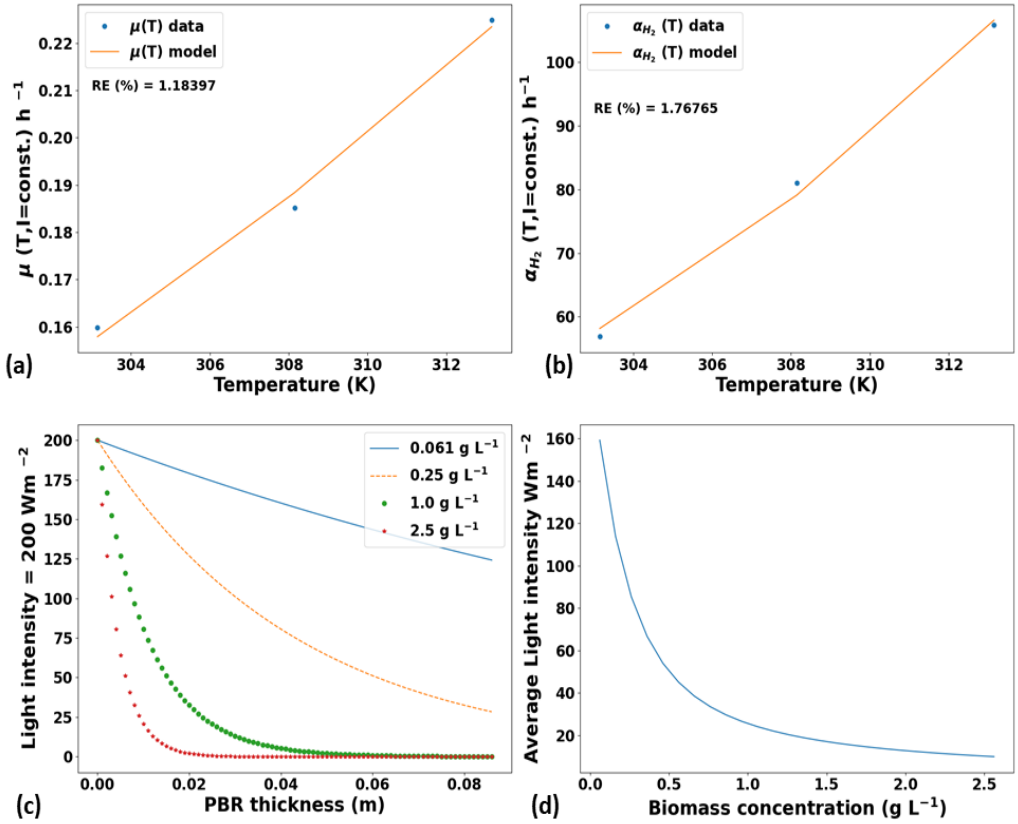

Figure 4.4: Model fitting results for temperature parameters in step two optimisation (a) to (b), and dynamic simulation of light intensity and attenuation influences: (c) to (d).

On the other hand, the enhanced biomass productivity observed at elevated temperatures increases biomass concentration and thus cell mutual shading within the PBR. Therefore, the average light intensity available to drive photosynthesis drops exponentially away from the illuminated surface towards the rear of the PBR according to the Beer-Lambert law. Both

bio-physical phenomena are effectively captured by the mechanistic model (see Figure 4.4 (c) and (d)) where it can be seen that the average light intensity is greatest during inoculation (time, $t = 0$ hrs) when the biomass concentration (X ~ 0.61 g L^{-1}) and cellular absorption are lowest. Conversely, the average light intensity is lowest at the end of the batch (t > 230 hrs) due to a greater biomass concentration (X > 2.5 g L^{-1}) and degree of cellular absorption and mutual shadings. Although, the percentage light captured increases with biomass density, (i.e., light travels through the PBR to other side and is wasted when biomass concentration is low), the small scale PBR's surface area to volume ratio appears sub-optimal with most of the light being attenuated with a few centimeters. An important insight from this is that, optimising this surface area to volume ratio could increase the local light availability leading to the biomass and biohydrogen productivity being further enhanced.

4.3.3 Result of perturbation analysis

The uncertainty bands in Figure 4.5 reflect the degree of variability on model predictions of biomass, substrate and biohydrogen imposed by the different classes of parameters. Each uncertainty class (I to III) was investigated in turn by randomly re-sampling the parameters between P_{min} and P_{max} whilst fixing the parameters from the other two classes. Since the resulting propagated uncertainty bounds were similar across the different experimental conditions studied herein (i.e., light intensities and temperature), for illustration, only the results corresponding to a light intensity of 100 Wm^{-2} at a temperature of 35 ℃ is presented. From Figure 4.5, it can be seen that the propagated uncertainty increases (i.e., size of band width) with time. The model uncertainty is shown to be lowest for Class I parameters (see Figure B 4.9 of the supplementary sheet) but highest (i.e., up to 60%) for Class III parameters. This result suggests that the model is highly sensitive to change of Class III parameters but is less responsive to Class I parameters.

This can be expected as Class I parameters are solely found within the substrate model, in contrast, biomass growth and biohydrogen production are void of them. Consequently, they have negligible impact to the model's uncertainty. In contrast, the largest model prediction uncertainty with Class III parameters for as little as 4% input uncertainty in Figure 4.5 (a) to (c) signifies the highest model sensitivity. This indicates the necessity of designing more experiments (e.g., adding 100 Wm^{-2} at 30℃ and 100 Wm^{-2} at 40℃) in order to accurately identify the values of temperature associated parameters. As the model accuracy is highly sensitive to these parameters, updating Class III parameters for model based process online optimisation may not be a safe strategy considering the level of prediction uncertainty that can be introduced to the model. As a result, their values should be well estimated prior to

the use of the model and then fixed when employing the model for process optimisation. Compared to Class III parameters, Class II parameters can also result in a similar magnitude of model uncertainty if their input uncertainty is around 20% as shown in Figure 4.5 (d) to (f). This implies that these parameters are sensitive enough to affect the model accuracy but the model is also robust to mild changes in these parameters (i.e., small changes in parameters will not cause a significant difference to the model's simulation result). As a result, these parameters are ideal candidates to be re-estimated during online operation if the model is used for dynamic process optimisation.

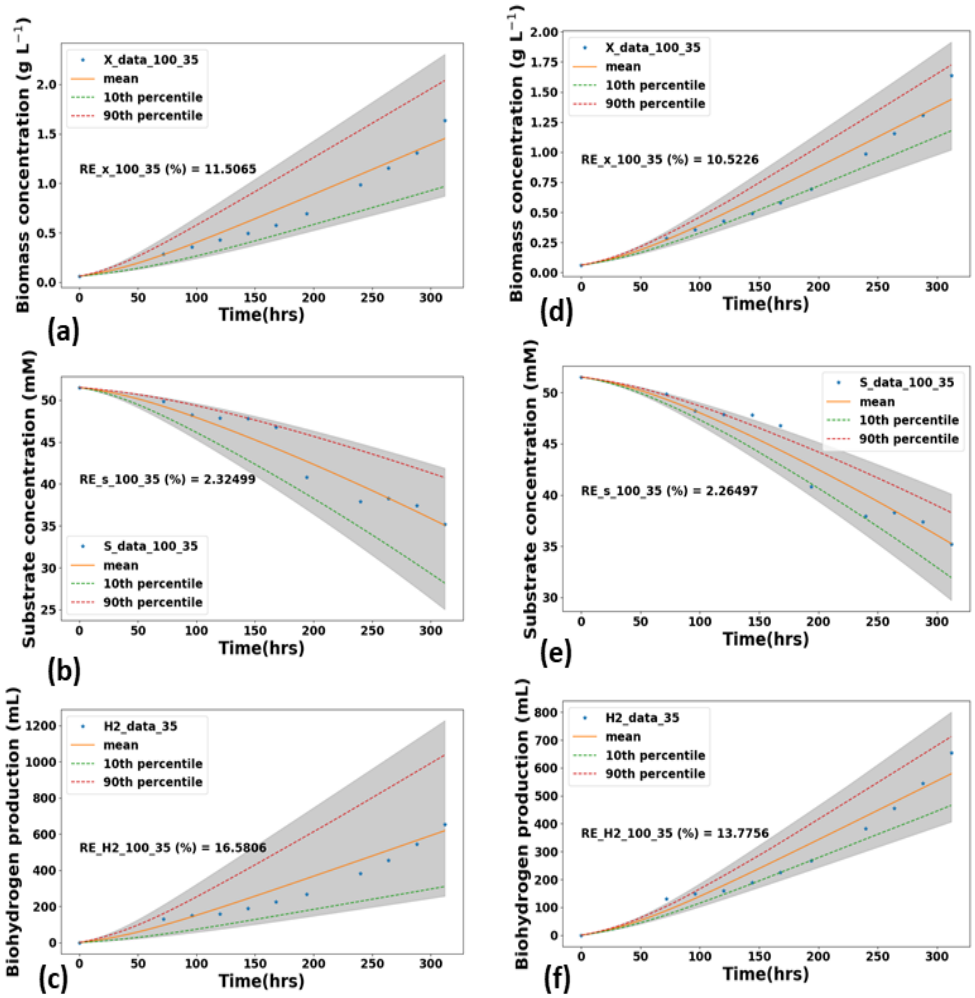

Figure 4.5: Perturbation analysis for input uncertainties of (a) to (c) 4% for class III, (d) to (f) 20% for class II. The mean, 10th and 90th percentile, and % RE for 100 Monte-Carlo simulations. Also, (a) to (c) and (d) to (f) are state variables corresponding to the biomass, substrate and biohydrogen models respectively.

Another result found from the perturbation analysis is that introducing an adequate level of parameter uncertainty may improve the kinetic model's simulation performance. Figure 4.6 shows the averaged model simulation error at different levels of input uncertainty over 100 Monte-Carlo simulations for Class II and Class III parameters. From the figure, it is observed

that the model simulation error is minimum when 5% and 30% input uncertainties are assigned to Class III and Class II parameters, respectively. This suggests that perturbation analysis can be used to determine the adequate level of parameter uncertainty that can be embedded into the model in order to improve its prediction accuracy and estimate its prediction uncertainty. As a result, the use of perturbation analysis for bioprocess robust optimisation will be explored in future research. However, it should be noted that this result has not been reported in other studies, thus further investigation needs to be carried out to understand if this conclusion can be generalised.

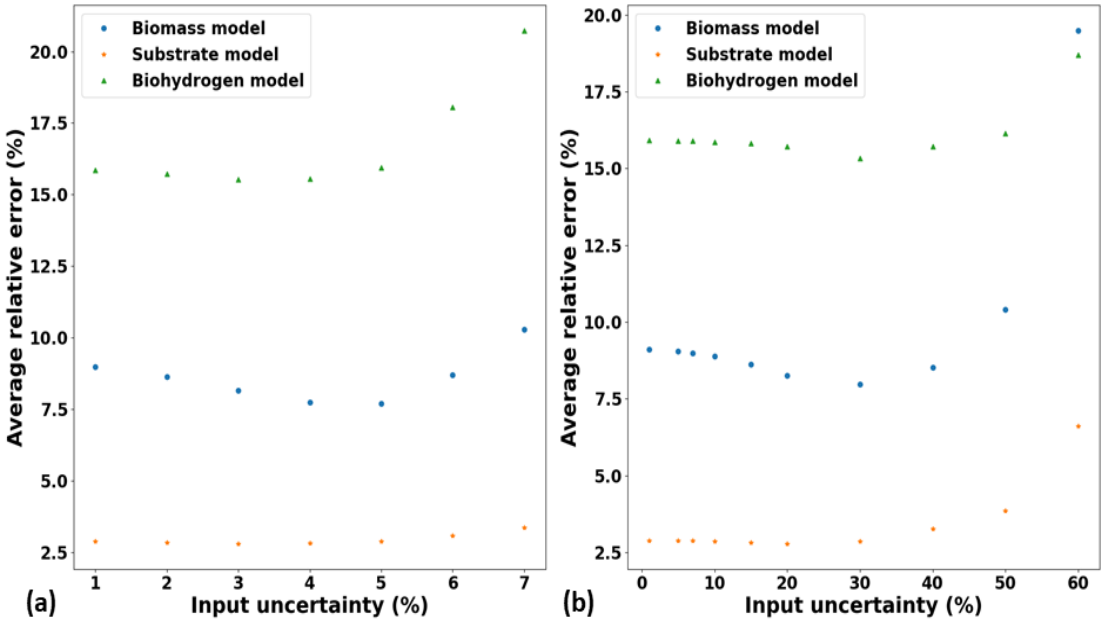

Figure 4.6: Effects of parameter input uncertainty on the model simulation accuracy. (a) Class III and (b) Class II parameters.

3.4 Performance of large scale PBR simulation

Figure 4.7 (a) to (c) shows the simulated and experimental process trajectories for the large scale PBR following estimation of the kinetic parameters (reported in Table 4.3) from the small scale PBR data. From the figure, it is seen that the model can well predict substrate consumption and hydrogen production in the large scale PBR, indicating its potential for large scale system prediction. The highest relative percentage error of 17% was recorded for the upscaled biomass growth model. Despite this being generally acceptable for a highly nonlinear temperature and light-dependent bioprocess, the model simulation error could be attributed to the lack of a decay term in Equation (1). This is evident in the model over-predicting the late exponential growth phase for the upscaled PBR contrary to the slowing biomass growth rate but steady biohydrogen production rate as observed. This phenomenon has been reported by other researchers [35] on the modelled microorganism *R. palustris* as biohydrogen production was observed in all three growth phases (i.e., (i) initial lag, (ii)

primary growth phase and (iii) secondary growth phase). Therefore, more experiments are needed for the incorporation and identification of this decay term which would improve the upscaled model accuracy in describing all three phases.

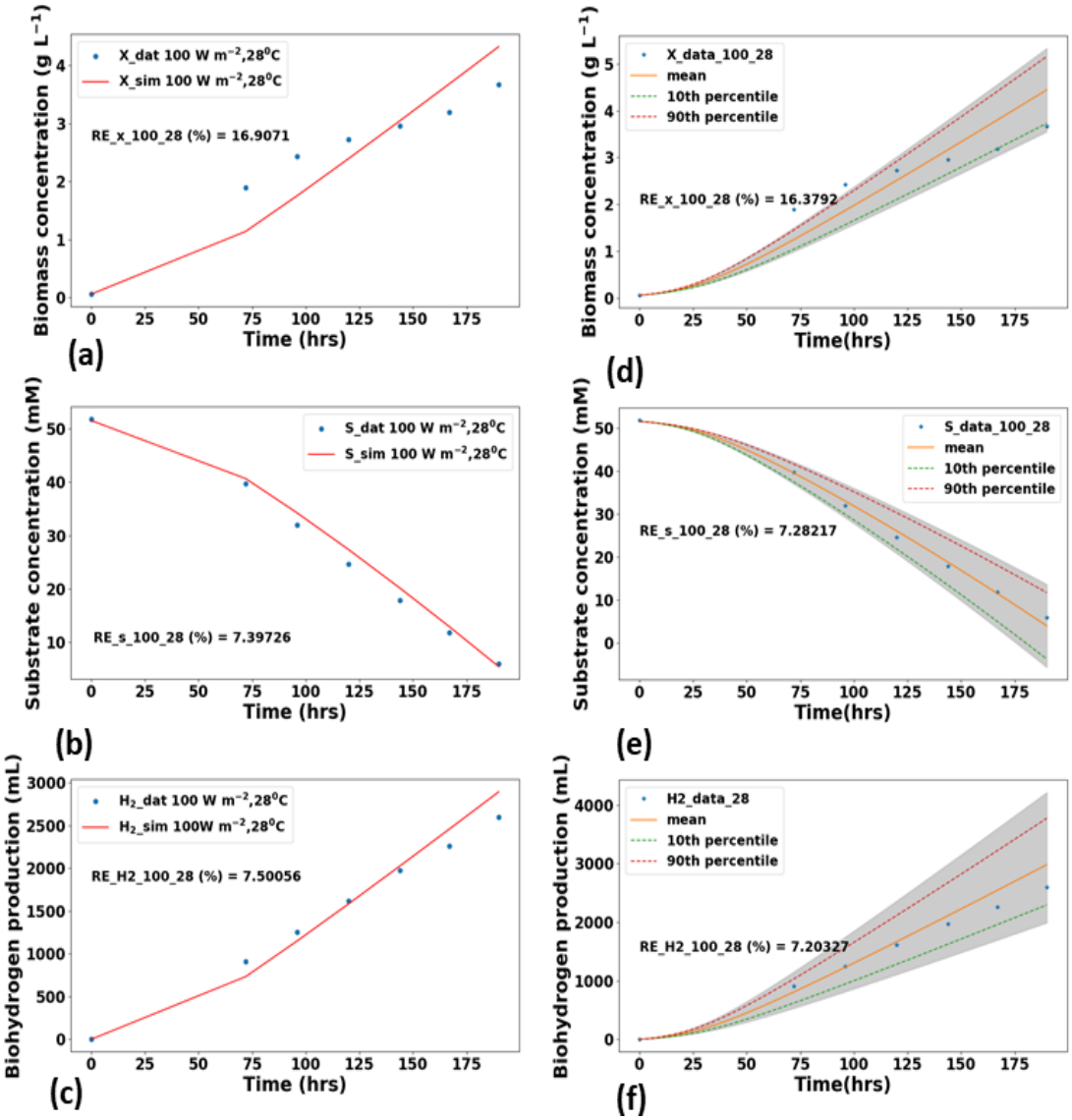

Figure 4.7: Simulation result of the large scale PBR: (a) to (c) and perturbation analysis (d) to (f) of 20% for transport phenomena associated parameters. The mean, 10^{th} and 90^{th} percentile, and %RE for 100 Monte-Carlo simulations. Each fitting is accompanied by the percentage relative error (% RE). Also, (a) to (c) and (d) to (f) are state variables corresponding to the biomass, substrate and biohydrogen models respectively.

Perturbation analysis investigated for the transport phenomena associated parameters at 20% input uncertainties are presented in Figure 4.7 (d) to (f). It is seen that all the state variables (biomass, substrate and biohydrogen models) were sensitive to the transport phenomena associated parameters. This implies that all the state variables are tunable during any re-calibration process for the prediction of a different PBR scale and enables the accurate extrapolations of the new PBR scale when deviations between the state variables and

experimental data are minimised. Contrary to the Class III parameters as seen in Figure 4 for 4% input uncertainty, these sensitives were relativity low and this indicates that the transport phenomena associated parameters can be updated during process online optimisation for scenarios such as a sudden disturbance of the PBR operation (e.g., random failure event of the mixing pumps in the PBR [202]).

With regards to the transport phenomena associated parameters listed in Table 4.2, η was observed to be higher than that reported in the literature [52]. This suggests a better light utilisation efficiency in the upscaled PBR due to an enhanced transport phenomena (i.e., better culture mixing that promotes a more frequent light/dark cycling). This is the case as unlike the small scale PBR with magnetic stirrer driven mixing, the upscaled PBR recirculated the biosuspension externally with a peristaltic pump from the overflow outlet into its bottom inlet via a connecting tube. In addition, the shorter light path length (36mm) of the upscaled PBR compared to that of the small scale PBR likely prevents cells from prolonged light deprivation as the enhanced culture mixing frequently cycled cells from the rear to the front PBR section. Shortened light/dark cycles are known for impacting the photosynthetic electron distribution in *R. palustris* via the cell redox and ATP balances [207]. As a result, the cells are subjected to metabolic pathway switches competing for the electrons with biomass and biohydrogen pathways being the two favoured electron sinks as their productivities were observed to be significantly enhanced. These observations are coherent with literature surrounding other photosynthetic bacteria as the authors Koku et al., [188] reported a respective 53% and 23% increase in biomass concentration and biohydrogen productivity with a 14h light-10h dark periods compared to continuous illumination for *Rhodobacter sphaeroides* O.U. 001.

Table 4.3: Calibration of transport phenomena associated parameters.

Parameters	**Value**	**Units**	**Literature**
η	4.515	dimensionless	0.25 to 3.625 [52]
ϕ	1.945	dimensionless	n/a

n/a: not available

It was found that, $\phi = 1.945$ as exhibited in Table 4.3, with this parameter being a novel contribution of this study and comparative literature on this parameter being unavailable. Nonetheless, it can be deduced that the maximum specific H_2 production rate was almost doubled due to a decrease in the partial pressure of PBR which facilitates biohydrogen

synthesis. This is in agreement with the authors [72] who reported a 12% increase in the biohydrogen productivity of *Rhodobacter sphaeroides* ZX-5 when the total pressure at the PBR's headspace was decreased from 1.082×10^5 to 0.944×10^5 Pa. However, their observations were void of a mechanistic description or any kinetic model parameters needed to capture the essential bio-physical knowledge. This gap has been bridged herein and presents an important advance in the aid of efficient design and upscaling of novel PBR configurations such as that in Cho and Pott [44].

Finally, since the kinetic model for *Rhodopseudomonas palustris* biohydrogen production within different PBR configurations has been constructed and verified, the first future research phase will focus on the investigation of kinetic model-based process optimisation and PBR design for the maximisation of biohydrogen production. Also, as the simulation performance of the kinetic model can be improved by introducing an adequate level of parameter uncertainty, perturbation analysis will be exploited in the second phase of future work for robust optimisation of the dynamic bioprocess.

4.4 Conclusion

In this research, a detailed mechanistic model capable of simulating the photoheterotrophic biomass growth and biohydrogen production of the photosynthetic bacterium *R. palustris* under the influences of light intensity, light attenuation and temperature was proposed. By using experimental data from a small scale (0.5 L) photobioreactor (PBR) with magnetic stirrer driven mixing, the intrinsic kinetic parameters were identified via an efficient parameter estimation method. The high accuracy of the model and its estimated parameters were verified by comparing with experimental measurements and previous literature. Based on perturbation analysis, it is seen that although the temperature and light dependent parameters are both sensitive to the model output, the former should first be identified and validated with more experimental data prior to the use of the model whilst the latter is more suited to be re-estimated during an online model based process optimisation framework.

For upscaling applications, two transport phenomena dependent parameters η and ϕ were proposed and embedded into the mechanistic model, thus requiring re-calibration for across-scale extrapolations. By comparing the model simulation result with experimental measurements from a larger scale (1 L) PBR with peristaltic pump driven mixing, the accuracy and applicability of the kinetic model for large scale PBR simulation was verified. It is also concluded that given the better culture mixing and gas removal performance in the large scale PBR, the biohydrogen production rate is enhanced markedly compared to the small scale PBR. This provides important advances for the future efficient design of novel

PBRs as well as upscaling to different production scales while enabling process online optimisation for the maximisation of biohydrogen production.

Acknowledgment

The author Mr. B. Anye Cho is fully funded by the Commonwealth Scholarship Commission, United Kingdom. We would like to thank Prof. Robert Pott at Stellenbosch University, South Africa for providing the experimental datasets.

Appendix B: Derivation of biohydrogen model under the influence of light and temperature

Using Eq. (4.3a), Y_{XH_2} and Y_{H_2} are formulated to be both light intensity and temperature-dependent thereby leading to (B1)

$$\frac{dH_2}{dt} = Y_{XH_2}(I,T) \cdot \frac{dX}{dt} + Y_{H_2}(I,T) \cdot X \tag{B1}$$

As $\frac{dX}{dt} = \mu(I,T) \cdot X$ in (B1) leading (B2)

$$\frac{dH_2}{dt} = Y_{XH_2}(I,T) \cdot \mu(I,T) \cdot X + Y_{H_2}(I,T) \cdot X \tag{B2}$$

The multiplicative effect of light intensity and temperature of the two variables (i.e., $Y_{XH_2}(I,T) \cdot \mu(I,T)$ produces a new variable (i.e., $\mu Y_{XH_2}(I,T)$) leading (B3)

$$\frac{dH_2}{dt} = \mu Y_{XH_2}(I,T) \cdot X + Y_{H_2}(I,T) \cdot X = \left[\mu Y_{XH_2}(I,T) + Y_{H_2}(I,T)\right] \cdot X \tag{B3}$$

By letting $\alpha_{H_2}(I,T) = \mu Y_{XH_2}(I,T) + Y_{H_2}(I,T)$, the combined effect of the variables is captured by a single variable which is both light intensity and temperature-dependent.

$$\frac{dH_2}{dt} = \alpha_{H_2}(I,T) \cdot X = \alpha_{max} \cdot \alpha_{H_2}(T) \cdot \alpha_{H_2}(I) \cdot X \tag{B4}$$

Finally, (B5) in the explicit form of (B4) used within this study

$$\frac{dH_2}{dt} = A'_{H_2} \cdot \exp\left(-\frac{E_{a,H_2}}{RT}\right) \cdot \left(\frac{\frac{I_0}{(\tau \cdot X) \cdot L} \cdot (1 - e^{-(\tau \cdot X) \cdot L})}{k_{s,H_2} + \left(\frac{I_0}{(\tau \cdot X) \cdot L} \cdot (1 - e^{-(\tau \cdot X) \cdot L})\right)}\right) \cdot X \tag{B5}$$

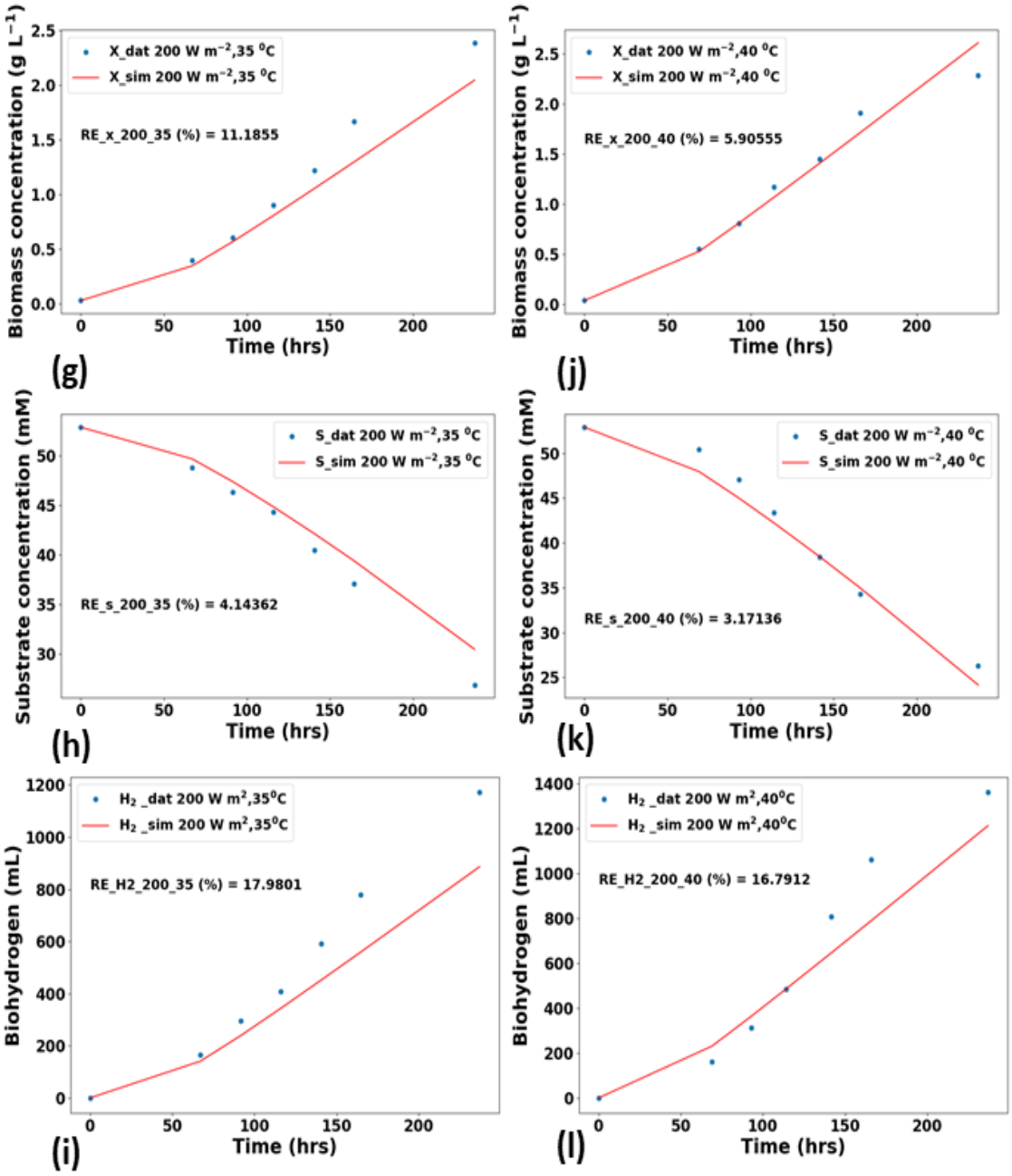

Figure B 4.8: Model fitting results for the various state variables at: 200 Wm^{-2} at 35℃ (g) to (i), and 200 Wm^{-2} at 40℃ (j) to (l). The (g) to (i) and (j) to (l) are state variables corresponding to the biomass, substrate and biohydrogen models respectively. Each fitting is accompanied by the percentage relative error (%RE).

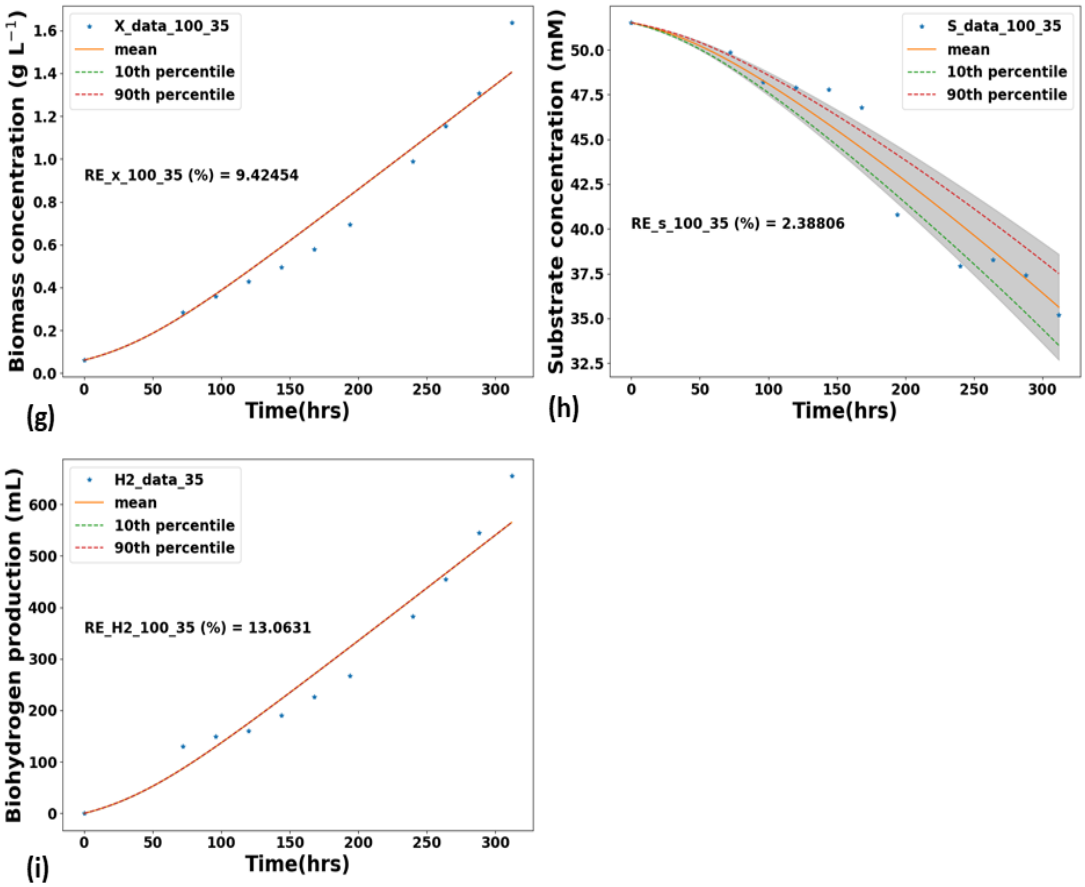

Figure B 4.9: Perturbation analysis for input uncertainties of 20% for Class I: (g) to (i) corresponding to biomass, substrate and biohydrogen models respectively. The mean, 10th and 90th percentile, and %RE for 100 Monte-Carlo simulations.

Chapter 5

A CFD Coupled Photo-bioreactive Transport Modelling of Tubular Photobioreactors Mixed by Peristaltic Pump

5.1 Preface

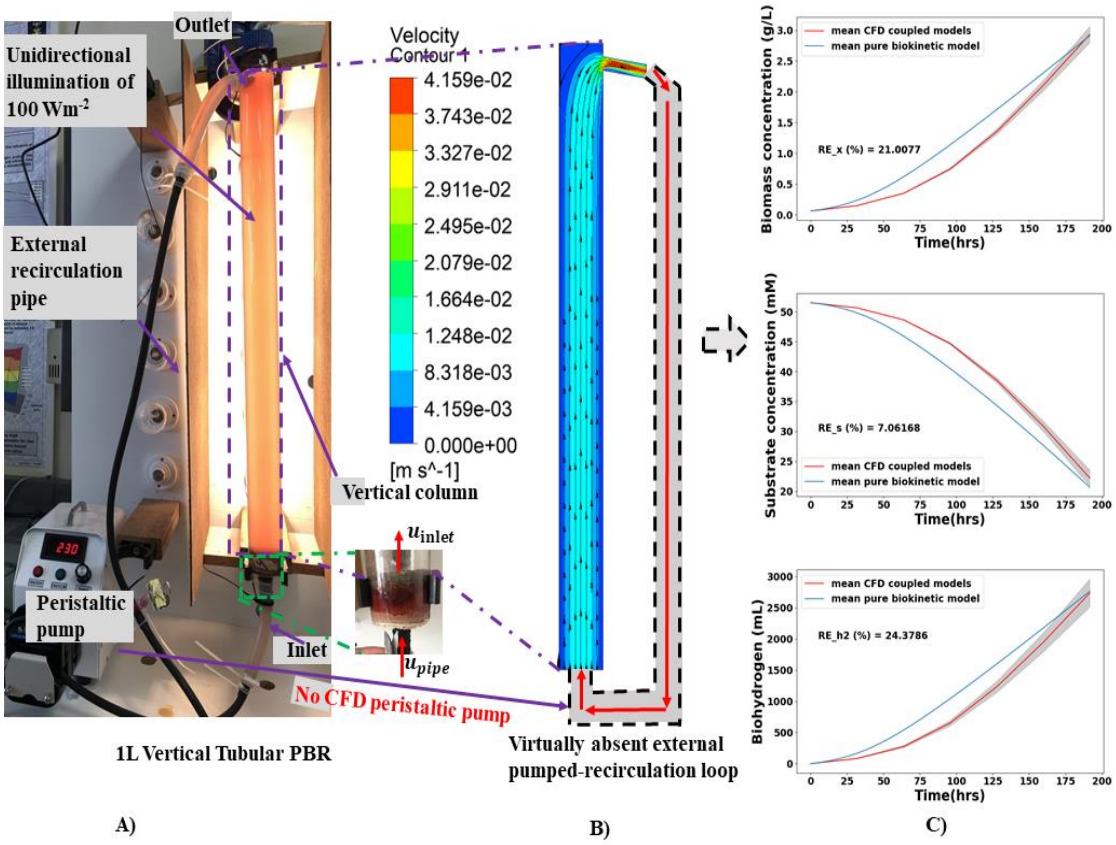

Figure 5.1: Graphical abstract showing: A) photobioreactor setup, B) CFD velocity results within the main column and illustrated virtually absent section, C) CFD trajectories of biomass, substrate and biohydrogen under 5% input uncertainty.

The airless and low shear mixing of externally pumped-recirculated vertical tubular photobioreactors (VT-PBRs) proffers biohydrogen production with higher purity (e.g., 94.1±0.4% by Ross and Pott [149]), therefore an attractive biotechnology for upscaling. To realise this, robust photo-bioreactive transport models are required to identify the primary limiting factors affecting biohydrogen optimisation and the VT-PBR's upscaling. On one hand, the proposed modelling strategy in Chapter 3 could be directly applied herein, especially as Chapter 4 has already presented and validated the photo-biokinetic model of *R. palustris* within the VT-PBR but outside of a CFD solver, thus only pending hydrodynamic

coupling herein. On the other hand, the CFD modelling of the complex interactions between hydrodynamics, light transport and bioreactions within the three VT-PBR's distinctive sections: i) vertical column, ii) dark external recirculation pipe, and iii) peristaltic pump as illustrated in Figure 5.1 A), has proven computationally intractable.

Therefore, Chapter 5 focuses on the development and validation of a new cost-efficient photo-bioreactive transport modelling strategy for tubular photobioreactor mixed by peristaltic pump by: approximating the complexities of the peristaltic pump with inlet-outlet boundary conditions (BCs), (ii) introducing mean residence time (t_m) for updating the BCs during simulation, and (iii) unifying t_m-dependent accelerated growth kinetics to parallelised Computational Fluid Dynamic (CFD) environment. Due to superior cost-savings compared to previous CFD studies, Monte-Carlo simulations for 5% coupled CFD-photo-bioreaction parameter uncertainties was investigated for the bioprocess reliability; this has not been done before.

The complete details of the paper as presented in Chapter 5 is structured as follows: Section 5.1 introduces the study; Section 5.2 presents the CFD hydrodynamic models and techniques for experimental validations, and the strategies for coupling the hydrodynamic, light transport and biokinetic models; Section 5.3 then presents the results and discusses the hydrodynamic insights and PBR performance under uncertainty; finally, Section 4 concludes the current study.

5.2 Publication 3

Bovinille Anye Cho[1], Elze Grobler[2], Robert William McClelland Pott[2], Ehecatl Antonio del Río Chanona[3], Dongda Zhang[1]. A CFD coupled photo-bioreactive transport modelling of tubular photobioreactor mixed by peristaltic pump. Accepted by Chemical Engineering Science, currently in press.

1. Department of Chemical Engineering and Analytical Science, University of Manchester, the Mill, Sackville Street, Manchester, M1 3AL, UK.
2. Department of Process Engineering, University of Stellenbosch, Banghoek road, Stellenbosch, 7599, South Africa.
3. Department of Chemical Engineering, Imperial College London, South Kensington Campus, London SW7 2AZ, UK.

Bovinille Anye Cho's contributions included construction of the new photo-bioreactive transport model, dynamic model parameter estimation, analysing of the data and results, drafting of the manuscript and manuscript revision for important intellectual content. Elze Grobler and Robert William McClelland Pott performed the tracer dye studies used for model validations. Ehecatl Antonio del Río Chanona provided valuable insights into the project. Dongda Zhang critically revised the manuscript for important intellectual content and gave the final approval of the article.

Abstract

Optimisation and upscaling of biohydrogen production in externally pumped-recirculated photobioreactors (PBRs) are hampered by computational infeasibilities of coupling hydrodynamics, to light transmission and bioreaction transport, through the column and peristaltic pump. This study approximates the complexities of peristaltic pump with inlet-outlet boundary conditions (BCs), introduces mean residence time (t_m) for updating BCs during simulation, and unifies t_m-dependent accelerated growth kinetics to parallelised Computational Fluid Dynamic (CFD) environment. Due to superior cost-savings compared to previous CFD studies, the bioprocess reliability under 5% coupled CFD-photo-bioreaction parameter uncertainties was investigated for the first time, and thoroughly validated with tracer dye studies plus literature bioreaction data for a 1L PBR. The results agreed to within 10% of error for simulated velocities, identifying undesired regions with poor radial mixing, and showed similar output uncertainties between the coupled CFD-photo-bioreactions and pure photo-bioreactions models, indicating absence of numerical diffusion. Therefore, this approach has great potentials for modelling other similar biosystems.

Keywords: CFD modelling; tubular photobioreactor; biokinetic modelling; biohydrogen production; uncertainty analysis.

5.1 Introduction

Microbial cultivation in photobioreactors (PBRs) for high-value bio-based products, fuels, and materials presents a viable option for tackling the ever-increasing mass and energy demands of the world's rapid population growth rate. Hence, these biotechnologies are receiving increasing interest from academia and the biorefinery, pharmaceutical, cosmetic and aquacultural industries [65,208]. Computational Fluid Dynamics (CFD) is a powerful numerical tool for accelerating the development and optimisation of novel biotechnologies, reducing the labour and expenses required for the physical design [51,65]. Experimentally validated CFD simulations have been extensively applied in PBR design, upscaling and structural optimisation of different configurations including: closed-PBRs: (i) continuous stirred tank PBRs [48–50], (ii) torus PBRs [53], (iii) flat-plate PBRs [14,51,52], (iv) airlift driven tubular PBRs [54,55], (v) bubble column tubular PBRs [56–59], (vi) thermosiphon PBRs [44], (vii) annular PBRs [60], (viii) semi-partitioning PBRs [61], and (ix) taylor-couette PBRs [27,28,62], to name a few.

Among the closed-PBR configurations, airlift and bubble column driven tubular PBRs are the commonly preferred configurations due to their (i) high surface-area-to-volume ratio, (ii) flexible tube arrangement enabling different patterns and orientation to maximise the photosynthetic efficiency, (iii) low energy consumption, and (iv) efficient mixing with low shear rate [208,209]. However, as an air-liquid-solid multiphase system, they are not attractive for producing gaseous biofuels such as biohydrogen due to the added expenses of separating the gaseous biofuel from the air mixture during downstream processing [66,71]. As a result, several modifications have been proposed in the literature [71,120,149], including the addition of (i) an external recirculation loop, (ii) a biohydrogen collection unit, and (iii) a peristaltic pump to provide airless pumped-recirculation mixing for a biohydrogen gas-liquid-solid tri-phasic system labelled herein as an externally pumped-recirculated tubular PBR.

Although the externally pumped-recirculated tubular PBR is an attractive biotechnology to be upscaled due to its higher biohydrogen productivity and percentage purity (e.g., $94.1 \pm 0.4\%$ in [149]), CFD modelling of the configuration is limited to only a few studies in literature. For instance, the authors El Maakoul et al., [210] replaced the external recirculation loop within their CFD model with a mass flowrate inlet and outlet boundary conditions to approximate the pumped-recirculation action for a 90 L anaerobic digester used for biogas production. They then investigated the effects of increasing recirculation rate on heat delivery and pressure drop. Similarly, Saini et al., [211] numerically investigated the

optimum recirculation rate for complete mixing of the anaerobic digester at a reduced power consumption cost. On the other hand, the authors Rivas et al., [212] used a velocity inlet and pressure outlet for the recirculation boundary conditions to investigate the spatial and temporal distribution of scalar tracers (i.e., mole fraction of methylene blue, but could be the concentration of any arbitrary specie for other investigations) in a (i) water and methylene blue, and (ii) water, methylene blue and artificial biomass mixtures within a 2.02 L Plexiglas tubular PBR. To guarantee recirculation of the scalar, the scalar value at the outlet section was calculated and then used to update the inlet scalar value every 10 mins for the duration of a 200 min CFD simulation.

Despite attaining satisfactory results, these studies were mainly focused on the fluid flow and mixing visualisation, while microbial growth, substrate consumption and biogas production were omitted from their CFD models. Hence, more robust CFD models are needed to capture the interacting effects of both the biotic and abiotic factors within such complex PBR biosystems. Specific to the scalar inlet updating time interval of 10 mins in Rivas et al., [212], the reasons for choosing this time changes to adequately represent the recirculation process of any arbitrary PBR were not provided thus, it is still unclear how to choose an updating time for an externally pumped-recirculated tubular PBRs of different scales and configurations. On the other hand, mean residence time has often been exploited in the CFD modelling of photocatalytic reactors [213,214] and chemical reactors [215,216] to analyse the degree of contaminant reduction and microbial inactivation. Therefore, studies which utilises the mean residence time for informing the frequency at which the scalar inlet boundary condition is to be updated, remains to be elucidated in the CFD modelling of replaced external recirculation loop with inlet-outlet boundary conditions.

Our previous work demonstrated that accelerating the simulated growth kinetics [52] is an efficient strategy for coupling the hydrodynamics and scalar transport phenomena, reducing the CFD computational clock time from a few days to a few hours without adversely affecting simulation accuracy. Meanwhile, parallel computing also reduces the computational cost immensely; for instance, Nauha and Alopaeus [148] parallelised their CFD simulation over 6 processors, reducing the computational clock time needed for simulating a 60 L bubble column from a few months to a few days. Therefore, merging both approaches present a unique opportunity to address the computational burden of coupling expensive CFD simulations with multiple state variables dynamics. In particular, estimation of prediction uncertainties from the biokinetic model parameters coupled to the CFD hydrodynamic model is of utmost interest but was previously unexplored due to the prohibitively high computational cost of Monte Carlo analysis.

Therefore, this manuscript aims at (i) to develop a CFD coupled hydrodynamics, light transport and biokinetic model for an externally pumped-recirculated tubular PBR, (ii) to validate the model against a literature case study [2] for biomass growth, glycerol consumption and biohydrogen production by the photosynthetic bacterium *Rhodopseudomonas palustris* NCIMB 11774, and (iii) for the first time, combine the computational cost-savings achieved by accelerated simulated growth kinetics and parallel computing to investigate the reliability of the CFD coupled hydrodynamic-biokinetic model via uncertainty propagation with Monte Carlo analysis.

5.2 Methodology

5.2.1 Experimental setup and tracer dye studies

The operational mode of the VT-PBR has been detailed in our previous works [2,149]; thus, only the adaptation of the experimental setup for tracer dye studies was presented herein. For this, ten monitoring points, labelled P_{1-10}, each 0.05 m apart were marked on the vertical column, as shown in Figure 5.2 A). Upon reaching hydrodynamic steady-state, achieved by recirculating phenolphthalein indicator in distilled water through the VT-PBR for at least one minute, 3 mL of 3.5 M NaOH was injected into the flow field via a sampling port in the external recirculation pipe producing a pink coloration. As the pink tracer was carried upward from P_1 to P_{10}, the time taken for the pink colouration to pass each monitoring point was recorded. By dividing the distance between the monitoring points by the time taken to pass each point, the local velocity of the flow field was determined. This procedure was repeated in triplicate, and the data collected was later used for validation of the CFD model's prediction at the locations of the numerical monitoring points.

5.2.2 Computational fluid dynamics (CFD)

5.2.2.1 Hydrodynamic model and CFD domain

As illustrated in Figure 5.2 A), the VT-PBR was characterised by three main sections: i) a vertical column illuminated by 100 W m^{-2} bulbs, ii) a dark (i.e., non-illuminated) external recirculation pipe, and iii) a peristaltic pump for the pumped-recirculation mixing. While each section is important, a CFD model that included them all would be too computationally expensive to simulate. Hence, the VT-PBR CFD model made the following simplifying assumptions:

- Only the illuminated vertical column and outlet section were included in the CFD model, while the dark recirculation pipe and peristaltic pump were omitted as they were considered photosynthetic dead zones without light.

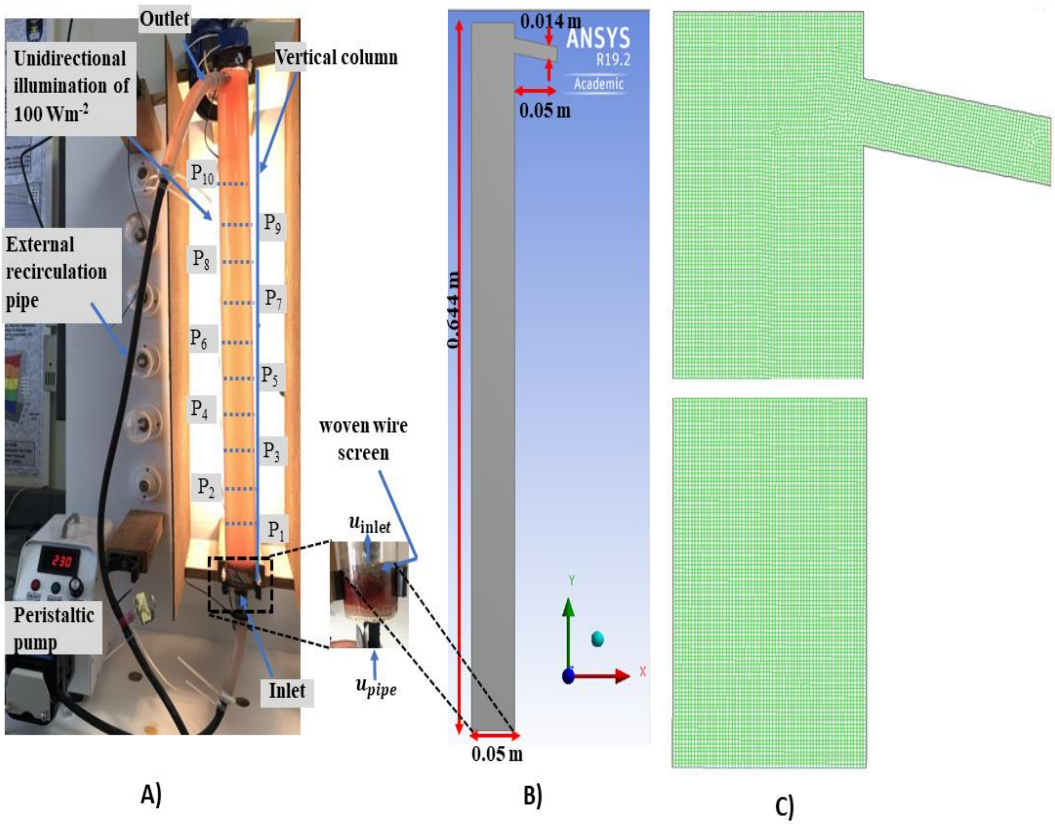

Figure 5.2: Experimental and CFD step up: A) Vertical tubular photobioreactor (VT-PBR) whereby $P_{1\text{-}10}$ are local velocity measuring points for the tracer dye study, B) 2D VT-PBR geometry with dimensions, and C) Quadrilateral dominant gird elements used in the domain meshing.

- The 3D geometry of the remaining illuminated column was approximated with the 2D design shown in Figure 5.2 B) due to the symmetrical tubular nature of the VT-PBR.
- Flow velocity via the inlet and outlet sections of the 2D geometry were captured with suitable boundary conditions, as reported in Table 5.1. Therefore, the peristaltic pump was omitted from the CFD model like in other literature sources [210–212].
- The smaller pipe's inlet velocity (i.e., $\boldsymbol{u}_{pipe}$) was uniformly distributed by the woven wire screen into the VT-PBR's inlet velocity (i.e., $\boldsymbol{u}_{inlet}$) but simulating its smaller grid element sizes would significantly increase the number of elements count and thus computational cost. Therefore, mass balance was applied to estimate $\boldsymbol{u}_{inlet}$ with Eq. (5.1a) whereby A_{pipe} and A_{VT-PBR} are the cross-sectional areas of the smaller pipe and the VT-PBR respectively.

$$\boldsymbol{u}_{inlet} = \frac{A_{pipe} \cdot \boldsymbol{u}_{pipe}}{A_{VT-PBR}} \tag{5.1a}$$

- The Reynolds number was calculated to be 381.9, indicating a laminar flow regime within the vertical column, thus Eq. (5.1b) for fully developed laminar flow profile was implemented as the inlet boundary condition of the CFD's hydrodynamic model.

$$\boldsymbol{u}(r) = 2 \cdot \boldsymbol{u}_{inlet} \cdot \left[1 - \left(\frac{r}{R}\right)^2\right] \tag{5.1b}$$

  whereby $\boldsymbol{u}(r)$ is the radial velocity, $2 \cdot \boldsymbol{u}_{inlet}$ is the maximum velocity occurring at the centre when the radius $r = 0$, R is the inner radius of the VT-PBR.
- The absence of visible biohydrogen bubbles during the operation of the experimental setup and the assumption of density similarities between cell biomass and water [52,215] reduces the investigation into a single-phase flow problem.
- Fluid within the entire CFD domain was incompressible, Newtonian, and operating under isothermal conditions at 301.15 K; thus, heat exchange was not considered.

Table 5.1: Operating conditions of the VT-PBR.

General boundary conditions	**Hydrodynamic model**	**Mass (scalar) transport model**
Inlet conditions	Velocity inlet (m s^{-1}) $\boldsymbol{u}_{inlet} = 0.0055$	Dirichlet (updated after every mean residence time)
Outlet conditions	Pressure outlet	Neuman (i.e., zero flux)
Top wall condition (water surface)	Free surface of constant shear (free slip) at 1 atm	Neuman (i.e., zero flux)
All other wall conditions	Non-slip	Neuman (i.e., zero flux)

Based on these assumptions, the continuity (i.e., Eq. (5.2)) and momentum (i.e., Eq. (5.3)) equations were solved as the CFD hydrodynamic model.

$$\frac{\partial \rho}{\partial t} = \nabla \cdot (\rho \mathbf{u}) = 0 \tag{5.2}$$

$$\frac{\partial}{\partial t}(\rho \mathbf{u}) + \nabla \cdot (\rho \mathbf{u}\mathbf{u}) = -\nabla P + \nabla \cdot \left(\mu \left[(\nabla \mathbf{u} + \nabla \mathbf{u}^T) - \frac{2}{3}\nabla \cdot \mathbf{u} I\right]\right) + \rho \mathbf{g} + \mathbf{F} \tag{5.3}$$

where $\boldsymbol{u}$ is the velocity, ρ is the density, while $\rho\boldsymbol{g}$ and $\boldsymbol{F}$ are the gravitational body force and external body forces, respectively, P is the static pressure, μ is the molecular viscosity, and I is the unit tensor.

5.2.2.2 Biokinetic model

Our recent work proposed a biokinetic model for simulating biomass growth, substrate consumption and biohydrogen production by the photosynthetic bacterium *R. palustris* within the VT-PBR [2], reproduced in Eq. (5.4) to Eq. (5.6). However, to approximate the biokinetics of the VT-PBR based solely on the productivity of the vertical column, it was necessary to correct for the fraction of time, T_L the bacteria cells spent within the illuminated zone of the experimental VT-PBR, as defined by Eq. (5.7). A caveat herein is that photosynthetic biomass growth was not limited by substrate concentration as it was supplied in replete amounts, hence the maintenance term in Eq. (5.5) was not influenced by T_L .

$$\frac{dX}{dt} = T_L \cdot A' \cdot \exp\left(-\frac{E_a}{RT}\right) \cdot \left(\frac{\frac{I_0}{(\tau \cdot X) \cdot L} \cdot (1 - e^{-(\tau \cdot X) \cdot l})}{k_s \left(\frac{1}{\eta}\right) + \left(\frac{I_0}{(\tau \cdot X) \cdot L} \cdot (1 - e^{-(\tau \cdot X) \cdot l})\right)} \right) \cdot X \tag{5.4}$$

$$\frac{dS}{dt} = -Y_{XS} \cdot \left(T_L \cdot A' \cdot \exp\left(-\frac{E_a}{RT}\right) \cdot \left(\frac{\frac{I_0}{(\tau . X) \cdot L} \cdot (1 - e^{-(\tau \cdot X) \cdot l})}{k_s \left(\frac{1}{\eta}\right) + \left(\frac{I_0}{(\tau \cdot X) \cdot L} \cdot (1 - e^{-(\tau \cdot X) \cdot l})\right)} \right) \cdot X \right) - m \cdot X \tag{5.5}$$

$$\frac{dH_2}{dt} = T_L \cdot \phi \cdot A'_{H_2} \cdot \exp\left(-\frac{E_{a,H_2}}{RT}\right) \cdot \left(\frac{\frac{I_0}{(\tau \cdot X) \cdot L} \cdot (1 - e^{-(\tau \cdot X) \cdot l})}{k_{s,H_2} \left(\frac{1}{\eta}\right) + \left(\frac{I_0}{(\tau \cdot X) \cdot L} \cdot (1 - e^{-(\tau \cdot X) \cdot l})\right)} \right) \cdot X \tag{5.6}$$

$$T_L = \frac{t_L}{t_L + t_D} \tag{5.7}$$

whereby A' (8.30×10^3 h^{-1}) and A'_{H_2}(1.01×10^{10} h^{-1}) are the pre-exponential factors for biomass growth and biohydrogen production, E_a (2.74×10^4 J mol^{-1}) and E_{a,H_2} (4.78×10^4 J mol^{-1}) are the activation energies for biomass growth and biohydrogen production, R (8.3145 J $mol^{-1}K^{-1}$) is the universal gas constant, T (301.15 K) is the absolute temperature, I_0 (100 Wm^{-2}) is the incident light intensity, k_s (500.0 Wm^{-2}) and k_{s,H_2} (500.0 Wm^{-2}) are the light saturation coefficients for biomass growth and biohydrogen production, τ (90.8 m^2 g^{-1}) is the light absorption coefficient, L (0.05 m) is the light path length, Y_{XS} (9.66 mmol g^{-1}) and m (0.0140 mmol g^{-1}) are the substrate yield coefficient and maintenance coefficient, η (4.515) is the effective light coefficient and ϕ (1.945), is the biohydrogen enhancement factor. Finally, t_L (s) and t_D (s) are the lengths of time spent in the light and dark zones, respectively, as estimated from the CFD model using Eq. (5.8) based on the predicted flow

rates $\dot{V}_i$ through the illuminated vertical column (i.e., $i = L$) of volume V_L and dark recirculation pipe (i.e., $i = D$) of volume V_D.

$$t_i = \frac{V_i}{\dot{V}_i} \tag{5.8}$$

5.2.2.3 Coupling of CFD hydrodynamics and biokinetic models

To integrate the dynamics of the biokinetics and concentration distribution within the VT-PBR, the three mass (scalar) transport equations describing the bioreaction species corresponding to the biomass growth (i.e., Eq. (5.9)), substrate consumption (i.e., Eq. (5.10)) and biohydrogen production (Eq. (5.11)) were coupled with the converged velocity flow fields from solving Eq. (5.2) and Eq. (5.3). On the left-hand side of Eq. (5.9) to (5.11), the first and second terms denote the accumulation and convection of the bioreaction specie, respectively. On the right-hand side of Eq. (5.9) to (5.11), the first and second terms denote bioreaction specie diffusion and growth, respectively, where the diffusivities were taken from literature: D_{e_X} = (5.5×10^{-10} m^2 s^{-1}) [52], D_{e_S} = (1.06×10^{-9} m^2 s^{-1}) [217] and $D_{e\_H_2}$ = (5.11×10^{-9} m^2 s^{-1}) [217]. The CFD implementation of the light transport model (i.e., $I_0 \cdot \exp^{(-\tau \cdot X \cdot l)}$) within the specie growth terms has already been detailed in our previous work [52] but was modified as illustrated in Table 5.2 to eliminate interpolation errors between the scalar's currently occupied mesh cell elements and the unoccupied neighboring cell elements of the domain. This guarantees the strong coupling of the column's rising plume to photobioreactions by tracking the rising plume's vertical distance and activating the light transport model in a compartmentalised approach. Since no significant improvement in the simulation results were observed beyond 50 compartments (i.e., 0.0128775 m each), thus 50 was deem satisfactory to avoid higher computational costs.

$$\frac{dX}{dt} + [\nabla \cdot (\boldsymbol{u}X)] = \nabla \cdot \left(D_{e\_X} \nabla \mathrm{X}\right) + \left[A' \cdot \exp^{\left(-\frac{E_a}{R \cdot T}\right)} \cdot \frac{I_0 \cdot \exp^{(-\tau \cdot X \cdot l)}}{I_0 \cdot \exp^{(-\tau \cdot X \cdot l)} + k_s'} \cdot X\right] \tag{5.9}$$

$$\begin{aligned} \frac{dS}{dt} + [\nabla \cdot (\boldsymbol{u}S)] & \\ &= \nabla \cdot \left(D_{e\_S} \nabla \mathrm{S}\right) \\ &+ \left[-Y_{XS} \cdot A' \cdot \exp^{\left(-\frac{E_a}{R \cdot T}\right)} \cdot \frac{I_0 \cdot \exp^{(-\tau \cdot X \cdot l)}}{I_0 \cdot \exp^{(-\tau \cdot X \cdot l)} + k_s'} \cdot X - m \cdot X\right] \end{aligned} \tag{5.10}$$

$$\frac{dH_2}{dt} + [\nabla \cdot (\boldsymbol{u} H_2)] = \nabla \cdot \left(D_{e\_H_2} \nabla H_2\right) + \left[\phi' \cdot A'_{H_2} \cdot \exp^{\left(-\frac{E_{a,H_2}}{R \cdot T}\right)} \cdot \frac{I_0 \cdot \exp^{(-\tau \cdot X \cdot l)}}{I_0 \cdot \exp^{(-\tau \cdot X \cdot l)} + k'_{s,H_2}} \cdot X\right] \quad (5.11)$$

Table 5.2: Algorithm pseudocode for coupling light intensity and light attenuation to scalar transport.

Algorithm: Coupling light intensity and light attenuation to scalar transport	
1:	$u_{peak} \leftarrow$ rising plume's maximum velocity
2:	$t_{CFD} \leftarrow$ CFD simulation time
3:	$Y_T \leftarrow$ vertical column's height
4:	$Y \leftarrow$ rising plume's vertical distance
5:	$Y_C \leftarrow$ vertical coordinates of each mesh cell centroid
6:	$I(l) \leftarrow$ light intensity and light attenuation
7:	$C_i \leftarrow$ compartmentalisation of domain into 50. $\sum_{i=1}^{n=50} \left[(i-1) \cdot \frac{Y_T}{50} \ll C_i \ll \left(i \cdot \frac{Y_T}{50}\right)\right]$
8:	**for all** cells in discretise domain **do**
9:	**for all** compartments $C_{i=1\ to\ 50}$ in domain **do**
10:	$Y \leftarrow u_{peak} \cdot t_{CFD}$
11:	**if** $Y_C > Y$ **then**
12:	$I(l) = 0.0$
13:	**else**
14:	$I(l) = I_0 \cdot \exp^{(-\tau \cdot X \cdot l)}$ see [52]

In Eq. (5.9) to (5.11), the light saturation coefficients (i.e., k'_s and k'_{s,H_2}) and biohydrogen enhancement factor (ϕ') are intrinsic to the VT-PBR meanwhile the estimated k_s, k_{s,H_2} and ϕ in our previous work [2] were based on a smaller PBR (i.e., Schott bottle PBR). Therefore, the conversion from the referenced Schott bottle PBR into the VT-PBR's CFD model warranted the formulation of Eq. (5.12) and Eq. (5.13) to embed the consequential effects of light/dark cycles onto the VT-PBR's intrinsic light saturation coefficients. Notice that the parameters on the right-hand side of both Eq. (5.12) and Eq. (5.13) are known since the *effective light coefficient* of the referenced Schott bottle PBR, $\eta_{SB} = 1.0$. However,

parameters on the left-hand side are unknown but for any given one (e.g., k_s' or η_{VT}) whereby η_{VT} is the VT-PBR's intrinsic *effective light coefficient*, the other was straight forwardly identifiable as with Eq. (5.14). This implies that both k_s' and k_{s,H_2}' have to be firstly estimated for η_{VT} and η_{VT,H_2} to be identified. However, it is well known in the literatures [2,105] that these two intrinsic parameters have similar order of magnitudes (i.e., $k_s' \sim k_{s,H_2}'$), thus only k_s' was to be estimated herein together with ϕ' for the VT-PBR's intrinsic biohydrogen partial pressure influences. This was achieved by minimising the sum of squares errors between the data (i.e., Eq. (5.4) to Eq. (5.6)) and the CFD coupled hydrodynamic-biokinetic model (i.e., Eq. (5.9) to Eq. (5.11)) resulting to k_s', ϕ' and η_{VT} as 7.0 (W m^{-2}), 5.65 (dimensionless), 0.063 (dimensionless) respectively.

$$\left(\frac{k_s'}{\eta_{VT}}\right)_{VT-PBR} = \left(\frac{k_s}{\eta_{SB}}\right)_{SB-PBR} \cdot \frac{\eta_{SB}}{\eta} \tag{5.12}$$

$$\left(\frac{k_{s,H_2}'}{\eta_{VT,H_2}}\right)_{VT-PBR} = \left(\frac{k_{s,H_2}}{\eta_{SB}}\right)_{SB-PBR} \cdot \frac{\eta_{SB}}{\eta} \tag{5.13}$$

$$\eta_{VT} = \frac{k_s'}{\frac{499.99}{1.0} \cdot \frac{1.0}{4.51}} = \frac{k_s'}{110.74} \tag{5.14}$$

Whereby the subscript $SB - PBR$ represents the referenced Schott bottle PBR and η_{VT,H_2} is the *effective light coefficient* for biohydrogen production.

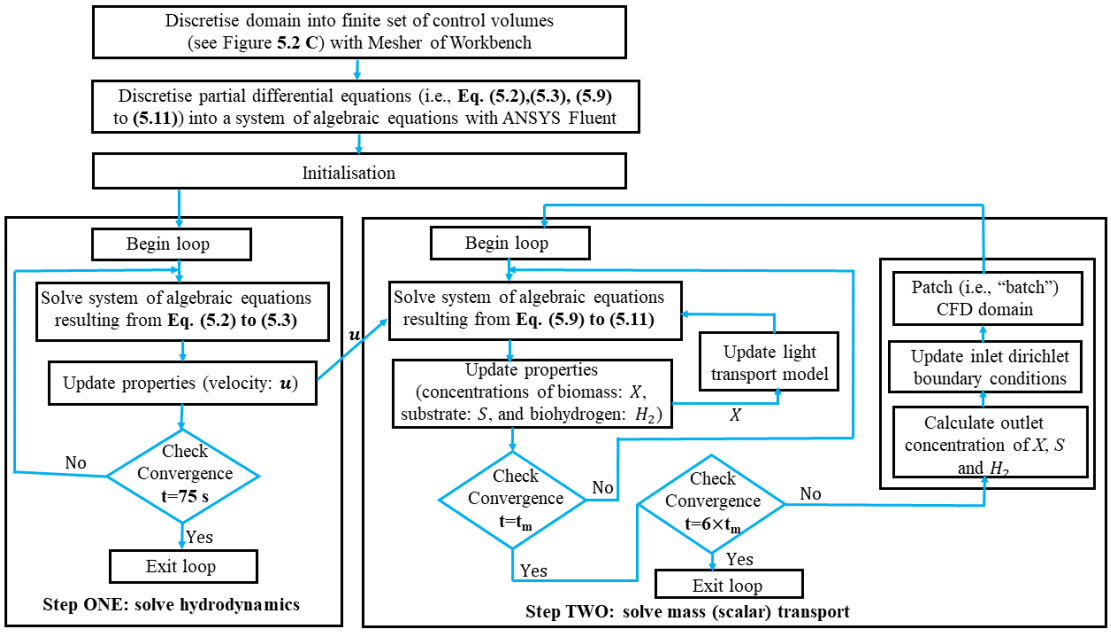

Figure 5.3: Schematic representation for the CFD coupling of hydrodynamics to light and biokinetics transport within an externally pumped-recirculated photobioreactor.

To model the external recirculation of X, S and H_2:(i) mean residence time was assumed equivalent to one pass through the vertical column and was determined from Eq. (C1) to Eq. (C3) in the Appendix C via the pulse input technique as discussed in [218], (ii) within each pass, the VT-PBR's inlet section was fixed to the value of the outlet's volume (i.e., area ×1 unit for a 2D CFD) average concentration from the previous pass, (iii) after each pass, the volume average concentration at the VT-PBR's outlet section was recalculated, and this result was patched into the VT-PBR's inlet section via the Dirichlet boundary condition and maintained for the duration of that pass as presented in Table 5.1. These three steps (i.e., (i), (ii), and (iii)) guarantees the complete recirculation of the bioreaction species from the VT-PBR's outlet back into the inlet section during the time course of the CFD simulation. As well, it renders the pass time accelerable for the growth kinetics decoupling it form the fluid dynamic's simulation time since it cannot be accelerated. The entire coupling strategy was summarised in Figure 5.3.

5.2.2.4 Solver settings and solution strategy

A time step size of 0.005 s and simulation time of 75 s was used to firstly solve the CFD hydrodynamic model to convergence (i.e., residuals drop below 10^{-6}). Secondly, 6 passes (i.e., $6 \times t_m$ s) were chosen to approximate the entire bioprocess and the same time step size of 0.005 s was considered for the mass (scalar) transport model. The computational cost-saving approach proposed by Anye Cho et al., [52] was implemented by scaling three model parameters: A', m and A'_{H_2} by a factor of $\frac{192\ \text{hrs}}{6 \times t_m\ \text{s}}$, accelerating biomass growth, substrate consumption and biohydrogen production, respectively. As per the parallel computing, the CFD simulations were parallelised over 16 processors with 4GB per processor core using the High-Performance Computing (HPC) cluster at The University of Manchester, United Kingdom.

5.2.2.5 CFD uncertainty propagation

The variability in the coupled hydrodynamic-biokinetic model predictions stems from the uncertainty associated with the estimated model parameters. While the impact of parameter uncertainty on a pure biokinetic model has been well quantified in literature [2,124,219,220] using Monte Carlo techniques, the impact of hydrodynamic coupling on the overall propagated uncertainty remains unknown. Therefore, to investigate this, a 5% input uncertainty was assigned to the transport phenomena related parameters in [2] corresponding to (i) $\frac{k_s}{\eta}$, $\frac{k_{s,H_2}}{\eta}$, τ and ϕ for the pure biokinetic model, and (ii) k'_s, k'_{s,H_2}, τ and ϕ' for the CFD coupled hydrodynamic-biokinetic model. This choice was motivated by the suitability of

these parameters for online model re-calibration during process optimisation. While the parameters collectively impact all three state variables, the state variables are also robust to mild perturbations of these parameters, as reported by Anye Cho et al., [2]. Latin Hypercube Sampling (LHS) drew 100 probabilistic samples from the parameter input spaces whereby each sample was used to simulate one possible process simulation using either the pure biokinetic model (i.e., Eq. (5.4) to (5.6)) or coupled hydrodynamic-biokinetic model (i.e., Eq. (5.9) to (5.11)). The former was simple to execute in Python version 3.7 using the *SMT* 1.0.0, *Numpy* and *SciPy* libraries, while the latter was more complex, requiring ANSYS Fluent version 19.2.

5.3 Results and discussion

5.3.1 Grid sensitivity analysis and CFD fluid flow validations

To compare and validate the CFD model's prediction against experimental results, the simulation was run with four different mesh resolutions (i.e., 50336, 104584, 205682, and 526257 grid elements), each composed of quadrilateral-based elements as shown in Figure 5.4 C). As seen in Figure 5.4 B), the CFD models predicted the local experimental velocity of all 10 measuring points to within a small percentage relative error (i.e., RE (%)) of less than 10% which is considered as satisfactory in other literature for PBR validation studies [44,55,221]. This confirms the reliability of the 2D CFD model for approximating the hydrodynamics of the 3D VT-PBR. Although increasing the number of grid elements from 50,336 to 526,257 did not improve the CFD's numerical accuracy, the computational time cost was observed to increase from 0.57 hrs to 0.68 hrs and 0.91 hrs, respectively. This result demonstrates that using the smallest number of grid elements (i.e., 50,336 grid elements) were sufficient for accurate CFD hydrodynamic prediction while minimising the computational time cost by 37.4 % compared with the highest 526,257 grid element option.

However, Figure 5.4 C) shows the grid Peclet number (P_e) to decreases with an increasing number of grid elements from 50,336 to 526,257, resulting in the highest and lowest P_e values of 10,884.2 and 3,359.5 respectively. This agrees with other literature findings [222,223] but high P_e values have serious consequences for numerical stability by inducing numerical (i.e., false) diffusion, which often masks the fluid's molecular diffusion, thereby inducing truncation errors into the advection-diffusion transport equations [222–224]. Therefore, given the stiff nature of the ordinary differential equations (ODEs) of the source growth terms embedded into the mass (scalar) transport equations, the CFD model with the highest number of grid elements (i.e., 526,257) and lowest P_e was selected for all subsequent analysis within this work.

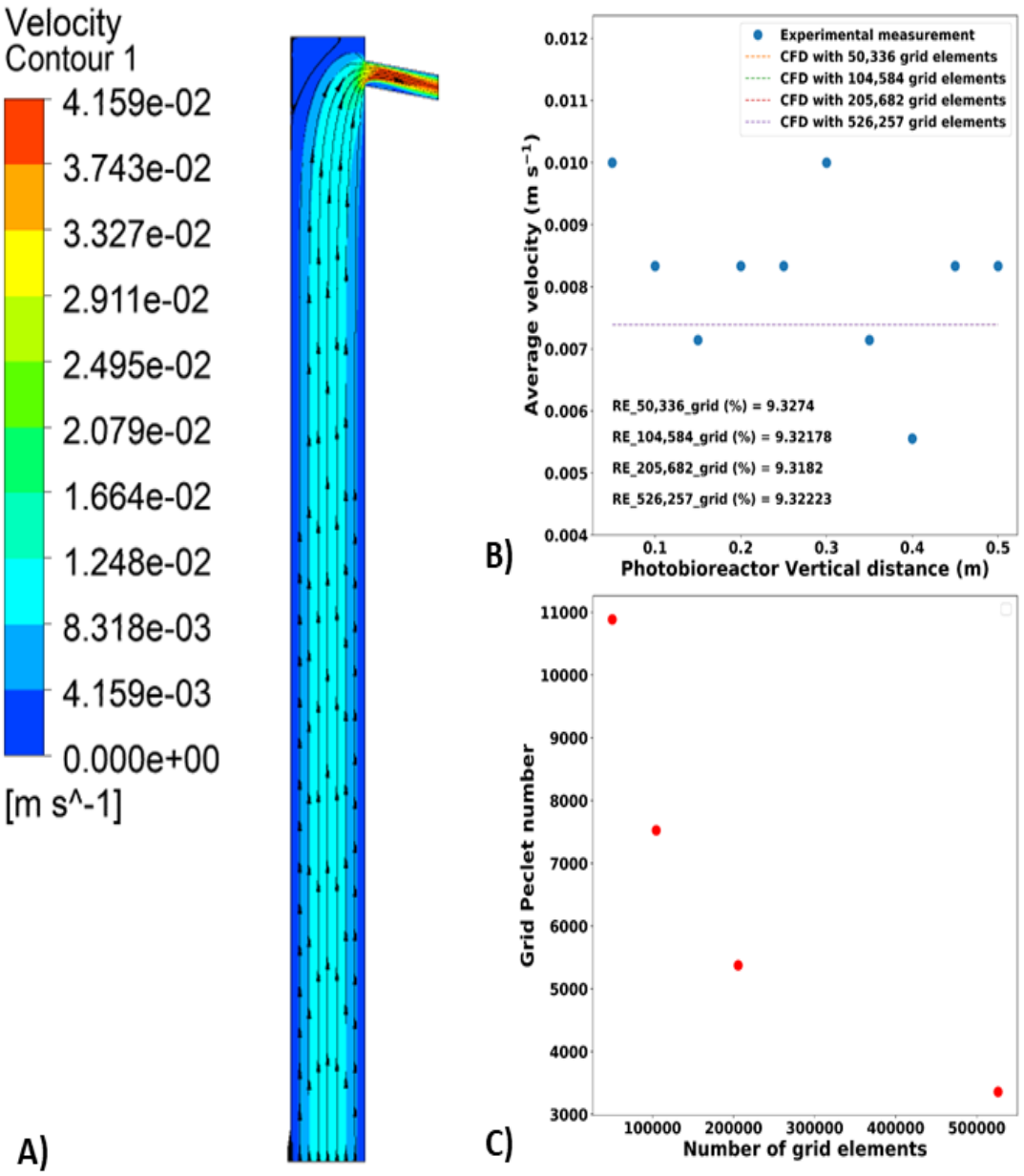

Figure 5.4: Results of A) CFD velocity contours with post-processed arrows indicting flow pattern and directions, B) CFD validation at monitoring points and grid sensitivity analysis with their indicated % RE, and C) influence of the number of CFD grid elements on the grid Peclet number.

5.3.2 CFD hydrodynamic insights

As the CFD model has been validated against experimental data, its full potential can be unleashed to explore the VT-PBR's hydrodynamic modes of operations, in particular: (i) the flow profile, and (ii) areas of poor mixing or hydrodynamic dead zones. Beginning with the flow profile, the CFD hydrodynamic model predicted an average velocity of 7.7×10^{-3} m s^{-1} with a corresponding light fraction time of 0.7 (T_L see Eq. (5.7) and Eq. (5.8)) and a parabolic flow profile exhibited by the arrowheads within the path lines across Figure 5.4

A) which are indicative of a laminar flow regime, thus validating the choice of the laminar flow regime during the CFD simulation solver setup as indeed correct. Now looking at hydrodynamic mixing within the VT-PBR, it can be seen that mixing was axially dominated, reflected by the vertically pointing arrowheads in Figure 5.4 A), which maintained a parallel trajectory from the inlet to the outlet. However, as visualised by the deep blue regions of the contour plot, hydrodynamic dead zones with lower velocities occurred near the walls and top of the vertical column. Low fluid velocities near the walls were expected, given the non-slip boundary condition at the walls of the vertical column in addition to the parabolic profile of the laminar flow which mainly peaks at the centre and then decreases towards the walls. Therefore, these results reveal the need to improve radial mixing within the VT-PBR to alleviate the stagnant near-wall regions to minimise prolonged exposure periods of either light intensity (i.e., photoinhibition) or darkness (i.e., photolimitation). Some have reported that static mixers can improve radial mixing; however, while many designs have been proposed for flat-plate PBRs [51,160,225,226], very few designs have been proposed for tubular PBRs [227–229].

5.3.3 Parameter estimation and CFD simulation results

To visualise the performance of the current photobioreactive transport modelling strategy, the CFD predicted light distribution and biomass concentration contours at four different simulation times within the 1st pass were plotted in Figure 5.5. It is seen that at the start (Figure 5.5 A)), the light distribution is zero through the domain and as the simulation progresses, the light distribution only becomes non-zero (Figure 5.5 B), C) and D)) for regions harboring the rising plume as indicated with the dash lines. Similar observations were made for the other coupled state variables (i.e., substrate consumption and biohydrogen production) and in the subsequent passes (i.e., 2nd to 6th) with the results not shown herein, thus validating the proposed algorithm. However, beneath the dash lines in Figure 5.5 B) to C) shows the algorithm to be missing out the curvature profile of the laminar plume, thereby activating the light transport model for a few more mesh cell elements which are unoccupied by the rising scalar, presenting an area of the algorithm's improvements.

Figure 5.6 A), C) and E) shows the model fitting and simulation results, where the percentage relative errors (i.e., RE (%)) for the biomass, substrate and biohydrogen models were 21.0 %, 7.1 % and 24.4 %, respectively. This high RE (%) were mostly observed for the intermediary passes (i.e., 2nd to 5th passes) and the good comparison at the 6th pass suggests decreasing RE (%) with increasing number of simulated passes. However, the improved performance achieved by increasing the number of passes comes at the cost of increased

computational CFD simulation time. Therefore, a good compromise between simulation accuracy and computational cost must be struck.

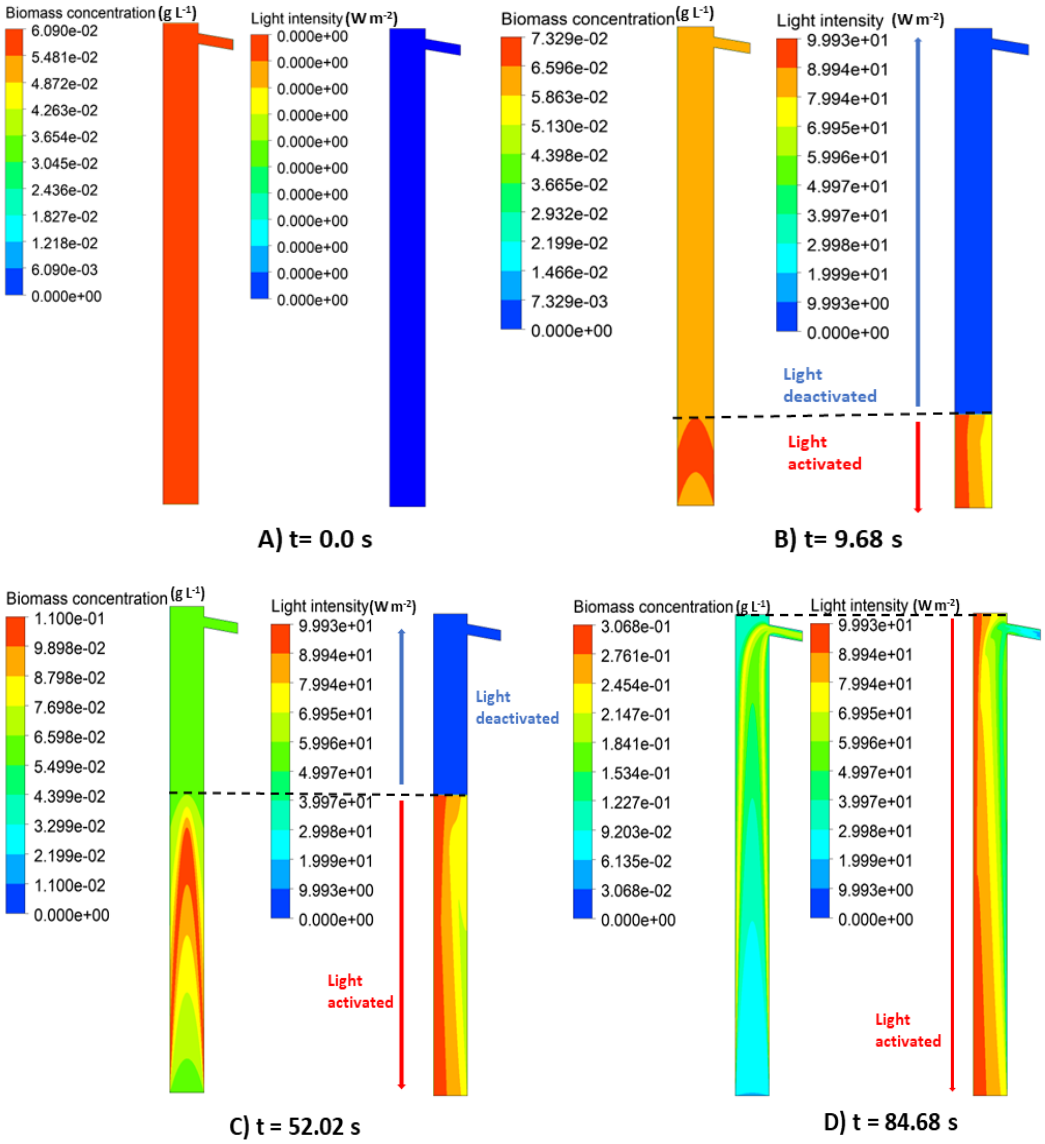

Figure 5.5: CFD prediction results of biomass and light intensity distribution at various time instances during the 1st pass: A) at the start, B) 9.68 s, C) 52.02 s, and D) end of pass. No photobioreactions outside of rising plume is indicated with blue arrows and the source term was always zero in the outlet pipe section.

The 6 passes herein only took 22.28 hrs of wall clock time to simulate 508.14 s of CFD simulation time. Of the 22.28 hrs wall clock time, it only took 0.91 hrs to simulate the hydrodynamics in Step ONE; the remaining 21.38 hrs were spent simulating the three state variables in Step TWO. Hence the model in this work is very efficient compared to others in the literature that took several days to converge even for a single state variable [142,148] using larger time step sizes of 3600 s [142] and 10 s [27]. Therefore, while increasing the number of passes would incur an additional computational cost, the resulting clock time

would remain competitive with published works, given the high accuracy achieved already with only 6 passes.

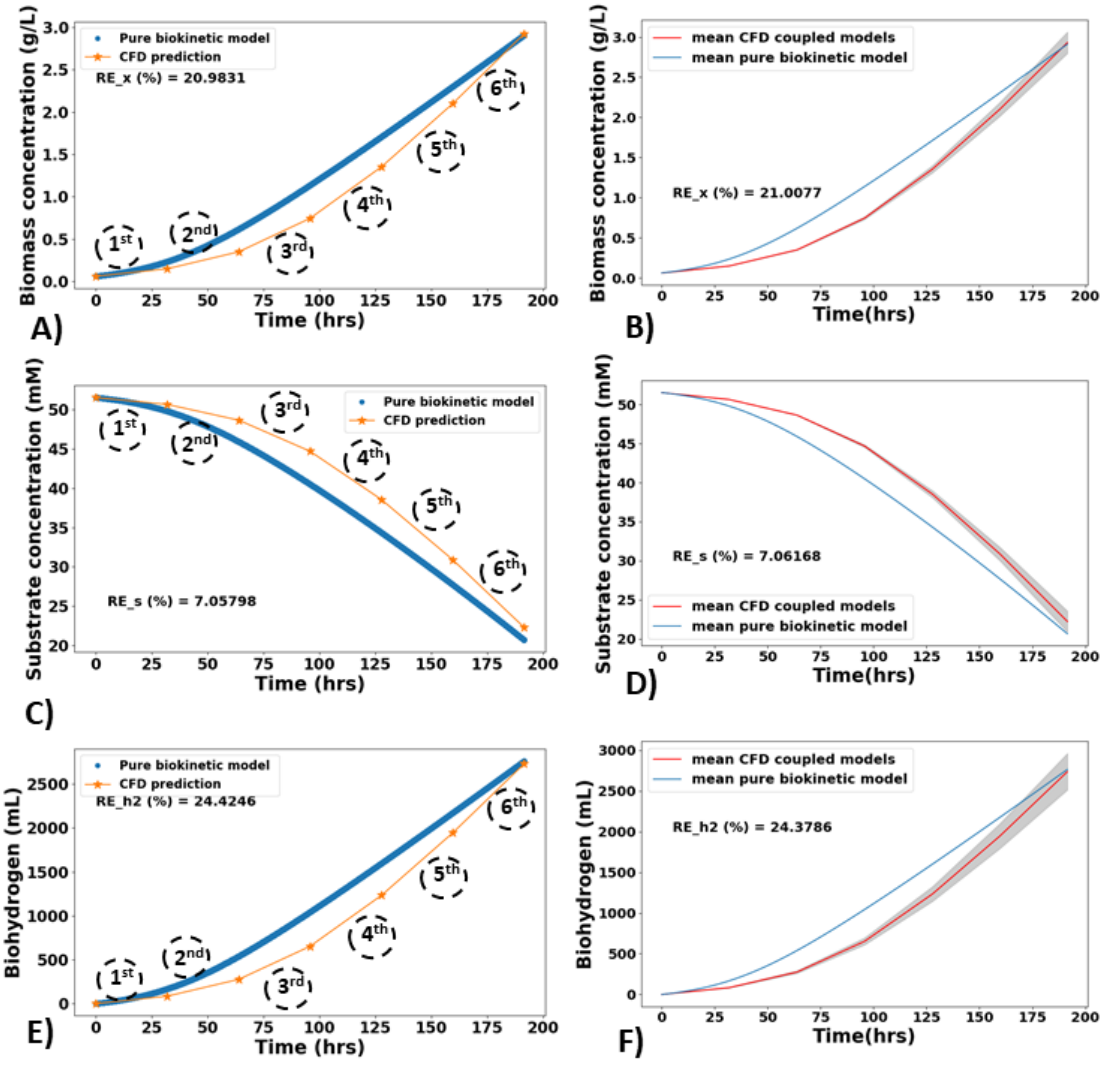

Figure 5.6: CFD end of pass prediction for the column's volume average results for A) biomass growth, C) substrate consumption, and E) biohydrogen production compared to the respective pure biokinetic simulation as the data. B), C) and F) shows CFD uncertainty propagation results for the state variables. The numbers enclosed within broken circles denote the pass number and the asterisk demarcates the end of that pass. The percentage relative errors (% RE) between the CFD and actual biokinetic predictions are indicated in each plot.

5.3.4 Uncertainty propagation results

The uncertainty bands in Figure 5.6 B), D) and F) shows the degree of variability in the predictions from the biokinetic model parameters into the CFD coupled hydrodynamic-biokinetic model as well as the pure biokinetic model in Appendix C. For all state variables, the propagated uncertainty increased with time, demonstrating that the models were

responsive to changes in the parameter input space while not being too sensitive, in agreement Anye Cho et al., [2]. Comparing the two models, the uncertainty of the pure biokinetic model approaches that of the coupled hydrodynamic-biokinetic model towards the end of the last (i.e., 6th) pass. This similarity suggests that the CFD hydrodynamic to biokinetic coupling was robust to false diffusion related errors. Also, the comparable percentage deviation between the two mean Monte Carlo predictions in Figure 5.6 B), D) and F) to those of Appendix C (i.e., without Monte Carlo) suggest that both models will perform the same under mild level of uncertainty provided that the solution quality in Section 5.3.3 was improved (i.e., minimise the high %RE in intermediary passes). Overall, this implies that the mathematically derived hydrodynamic and transport phenomena related parameters in the literature [2,52] and the formulated Eq. (5.12) to Eq. (5.14) for estimating the VT-PBR's intrinsic parameters were theoretically sound, meaning they can be perturbated directly to investigate the hydrodynamic influence on the overall PBR's productivity.

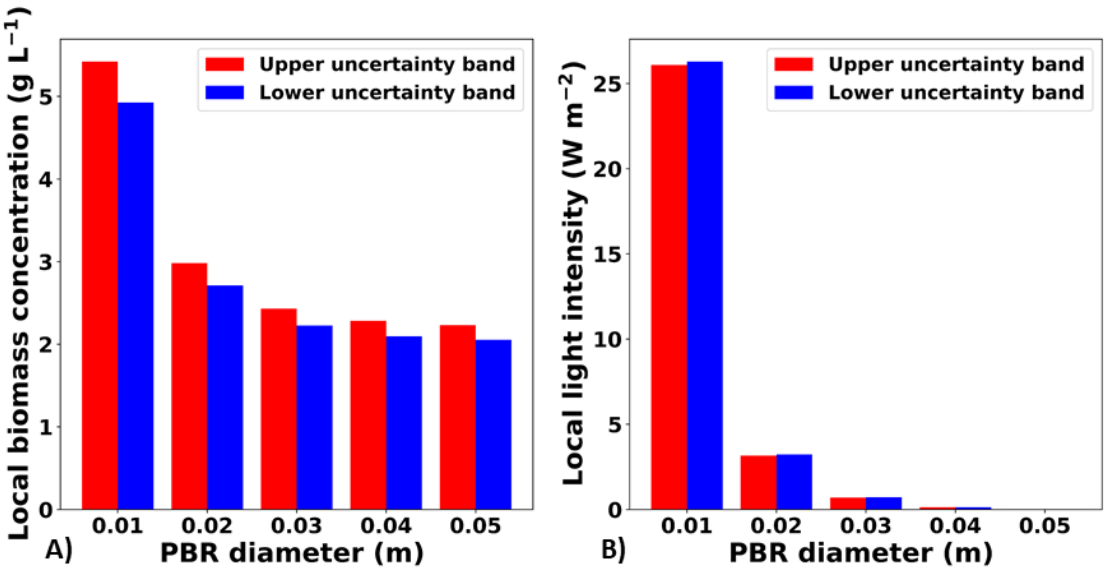

Figure 5.7: Effects of uncertainty propagation in the CFD coupled hydrodynamic-biokinetic models at the end of the final pass. The x-axis of A) and B) corresponds to volume averages for 0.01 m intervals through the vertical height of the vertical column for the lower and upper uncertainty bands respectively.

Also, the influence of the CFD coupled hydrodynamic-biokinetic model's uncertainty propagation on the local state variables (e.g., distribution of biomass concentration) and growth limiting factors (i.e., local light intensity) were further analysed with the lower and upper uncertainty bands at the end of the final pass. This was since the literature studies [21,76] considered optimisation of the biomass concentration at the final cultivation period.

For this, the column was vertically split up into 5 equal sections (0.01 m each) along the PBR's light path length (a scalable variable) and the volume averages of the local biomass concentration and local light intensities reported respectively in Figure 5.7 A) and B). The results showed (i) slight inverse correlation between local biomass concentration and local light intensity, (ii) strong coupling between local biomass concentration and light intensity as they both decrease with increasing PBR's diameter, (iii) local light intensity was critically low (i.e., < 5 W m^{-2}) beyond 0.02 m. Meanwhile the implications of (ii) and (iii) for the design and upscaling of PBRs have already been discussed in the literature [78,165], (i) is revealed herein as an interacting effect which could increase to significant levels with increasing uncertainty bands. Hence, the PBR's optimisation under uncertainty might guarantee a good compromise between the uncertainties's upper and lower bands while not violating this inverse correlation for the optimal solution

5.4. Conclusion

This paper presents a cost-efficient CFD based framework exploiting parallelised computing environment, and cost-saving accelerated growth kinetics, for the modelling of light and bioreaction species transport in a vertical tubular photobioreactor under uncertainty. The simulated (i) velocities and (ii) bioreaction species (i.e., biomass growth, substrate consumption and biohydrogen production) agreed well with the experimental data to within 10% and 24% respectively. However, the absence of radially dominated flow patterns in the simulated velocities suggests the need for the PBR's structural optimisation to eliminate stagnant near-wall regions. Regarding the increasing accuracy for the simulated bioreaction species with increased number of simulated passes, it has been found that there is a trade-off between the simulation accuracy and computational cost. Therefore, optimisation of the PBR's flow and biohydrogen productivity under uncertainty are now computationally feasible.

Acknowledgement

The author Mr. B. Anye Cho is fully funded by the Commonwealth Scholarship Commission, United Kingdom. We would like to thank Prof. Robert Pott at Stellenbosch University, South Africa for providing the experimental datasets.

Appendix C: Equations for mean residence analysis

$$C(t) = \phi_{outlet}(t) \tag{C1}$$

$$E(t) = \frac{C(t)}{\int_0^\infty C(t)\,dt} = \frac{C(t)}{\sum_i C(t)_i \cdot \Delta t} \tag{C2}$$

$$t_m = \int_0^\infty E(t) \cdot t\,dt = \sum_i E(t)_i \cdot t \cdot \Delta t \tag{C3}$$

Whereby ϕ_{outlet} is the passive scalar at the outlet section, $C(t)$ and $E(t)$ are the C-curve and the E-curve, while $\Delta t = 0.5$ s is the time step size and t_m is the mean residence time.

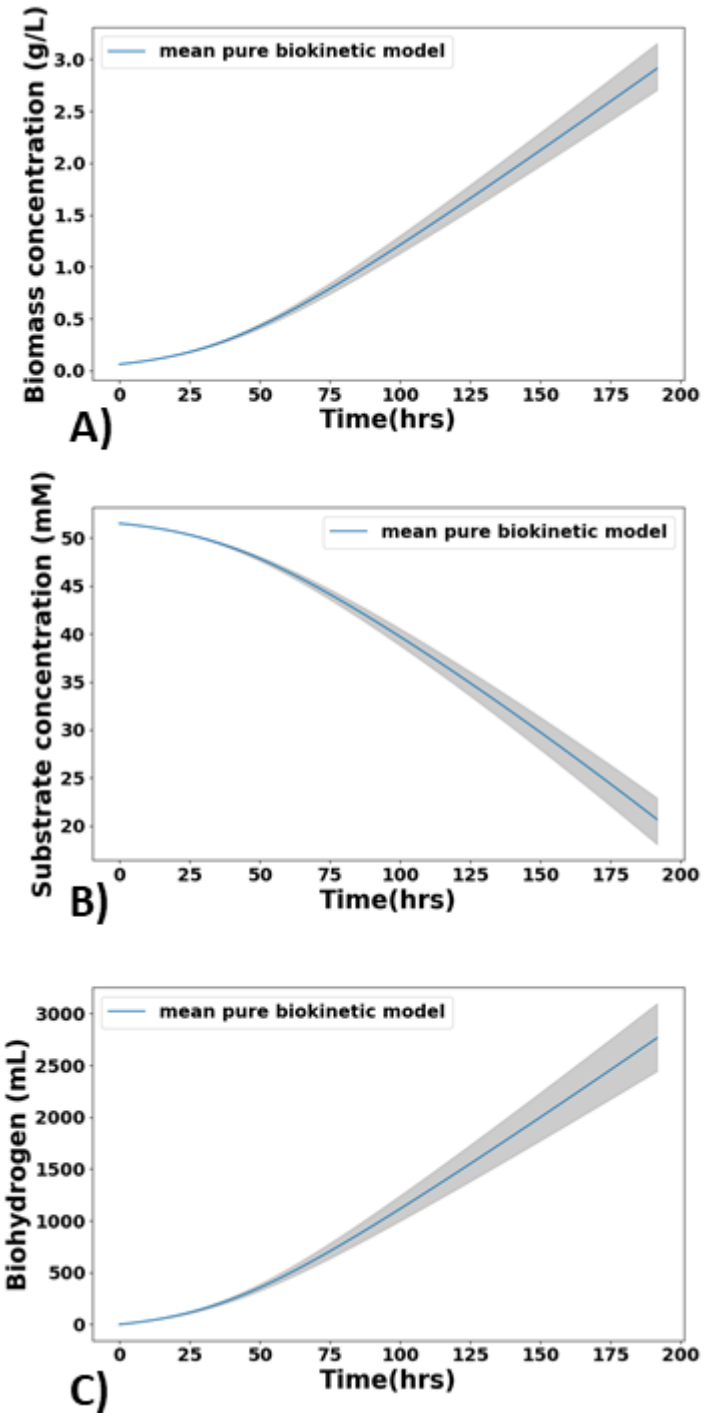

Figure C 5.8: Uncertainty propagation results for state variables: A) biomass concentration, B) substrate concentration, and C) biohydrogen production of the pure biokinetic model.

Chapter 6

Conclusions and Future Directions

Chapter 6 represents the last Chapter of this PhD thesis, and it is broken down into two main sub-chapters. The first sub-chapter covers the conclusions arrived within this research work whereas the second sub-chapter covers the future directives of the work.

6.1 Conclusion

Bio-based products, fuels, and materials are sustainable options for tackling the ever-increasing mass and energy demands of the world's rapid growing population growth. However, current small-scale productions in closed photobioreactors (PBRs) are associated with high costs compared to fossil-based alternatives, thus hindering their commercialisation. In order to attain economic viability, the biotechnological transfer from smaller PBR scales, into pilot plants, and industrial scales presents a major engineering challenge for now and the near future. Prior to the work conducted as part of this PhD thesis, the overall progress was prohibitively slowed by several bottlenecks but primarily due to light attenuation challenges; uneven light distribution due to cellular absorption and mutual shading, and the other PBR local environmental conditions like nutrient and pH gradients, biohydrogen partial pressures, just to highlight a few. Presently, the contributions of this PhD thesis via the three original publications have significantly advanced this area as summarised in the subsequent paragraphs.

In Chapter 3, light attenuation challenges, reportedly the primary bottleneck for upscaling PBRs was tackled by proposing the first mechanistic model to directly integrate the effect of PBR mixing-induced light/dark cycles into biomass growth kinetics via a new parameter, the *effective light coefficient*. To estimate its value, *in silico* experiments within a Flat plate PBR and for the cultivation red marine alga *Porphyridium* sp., were designed in a Computational Fluid Dynamic (CFD) solver. As a result of the expensive nature of such PDE simulations, a cost-efficient accelerated growth kinetics strategy for coupling bioreactor fluid dynamics with biomass growth kinetics and light transmission was proposed and validated. This enabled the simulation of all 10 *in silico* experiments within feasible wall-clock time to enable the optimisation of the *effective light coefficient*. From this, the *effective light coefficient* was linked to the photobioreactor gas inflow rates via a non-linear correlation. Hence, the PBR gas inflow rates can now be easily optimised and controlled to alleviate light attenuation and maintain a high biomass growth rate.

Despite the breakthrough in Chapter 3, the proposed multiscale photo-bioreactive transport model was validated for only one microbial strain and PBR design. Hence, the systematic biotechnological transfer to other PBR scales, configurations and for the cultivations of different microbial strains were still unclear. Therefore, Chapter 4 exploits two different types of PBR: Schott bottle-based (500 mL) and vertical tubular-based (1 L) for the cultivation of the photosynthetic bacterium *Rhodopseudomonas palustris*. To account for the other PBR local environmental conditions influencing PBR upscaling, Chapter 3's mechanistic model was extended to unify the complicated influences of light intensity, light attenuation and temperature to the light/dark cycles experienced by *Rhodopseudomonas palustris* during biomass and biohydrogen production. Through theoretical derivation and perturbation analysis, two parameters: the *effective light coefficient* (Chapter 3's contribution) and the *biohydrogen enhancement coefficient* (Chapter 4's contribution), both linked to the photobioreactor's transport phenomena, were proposed and validated for recalibrations during scale-up predictions and/or across the configuration predictions.

Among the two investigated PBR types in Chapter 4, the scalable vertical tubular PBR possesses: (i) a high surface-area-to-volume ratio in the main column, and (ii) efficient mixing with low shear rate via a peristaltic pump, which maximises the photosynthetic efficiency thereby enhancing the biohydrogen productivity. With the greater goal of optimising and upscaling biohydrogen production, Chapter 5 investigates the coupling of hydrodynamics, to light transmission and bioreaction transport from Chapter 4, through the column and a peristaltic pump. This was found to be computational infeasibilities. Therefore, a cost-saving CFD framework approximating the complexities of the peristaltic pump with inlet-outlet boundary conditions (BCs), introducing mean residence time (t_m) for updating the BCs during simulation, and unifying t_m-dependent accelerated growth kinetics to a parallelised CFD environment was proposed. Due to superior cost savings compared to previous CFD studies, the bioprocess reliability under 5% coupled CFD-photo-bioreaction parameter uncertainties was investigated for the first time with Monte Carlo simulations. To thoroughly validate the proposed CFD photobioreactive transport modelling strategy, experimental tracer dye studies and bioreaction data (biomass, substrate and biohydrogen as seen in Chapter 4) were exploited. The simulated velocities agreed to within 10 % of error, and similar output uncertainties between the coupled CFD-photo-bioreactions and pure photo-bioreactions models were observed. With the model, undesired regions with poor radial mixing were identified and static mixers were suggested to enhance the PBR's radial mixing. By eliminating the stagnant regions, PBR's long light/dark cycles, biohydrogen partial pressures, and biohydrogen productivity can now be optimised.

6.2 Future directions

Whilst Chapters 3 to 5 show cased the significant contributions from this PhD thesis, the complete biotechnological transfer from smaller PBR scales, into pilot plants, and industrial scales is still far from sufficient maturity. This is partly because of the investigations presented herein, were carried out in laboratory scale PBR configurations. Nonetheless, some interesting insights were gained and led to identification of the following future directions:

6.2.1 Model-based control of PBR mixing to alleviate light attenuation and maintain a high biomass growth rate.

It was acknowledged in Chapter 3 that the original nonlinear correlation linking the *effective light coefficient* to the PBR gas inflow rates had an upper bound beyond which its prediction fails. Since this was unexplored, a future directive would be to experimentally cultivate the microbial cells at various PBR gas inflow rates to identify their intrinsic biological limits for tolerating high mixing induced shear stresses. This cannot be achieved *in silico* but with sufficient experimental growth data sets, the proposed model parameters can be recalibrated to enhance the prediction fidelity for a wider manipulated range of PBR gas inflow rates. Also, the proposed model is flexible enough for the incorporation of additional manipulated variables like the influences of PBR incident light intensities and dual-directional (i.e., instead of just uni-directional) illumination. The latter manipulated variable has been shown to enhanced biomass growth in literature studies for faster growing strains like *Desmodesmus sp.*, by the authors Del Rio-Chanona et al., [170] and *Scenedesmus obtusiusculus* by the authors Koller et al., [171]. Therefore, it would be interesting to compare the outcome of both techniques.

6.2.2 Robust optimisation of static mixer design for maximising biomass and biohydrogen productivity in a tubular PBR: A combined CFD-machine learning driven approach.

The identification of undesired regions with poor radial mixing was a major finding with the proposed CFD photobioreactive transport model in Chapter 5. Elsewhere in the literatures [51,160,227,228], static mixers have been demonstrated to enhance radial mixing thereby eliminating stagnant regions within the PBRs. This concept was quickly tested by introducing static mixer design variables: (i) battle length B_L, (ii) baffle spacing B_H, and (iii) baffle inclination angle B_θ as seen in Figure 6.1 A). The preliminary results in Figure 6.1 B) shows the appearance of swirly flows which are desired to induce radial mixing within the PBR. Due to the promising results, the three static mixer design variables are to be optimised

together with the biomass growth and biohydrogen productivity. Therefore, it is recommended to use Chapter 5's cost efficient CFD photobioreactive transport modelling strategy to generate the numerous *in silico* experiments from the sampled design variable space. Then, state-of-art machine learning algorithms can be employed to learn from and replace the CFD simulations. The obtained surrogate model now becomes cheap to evaluate and suitable for the optimisation studies.

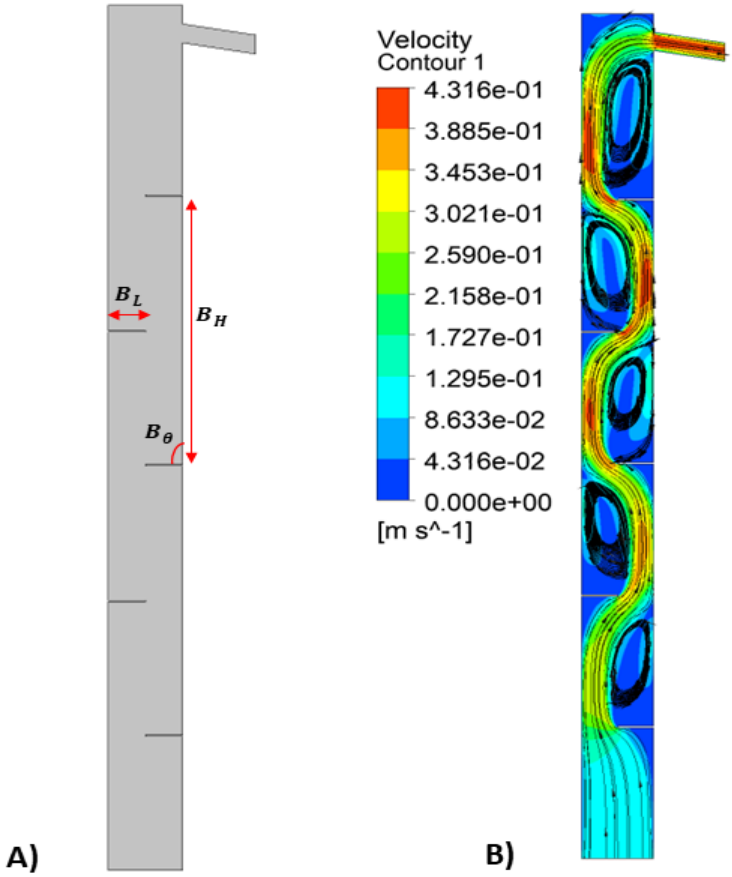

Figure 6.1: Future work showing A) some identified geometrical parameters influencing radial mixing within the VT-PBR to be later optimise, and B) CFD visualisation showing the creation of radial mixing within the VT-PBR when these geometrical parameters are included.

6.2.3 Application to other scalable PBR configurations.

Although different PBR configurations such as (i) flat plate/bubble column PBRs, (ii) schott bottle PBRs and (iii) vertical tubular PBRs, has been explored within this PhD research, there exist a plethora of other scalable configurations targeting diverse metabolite productions. For example, continuous stirred tank reactors (CSTR) PBRs [48–50], and airlift driven PBRs [54,55] has been extensively exploited in academia and the biorefinery, cosmetic, pharmaceutical, and aquacultural industries. These PBR configurations exploit

different mixing mechanisms to achieve microbial cell circulation, hence, correlating these to the Light/Dark cycles, effects of substrate and temperature, and PBR biohydrogen partial pressure, is of utmost interest herein.

Starting with CSTR based PBRs, efficient mixing and microbial cell circulation is mainly achieved with mechanical agitation by impellers (blades connected to a shaft and rotated with a motor). The important optimal operational parameters, for examples impeller design, required number of impeller rotations, and desired mixing regime, just to name a few, has been detailed in the literature [48–50]. Therefore, by directly correlating the Reynolds number of these CSTR based PBRs to the *effective light coefficient* as discussed in Chapter 3, the herein formulated mathematical models are exploitable for the optimal control of these PBRs. However, these CSTR based PBRs are often sparged (e.g., oxygen and CO_2 supply, etc.) depending on the microbial biological demand, thus creating a gas-liquid-solid multiphase system. As biomass growth is optimised by manipulating the impeller rotation speed to alleviate light attenuation, the microbial biological demand is expected to varying considerably. Therefore, the sparging rate is to be concurrently manipulated with the impeller rotation speed to maintain the biomass growth rate at the theoretical maximum. Nevertheless, increasing and/or decreasing the supply of the gasses would consequentially affect the cell growth rates. For example, altering the PBR's CO_2 will offset the operational pH, thus limiting cell growth rate. Hence, the gas mass transfer coefficients are key parameters to be investigated and then embedded into the proposed mathematical models.

Unlike CSTR based PBRs, airlift driven PBRs are void of internal moving parts. They are equipped with an airlift pump and either a draft tube (internal loop) or an external loop. The airlift principle, upward displacement of less dense gas–liquid mixture through the higher density surrounding liquid, is how efficient mixing and microbial cell circulation is attained. Just like sparged CSTR based PBRs, gas-liquid-solid multiphase system is obtained and the caveat on the gas mass transfer coefficients are to be investigated and embedded into the model.

Reference

[1] Dechatiwongse P, Srisamai S, Maitland G, Hellgardt K. Effects of light and temperature on the photoautotrophic growth and photoinhibition of nitrogen-fixing cyanobacterium Cyanothece sp. ATCC 51142. Algal Res 2014;5:103–11. https://doi.org/10.1016/j.algal.2014.06.004.

[2] Anye Cho B, Ross BS, du Toit JP, Pott RWMC, del Río Chanona EA, Zhang D. Dynamic modelling of Rhodopseudomonas palustris biohydrogen production: Perturbation analysis and photobioreactor upscaling. Int J Hydrogen Energy 2021;46:36696–708. https://doi.org/10.1016/j.ijhydene.2021.08.162.

[3] Pilon L, Berberoğlu H, Kandilian R. Radiation transfer in photobiological carbon dioxide fixation and fuel production by microalgae. J Quant Spectrosc Radiat Transf 2011;112:2639–60. https://doi.org/10.1016/j.jqsrt.2011.07.004.

[4] Bayod-Rújula AA. Solar photovoltaics (PV). Solar Hydrogen Production, Elsevier; 2019, p. 237–95. https://doi.org/10.1016/B978-0-12-814853-2.00008-4.

[5] Green MA, Emery K, Hishikawa Y, Warta W. Solar cell efficiency tables (version 36). Progress in Photovoltaics: Research and Applications 2010;18:346–52. https://doi.org/10.1002/pip.1021.

[6] Tang C, Li S, Li M, Xie GH. Bioethanol Potential of Energy Sorghum Grown on Marginal and Arable Lands. Front Plant Sci 2018;9:1–11. https://doi.org/10.3389/fpls.2018.00440.

[7] Kim S, Dale BE. Life cycle assessment of various cropping systems utilized for producing biofuels: Bioethanol and biodiesel. Biomass Bioenergy 2005;29:426–39. https://doi.org/10.1016/j.biombioe.2005.06.004.

[8] Dong Y. Hynol-An economical process for methanol production from biomass and natural gas with reduced CO2 emission. Int J Hydrogen Energy 1997;22:971–7. https://doi.org/10.1016/S0360-3199(96)00198-X.

[9] Demirbaş A. Yields of hydrogen-rich gaseous products via pyrolysis from selected biomass samples. Fuel 2001;80:1885–91. https://doi.org/10.1016/S0016-2361(01)00070-9.

[10] Hill J, Nelson E, Tilman D, Polasky S, Tiffany D. Environmental, economic, and energetic costs and benefits of biodiesel and ethanol biofuels. Proc Natl Acad Sci U S A 2006;103:11206–10. https://doi.org/10.1073/pnas.0604600103.

[11] Brosse N, Dufour A, Meng X, Sun Q, Ragauskas A. Miscanthus : a fast-growing crop for biofuels and chemicals production. Biofuels, Bioproducts and Biorefining 2012;6:580–98. https://doi.org/10.1002/bbb.1353.

[12] Hartman JC, Nippert JB, Orozco RA, Springer CJ. Potential ecological impacts of switchgrass (Panicum virgatum L.) biofuel cultivation in the Central Great Plains, USA. Biomass Bioenergy 2011;35:3415–21. https://doi.org/10.1016/j.biombioe.2011.04.055.

[13] Chisti Y. Biodiesel from microalgae beats bioethanol. Trends Biotechnol 2008;26:126–31. https://doi.org/10.1016/j.tibtech.2007.12.002.

[14] Li M, Hu D, Liu H. Photobioreactor with ideal light-dark cycle designed and built from mathematical modeling and CFD simulation. Ecol Eng 2014;73:162–7. https://doi.org/10.1016/j.ecoleng.2014.09.010.

[15] Pruvost J, Cornet JF, Legrand J. Hydrodynamics influence on light conversion in photobioreactors: An energetically consistent analysis. Chem Eng Sci 2008;63:3679–94. https://doi.org/10.1016/j.ces.2008.04.026.

[16] Gao X, Kong B, Vigil RD. Simulation of algal photobioreactors: recent developments and challenges. Biotechnol Lett 2018;40:1311–27. https://doi.org/10.1007/s10529-018-2595-3.

[17] Lu H, Zhang G, He S, Peng C, Ren Z. Production of photosynthetic bacteria using organic wastewater in photobioreactors in lieu of a culture medium in fermenters: From lab to pilot scale. J Clean Prod 2020;259:120871. https://doi.org/10.1016/j.jclepro.2020.120871.

[18] Scoma A, Giannelli L, Faraloni C, Torzillo G. Outdoor H 2 production in a 50-L tubular photobioreactor by means of a sulfur-deprived culture of the microalga Chlamydomonas reinhardtii. J Biotechnol 2012;157:620–7. https://doi.org/10.1016/j.jbiotec.2011.06.040.

[19] Adessi A, Torzillo G, Baccetti E, de Philippis R. Sustained outdoor H2 production with Rhodopseudomonas palustris cultures in a 50L tubular

photobioreactor. Int J Hydrogen Energy 2012;37:8840–9. https://doi.org/10.1016/j.ijhydene.2012.01.081.

[20] Ali H, Solsvik J, Wagner JL, Zhang D, Hellgardt K, Park CW. CFD and kinetic-based modeling to optimize the sparger design of a large-scale photobioreactor for scaling up of biofuel production. Biotechnol Bioeng 2019;116:2200–11. https://doi.org/10.1002/bit.27010.

[21] del Rio-Chanona EA, Wagner JL, Ali H, Fiorelli F, Zhang D, Hellgardt K. Deep learning-based surrogate modeling and optimization for microalgal biofuel production and photobioreactor design. AIChE Journal 2019;65:915–23. https://doi.org/https://doi.org/10.1002/aic.16473.

[22] Fernández I, Acién FG, Berenguel M, Guzmán JL. First Principles Model of a Tubular Photobioreactor for Microalgal Production. Ind Eng Chem Res 2014;53:11121–36. https://doi.org/10.1021/ie501438r.

[23] Lindblad P, Fuente D, Borbe F, Cicchi B, Conejero JA, Couto N, et al. CyanoFactory, a European consortium to develop technologies needed to advance cyanobacteria as chassis for production of chemicals and fuels. Algal Res 2019;41. https://doi.org/10.1016/j.algal.2019.101510.

[24] Wu X, Merchuk JC. Simulation of algae growth in a bench scale internal loop airlift reactor. Chem Eng Sci 2004;59:2899–912. https://doi.org/10.1016/j.ces.2004.02.019.

[25] Wu X, Merchuk JC. Simulation of algae growth in a bench-scale bubble column reactor. Biotechnol Bioeng 2002;80:156–68. https://doi.org/10.1002/bit.10350.

[26] Béchet Q, Shilton A, Guieysse B. Modeling the effects of light and temperature on algae growth: state of the art and critical assessment for productivity prediction during outdoor cultivation. Biotechnol Adv 2013;31:1648–63.

[27] Gao X, Kong B, Dennis Vigil R. Comprehensive computational model for combining fluid hydrodynamics, light transport and biomass growth in a Taylor vortex algal photobioreactor: Eulerian approach. Algal Res 2017;24:1–8. https://doi.org/10.1016/j.algal.2017.03.009.

[28] Gao X, Kong B, Vigil RD. Comprehensive computational model for combining fluid hydrodynamics, light transport and biomass growth in a Taylor vortex algal photobioreactor: Lagrangian approach. Bioresour Technol 2017;224:523–30. https://doi.org/10.1016/j.biortech.2016.10.080.

[29] Eilers PHC, Peeters JCH. A model for the relationship between light intensity and the rate of photosynthesis in phytoplankton. Ecol Modell 1988;42:199–215. https://doi.org/10.1016/0304-3800(88)90057-9.

[30] Akkerman I, Janssen M, Rocha J, Wijffels RH. Photobiological hydrogen production: Photochemical efficiency and bioreactor design. Int J Hydrogen Energy, vol. 27, 2002, p. 1195–208. https://doi.org/10.1016/S0360-3199(02)00071-X.

[31] Berberoglu H, Gomez PS, Pilon L. Radiation characteristics of Botryococcus braunii, Chlorococcum littorale, and Chlorella sp. used for CO2fixation and biofuel production. J Quant Spectrosc Radiat Transf 2009;110:1879–93. https://doi.org/10.1016/j.jqsrt.2009.04.005.

[32] Mills LA, Moreno-Cabezuelo JÁ, Włodarczyk A, Victoria AJ, Mejías R, Nenninger A, et al. Development of a Biotechnology Platform for the Fast-Growing Cyanobacterium Synechococcus sp. PCC 11901. Biomolecules 2022;12:872. https://doi.org/10.3390/biom12070872.

[33] Lindberg P, Park S, Melis A. Engineering a platform for photosynthetic isoprene production in cyanobacteria, using Synechocystis as the model organism. Metab Eng 2010;12:70–9. https://doi.org/10.1016/j.ymben.2009.10.001.

[34] Balskus EP, Walsh CT. The Genetic and Molecular Basis for Sunscreen Biosynthesis in Cyanobacteria. Science (1979) 2010;329:1653–6. https://doi.org/10.1126/science.1193637.

[35] Zhang D, Xiao N, Mahbubani KT, del Rio-Chanona EA, Slater NKH, Vassiliadis VS. Bioprocess modelling of biohydrogen production by Rhodopseudomonas palustris: Model development and effects of operating conditions on hydrogen yield and glycerol conversion efficiency. Chem Eng Sci 2015;130:68–78. https://doi.org/10.1016/j.ces.2015.02.045.

[36] Carvalho AP, Silva SO, Baptista JM, Malcata FX. Light requirements in microalgal photobioreactors: An overview of biophotonic aspects. Appl Microbiol Biotechnol 2011;89:1275–88. https://doi.org/10.1007/s00253-010-3047-8.

[37] Olivieri G, Gargiulo L, Lettieri P, Mazzei L, Salatino P, Marzocchella A. Photobioreactors for microalgal cultures: A Lagrangian model coupling hydrodynamics and kinetics. Biotechnol Prog 2015;31:1259–72. https://doi.org/10.1002/btpr.2138.

[38] García-Camacho F, Sánchez-Mirón A, Molina-Grima E, Camacho-Rubio F, Merchuck JC. A mechanistic model of photosynthesis in microalgae including photoacclimation dynamics. J Theor Biol 2012;304:1–15. https://doi.org/10.1016/j.jtbi.2012.03.021.

[39] Nikolaou A, Hartmann P, Sciandra A, Chachuat B, Bernard O. Dynamic coupling of photoacclimation and photoinhibition in a model of microalgae growth. J Theor Biol 2016;390:61–72. https://doi.org/10.1016/j.jtbi.2015.11.004.

[40] Deo D, Ozgur E, Eroglu I, Gunduz U, Yucel M. Photofermentative Hydrogen Production in Outdoor Conditions. Hydrogen Energy - Challenges and Perspectives, 2012. https://doi.org/10.5772/50390.

[41] Azwar MY, Hussain MA, Abdul-Wahab AK. Development of biohydrogen production by photobiological, fermentation and electrochemical processes: A review. Renewable and Sustainable Energy Reviews 2014;31:158–73. https://doi.org/10.1016/j.rser.2013.11.022.

[42] Hallenbeck PC, Benemann JR. Biological hydrogen production; Fundamentals and limiting processes. Int J Hydrogen Energy 2002;27:1185–93. https://doi.org/10.1016/S0360-3199(02)00131-3.

[43] Eroglu E, Melis A. Photobiological hydrogen production: Recent advances and state of the art. Bioresour Technol 2011;102:8403–13. https://doi.org/10.1016/j.biortech.2011.03.026.

[44] Cho BA, Pott RWM. The development of a thermosiphon photobioreactor and analysis using Computational Fluid Dynamics (CFD). Chemical

Engineering Journal 2019;363:141–54. https://doi.org/10.1016/j.cej.2019.01.104.

[45] Pulz O. Photobioreactors: Production systems for phototrophic microorganisms. Appl Microbiol Biotechnol 2001;57:287–93. https://doi.org/10.1007/s002530100702.

[46] Yen H-W, Hu I-C, Chen C-Y, Nagarajan D, Chang J-S. Design of photobioreactors for algal cultivation. Second Edi. Elsevier B.V.; 2019. https://doi.org/10.1016/b978-0-444-64192-2.00010-x.

[47] Roshdy A. Utilizing wastewater as a nutrition source for the cultivation of Chlorella Vulgaris. The American University in Cairo, 2019. https://doi.org/10.13140/RG.2.2.11708.49286.

[48] Elqotbi M, Vlaev SD, Montastruc L, Nikov I. CFD modelling of two-phase stirred bioreaction systems by segregated solution of the Euler-Euler model. Comput Chem Eng 2013;48:113–20. https://doi.org/10.1016/j.compchemeng.2012.08.005.

[49] Zhang T. Dynamics of fluid and light intensity in mechanically stirred photobioreactor. J Biotechnol 2013;168:107–16. https://doi.org/10.1016/j.jbiotec.2013.07.007.

[50] Delafosse A, Calvo S, Collignon ML, Delvigne F, Crine M, Toye D. Euler-Lagrange approach to model heterogeneities in stirred tank bioreactors - Comparison to experimental flow characterization and particle tracking. Chem Eng Sci 2015;134:457–66. https://doi.org/10.1016/j.ces.2015.05.045.

[51] Wang L, Wang Q, Zhao R, Tao Y, Ying KZ, Mao XZ. Novel Flat-Plate Photobioreactor with Inclined Baffles and Internal Structure Optimization to Improve Light Regime Performance. ACS Sustain Chem Eng 2021;9:1550–8. https://doi.org/10.1021/acssuschemeng.0c06109.

[52] Anye Cho B, Carvalho Servia MÁ, del Río Chanona EA, Smith R, Zhang D. Synergising biomass growth kinetics and transport mechanisms to simulate light/dark cycle effects on photo-production systems. Biotechnol Bioeng 2021;118:1932–42. https://doi.org/10.1002/bit.27707.

[53] Pruvost J, Pottier L, Legrand J. Numerical investigation of hydrodynamic and mixing conditions in a torus photobioreactor. Chem Eng Sci 2006;61:4476–89. https://doi.org/10.1016/j.ces.2006.02.027.

[54] Luo HP, Al-Dahhan MH. Verification and validation of CFD simulations for local flow dynamics in a draft tube airlift bioreactor. Chem Eng Sci 2011;66:907–23. https://doi.org/10.1016/j.ces.2010.11.038.

[55] Huang J, Ying J, Fan F, Yang Q, Wang J, Li Y. Development of a novel multi-column airlift photobioreactor with easy scalability by means of computational fluid dynamics simulations and experiments. Bioresour Technol 2016;222:399–407. https://doi.org/10.1016/j.biortech.2016.09.109.

[56] Gao X, Kong B, Vigil RD. Multiphysics simulation of algal growth in an airlift photobioreactor: Effects of fluid mixing and shear stress. Bioresour Technol 2018;251:75–83. https://doi.org/10.1016/j.biortech.2017.12.014.

[57] Nauha EK, Alopaeus V. Modeling method for combining fluid dynamics and algal growth in a bubble column photobioreactor. Chemical Engineering Journal 2013;229:559–68. https://doi.org/10.1016/j.cej.2013.06.065.

[58] Liu Q, Luo Z. Modeling bubble column reactor with the volume of fluid approach: Comparison of surface tension models. Chin J Chem Eng 2019;27:2659–65. https://doi.org/10.1016/j.cjche.2019.02.033.

[59] López-Rosales L, Sánchez-Mirón A, Contreras-Gómez A, García-Camacho F, Battaglia F, Zhao L, et al. Characterization of bubble column photobioreactors for shear-sensitive microalgae culture. Bioresour Technol 2019;275:1–9. https://doi.org/10.1016/j.biortech.2018.12.009.

[60] Basak N, Jana AK, Das D. CFD modeling of hydrodynamics and optimization of photofermentative hydrogen production by Rhodopseudomonas palustris DSM 123 in annular photobioreactor. Int J Hydrogen Energy 2016;41:7301–17. https://doi.org/10.1016/j.ijhydene.2016.02.126.

[61] Teke GM, Gakingo GK, Pott RWM. Towards improved understanding of the hydrodynamics of a semi-partition bioreactor (SPB): A numerical investigation. Chemical Engineering Research and Design 2022;177:210–22. https://doi.org/10.1016/j.cherd.2021.10.026.

[62] Papacek S, Jablonsky J, Petera K. Advanced integration of fluid dynamics and photosynthetic reaction kinetics for microalgae culture systems. BMC Syst Biol 2018;12:1–12. https://doi.org/10.1186/s12918-018-0611-9.

[63] Waldrop MM. Microbes for better sewage treatment. Proceedings of the National Academy of Sciences 2021;118:1–5. https://doi.org/10.1073/pnas.2112863118.

[64] Gupta PL, Lee SM, Choi HJ. A mini review: photobioreactors for large scale algal cultivation. World J Microbiol Biotechnol 2015;31:1409–17. https://doi.org/10.1007/s11274-015-1892-4.

[65] Pires JCM, Alvim-ferraz MCM, Martins FG. Photobioreactor design for microalgae production through computational fl uid dynamics : A review. Renewable and Sustainable Energy Reviews 2017;79:248–54. https://doi.org/10.1016/j.rser.2017.05.064.

[66] Kunjapur AM, Eldridge RB. Photobioreactor design for commercial biofuel production from microalgae. Ind Eng Chem Res 2010;49:3516–26. https://doi.org/10.1021/ie901459u.

[67] Krujatz F, Illing R, Krautwer T, Liao J, Helbig K, Goy K, et al. Light-field-characterization in a continuous hydrogen-producing photobioreactor by optical simulation and computational fluid dynamics. Biotechnol Bioeng 2015;112:2439–49. https://doi.org/10.1002/bit.25667.

[68] Tamburic B, Zemichael FW, Crudge P, Maitland GC, Hellgardt K. Design of a novel flat-plate photobioreactor system for green algal hydrogen production. Int J Hydrogen Energy 2011;36:6578–91. https://doi.org/10.1016/j.ijhydene.2011.02.091.

[69] Posten C. Design principles of photo-bioreactors for cultivation of microalgae. Eng Life Sci 2009;9:165–77. https://doi.org/10.1002/elsc.200900003.

[70] Dasgupta CN, Jose Gilbert J, Lindblad P, Heidorn T, Borgvang SA, Skjanes K, et al. Recent trends on the development of photobiological processes and photobioreactors for the improvement of hydrogen production. Int J Hydrogen Energy 2010;35:10218–38. https://doi.org/10.1016/j.ijhydene.2010.06.029.

[71] Skjånes K, Andersen U, Heidorn T, Borgvang SA. Design and construction of a photobioreactor for hydrogen production, including status in the field. J Appl Phycol 2016;28:2205–23. https://doi.org/10.1007/s10811-016-0789-4.

[72] Li X, Wang Y, Zhang S, Chu J, Zhang M, Huang M, et al. Effects of light/dark cycle, mixing pattern and partial pressure of H2 on biohydrogen production by Rhodobacter sphaeroides ZX-5. Bioresour Technol 2011;102:1142–8. https://doi.org/10.1016/j.biortech.2010.09.015.

[73] Cornet JF, Dussap CG. A simple and reliable formula for assessment of maximum volumetric productivities in photobioreactors. Biotechnol Prog 2009;25:424–35. https://doi.org/10.1002/btpr.138.

[74] Bosma R, van Zessen E, Reith JH, Tramper J, Wijffels RH. Prediction of volumetric productivity of an outdoor photobioreactor. Biotechnol Bioeng 2007;97:1108–20. https://doi.org/10.1002/bit.21319.

[75] Molina E, Fernández J, Acién FG, Chisti Y. Tubular photobioreactor design for algal cultures. J Biotechnol 2001;92:113–31. https://doi.org/10.1016/S0168-1656(01)00353-4.

[76] Zhang D, Chanona EADR, Vassiliadis VS, Tamburic B. Analysis of green algal growth via dynamic model simulation and process optimization. Biotechnol Bioeng 2015;112:2025–39. https://doi.org/10.1002/bit.25610.

[77] Zhang D, Dechatiwongse P, Hellgardt K. Modelling light transmission , cyanobacterial growth kinetics and fl uid dynamics in a laboratory scale multiphase photo-bioreactor for biological hydrogen production. Algal Res 2015;8:99–107. https://doi.org/10.1016/j.algal.2015.01.006.

[78] Socher ML, Löser C, Schott C, Bley T, Steingroewer J. The challenge of scaling up photobioreactors: Modeling and approaches in small scale. Eng Life Sci 2016;16:598–609. https://doi.org/10.1002/elsc.201500134.

[79] Blackman FF. Optima and limiting factors. Ann Bot 1905;os-19:281–96. https://doi.org/10.1093/oxfordjournals.aob.a089000.

[80] Jassby AD, Platt T. Mathematical formulation of the relationship between photosynthesis and light for phytoplankton. Limnol Oceanogr 1976;21:540–7. https://doi.org/10.4319/lo.1976.21.4.0540.

[81] Woodcock A, Newman J. Environmental control. Handbook of Electronic Assistive Technology 2018:149–80. https://doi.org/10.1016/B978-0-12-812487-1.00006-5.

[82] Cullen JJ. On models of growth and photosynthesis in phytoplankton. Deep-Sea Research 1990;37:667–83.

[83] Acién Fernández FG, García Camacho F, Chisti Y. Photobioreactors: light regime, mass transfer, and scaleup. Prog Ind Microbiol 1999;35:231–47. https://doi.org/10.1016/S0079-6352(99)80118-0.

[84] Kroumov AD, Módenes AN, Trigueros DEG, Espinoza-Quiñones FR, Borba CE, Scheufele FB, et al. A systems approach for CO2 fixation from flue gas by microalgae—Theory review. Process Biochemistry 2016;51:1817–32. https://doi.org/10.1016/j.procbio.2016.05.019.

[85] Acién FG, Garcia Camacho F, Sanchez Perez JA, Fernandez Sevilla JM, Molina Grima E, Fernández FGA, et al. Modeling of Biomass Productivity in Tubular Photobioreactors for Microalgal Cultures: Effects of Dilution Rate, Tube Diameter, and Solar Irradiance. Biotechnol Bioeng 1998;58:605–16.

[86] Molina Grima E, Fernández Sevilla JM, Sánchez Pérez JA, García Camacho F. A study on simultaneous photolimitation and photoinhibition in dense microalgal cultures taking into account incident and averaged irradiances. J Biotechnol 1996;45:59–69. https://doi.org/10.1016/0168-1656(95)00144-1.

[87] Baly ECC. The kinetics of photosynthesis. Proc R Soc Lond A Math Phys Sci 1935;149:596–596. https://doi.org/10.1098/rspa.1935.0083.

[88] Smith EL. Photosynthesis in Relation to Light and Carbon Dioxide. Proceedings of the National Academy of Sciences 1936;22:504–11. https://doi.org/10.1073/pnas.22.8.504.

[89] J.C.H. P, P. E. The relationship between light intensity and photosynthesis - a simple mathematical model. Hydrobiol Bull. 1972:134–6.

[90] Bannister TT. Quantitative description of steady state, nutrient-saturated algal growth, including adaptation. Limnol Oceanogr 1979;24:76–96. https://doi.org/10.4319/lo.1979.24.1.0076.

[91] Molina Grima E, Garcia Carnacho F, Sanchez Perez J a, Fernandez Sevilla JM, Acien Fernandez FG, Contreras Gomez A. A mathematical Model of

Microalgal Growth in Light-Limited Chemostat Culture. Journal of Chemical Technology & Biotechnology 1994;61:167–73. https://doi.org/10.1002/jctb.280610212.

[92] Bernard O, Rémond B. Validation of a simple model accounting for light and temperature effect on microalgal growth. Bioresour Technol 2012;123:520–7. https://doi.org/10.1016/j.biortech.2012.07.022.

[93] Kurano N, Miyachi S. Selection of microalgal growth model for describing specific growth rate-light response using extended information criterion. J Biosci Bioeng 2005;100:403–8. https://doi.org/10.1263/jbb.100.403.

[94] Papadakis IA, Kotzabasis K, Lika K. Modeling the dynamic modulation of light energy in photosynthetic algae. J Theor Biol 2012;300:254–64. https://doi.org/10.1016/j.jtbi.2012.01.040.

[95] Han BP. A mechanistic model of algal photoinhibition induced by photodamage to photosystem-II. J Theor Biol 2002;214:519–27. https://doi.org/10.1006/jtbi.2001.2468.

[96] Han BP. Photosynthesis-Irradiance response at physiological level: A mechanistic model. J Theor Biol 2001;213:121–7. https://doi.org/10.1006/jtbi.2001.2413.

[97] Han B-P. Effect of photoinhibition on algal photosynthesis: a dynamic model. J Plankton Res 2000;22:865–85. https://doi.org/10.1093/plankt/22.5.865.

[98] Nikolaou A, Bernardi A, Meneghesso A, Bezzo F, Morosinotto T, Chachuat B. A model of chlorophyll fluorescence in microalgae integrating photoproduction, photoinhibition and photoregulation. J Biotechnol 2015;194:91–9. https://doi.org/10.1016/j.jbiotec.2014.12.001.

[99] Rubio Camacho F, García Camacho F, Fernández Sevilla JM, Chisti Y, Molina Grima E. A mechanistic model of photosynthesis in microalgae. Biotechnol Bioeng 2003;81:459–73. https://doi.org/10.1002/bit.10492.

[100] Bernardi A, Perin G, Sforza E, Galvanin F, Morosinotto T, Bezzo F. An identifiable state model to describe light intensity influence on microalgae growth. Ind Eng Chem Res 2014;53:6738–49. https://doi.org/10.1021/ie500523z.

[101] Wu X, Merchuk JC. A model integrating fluid dynamics in photosynthesis and photoinhibition processes. Chem Eng Sci 2001;56:3527–38. https://doi.org/10.1016/S0009-2509(01)00048-3.

[102] Alagappan G, Cowan RM. Effect of temperature and dissolved oxygen on the growth kinetics of Pseudomonas putida F1 growing on benzene and toluene. Chemosphere 2004;54:1255–65. https://doi.org/10.1016/j.chemosphere.2003.09.013.

[103] Vargas JVC, Mariano AB, Corrêa DO, Ordonez JC. The microalgae derived hydrogen process in compact photobioreactors. Int J Hydrogen Energy 2014;39:9588–98. https://doi.org/10.1016/j.ijhydene.2014.04.093.

[104] Zwietering MH, de Koos JT, Hasenack BE, de Witt JC, van't Riet K. Modeling of bacterial growth as a function of temperature. Appl Environ Microbiol 1991;57:1094–101. https://doi.org/10.1128/aem.57.4.1094-1101.1991.

[105] Zhang D, Dechatiwongse P, del Rio-Chanona EA, Maitland GC, Hellgardt K, Vassiliadis VS. Modelling of light and temperature influences on cyanobacterial growth and biohydrogen production. Algal Res 2015;9:263–74. https://doi.org/10.1016/j.algal.2015.03.015.

[106] Dauta A, Devaux J, Piquemal F, Boumnich L. Growth rate of four freshwater algae in relation to light and temperature. Hydrobiologia 1990;207:221–6. https://doi.org/10.1007/BF00041459.

[107] Sözmen AB, Ata A, Ovez B. Optimization of the algal species Chlorella miniata growth: Mathematical modelling and evaluation of temperature and light intensity effects. Biocatal Agric Biotechnol 2022;39:102239. https://doi.org/10.1016/j.bcab.2021.102239.

[108] Ratkowsky DA, Lowry RK, McMeekin TA, Stokes AN, Chandler RE. Model for bacterial culture growth rate throughout the entire biokinetic temperature range. J Bacteriol 1983;154:1222–6. https://doi.org/10.1128/jb.154.3.1222-1226.1983.

[109] Wang J, Wan W. Kinetic models for fermentative hydrogen production: A review. Int J Hydrogen Energy 2009;34:3313–23. https://doi.org/10.1016/j.ijhydene.2009.02.031.

[110] Obeid J, Flaus JM, Adrot O, Magnin JP, Willison JC. State estimation of a batch hydrogen production process using the photosynthetic bacteria Rhodobacter capsulatus. Int J Hydrogen Energy 2010;35:10719–24. https://doi.org/10.1016/j.ijhydene.2010.02.051.

[111] Luo HP, Al-Dahhan MH. Analyzing and Modeling of Photobioreactors by Combining First Principles of Physiology and Hydrodynamics. Biotechnol Bioeng 2004;85:382–93. https://doi.org/10.1002/bit.10831.

[112] Berberoglu H, Yin J, Pilon L. Light transfer in bubble sparged photobioreactors for H2production and CO2mitigation. Int J Hydrogen Energy 2007;32:2273–85. https://doi.org/10.1016/j.ijhydene.2007.02.018.

[113] Murphy TE, Berberoğlu H. Effect of algae pigmentation on photobioreactor productivity and scale-up: A light transfer perspective. J Quant Spectrosc Radiat Transf 2011;112:2826–34. https://doi.org/10.1016/j.jqsrt.2011.08.012.

[114] Wheaton ZC, Krishnamoorthy G. Modeling radiative transfer in photobioreactors for algal growth. Comput Electron Agric 2012;87:64–73. https://doi.org/10.1016/j.compag.2012.05.002.

[115] Kong B, Vigil RD. Simulation of photosynthetically active radiation distribution in algal photobioreactors using a multidimensional spectral radiation model. Bioresour Technol 2014;158:141–8. https://doi.org/10.1016/j.biortech.2014.01.052.

[116] Cornet JF, Dussap CG, Gros JB, Binois C, Lasseur C. A simplified monodimensional approach for modeling coupling between radiant light transfer and growth kinetics in photobioreactors. Chem Eng Sci 1995;50:1489–500. https://doi.org/10.1016/0009-2509(95)00022-W.

[117] Huang J, Feng F, Wan M, Ying J, Li Y, Qu X, et al. Improving performance of flat-plate photobioreactors by installation of novel internal mixers optimized with computational fluid dynamics. Bioresour Technol 2015;182:151–9. https://doi.org/10.1016/j.biortech.2015.01.067.

[118] Acién Fernández FG, García Camacho F, Sánchez Pérez JA, Fernández Sevilla JM, Molina Grima E. A model for light distribution and average solar irradiance inside outdoor tubular photobioreactors for the microalgal mass culture. Biotechnol Bioeng 1997;55:701–14.

https://doi.org/10.1002/(SICI)1097-0290(19970905)55:5<701::AID-BIT1>3.0.CO;2-F.

[119] Suh IS, Lee SB. A light distribution model for an internally radiating photobioreactor. Biotechnol Bioeng 2003;82:180–9. https://doi.org/10.1002/bit.10558.

[120] Palamae S, Choorit W, Dechatiwongse P, Zhang D, Antonio del Rio-Chanona E, Chisti Y. Production of renewable biohydrogen by Rhodobacter sphaeroides S10: A comparison of photobioreactors. J Clean Prod 2018;181:318–28. https://doi.org/10.1016/j.jclepro.2018.01.238.

[121] Rio-chanona EA, Ahmed N rashid, Zhang D, Lu Y, Jing K. Kinetic Modeling and Process Analysis for Desmodesmus sp. Lutein Photo-Production. AICHE Journal 2017;63:2546–54. https://doi.org/10.1002/aic.

[122] Shin S, Venturelli OS, Zavala VM. Scalable nonlinear programming framework for parameter estimation in dynamic biological system models. PLoS Comput Biol 2019;15:1–29. https://doi.org/10.1371/journal.pcbi.1006828.

[123] Villaverde AF, Fröhlich F, Weindl D, Hasenauer J, Banga JR. Benchmarking optimization methods for parameter estimation in large kinetic models. Bioinformatics 2019;35:830–8. https://doi.org/10.1093/bioinformatics/bty736.

[124] Sadino-Riquelme MC, Rivas J, Jeison D, Hayes RE, Donoso-Bravo A. Making sense of parameter estimation and model simulation in bioprocesses. Biotechnol Bioeng 2020;117:1357–66. https://doi.org/10.1002/bit.27294.

[125] del Rio-Chanona EA, Dechatiwongse P, Zhang D, Maitland GC, Hellgardt K, Arellano-Garcia H, et al. Optimal Operation Strategy for Biohydrogen Production. Ind Eng Chem Res 2015;54:6334–43. https://doi.org/10.1021/acs.iecr.5b00612.

[126] Hedengren JD, Shishavan RA, Powell KM, Edgar TF. Nonlinear modeling, estimation and predictive control in APMonitor. Comput Chem Eng 2014;70:133–48. https://doi.org/10.1016/j.compchemeng.2014.04.013.

[127] Nicholson B, Siirola JD, Watson JP, Zavala VM, Biegler LT. Pyomo.Dae: a Modeling and Automatic Discretization Framework for Optimization With

Differential and Algebraic Equations. Math Program Comput 2018;10:187–223. https://doi.org/10.1007/s12532-017-0127-0.

[128] Sandia National laboratories. Nonlinear problems 2011. https://static1.squarespace.com/static/5492d7f4e4b00040889988bd/t/57bd0faad482e927298cca8f/1472008110099/5_Nonlinear.pdf.

[129] Ranganath M, Renganathan S, Gokulnath C. Identification of bioprocesses using Genetic Algorithm. n.d.

[130] Park LJ, Park CH, Park C, Lee T. Application of genetic algorithms to parameter estimation of bioprocesses. Med Biol Eng Comput 1997;35:47–9. https://doi.org/10.1007/BF02510391.

[131] Saha G, Barua A, Sinha S. Bioreactors. CRC Press; 2017. https://doi.org/10.1201/9781315116266.

[132] Cheema JJS, Sankpal N v, Tambe SS, Kulkarni BD. Genetic programming assisted stochastic optimization strategies for optimization of glucose to gluconic acid fermentation. Biotechnol Prog 2002;18:1356–65. https://doi.org/10.1021/bp015509s.

[133] Roubos JA, van Straten G, van Boxtel AJB. An evolutionary strategy for fed-batch bioreactor optimization; concepts and performance. J Biotechnol 1999;67:173–87. https://doi.org/10.1016/S0168-1656(98)00174-6.

[134] Simutis R, Galvanauskas V, Levisauskas D, Repšytė J. Bioprocess Optimization Based On Relevance Vector Regression Models and Evolutionary Programming Technique. 2014. https://doi.org/10.5281/zenodo.1092289.

[135] Kennedy J, Eberhart RC, Shi Y. The Particle Swarm. Swarm Intelligence, Elsevier; 2001, p. 287–325. https://doi.org/10.1016/B978-155860595-4/50007-3.

[136] Freitas D, Lopes LG, Morgado-Dias F. Particle Swarm Optimisation: A Historical Review Up to the Current Developments. Entropy 2020;22:362. https://doi.org/10.3390/e22030362.

[137] Karaboga D, Akay B. A comparative study of Artificial Bee Colony algorithm. Appl Math Comput 2009;214:108–32. https://doi.org/10.1016/j.amc.2009.03.090.

[138] Salleh AHM, Mohamad MS, Deris S, Omatu S, Fdez-Riverola F, Corchado JM. Gene knockout identification for metabolite production improvement using a hybrid of genetic ant colony optimization and flux balance analysis. Biotechnology and Bioprocess Engineering 2015;20:685–93. https://doi.org/10.1007/s12257-015-0276-9.

[139] Versteeg HK, Malalasekera W. An Introduction to Computational Fluid Dynamics: The Finite Volume Method. 2nd ed. Harlow: Pearson; 2007.

[140] Massart A, Mirisola A, Lupant D, Thomas D, Hantson AL. Experimental characterization and numerical simulation of the hydrodynamics in an airlift photobioreactor for microalgae cultures. Algal Res 2014;6:210–7. https://doi.org/10.1016/j.algal.2014.07.003.

[141] Sato T, Yamada D, Hirabayashi S. Development of virtual photobioreactor for microalgae culture considering turbulent flow and flashing light effect. Energy Convers Manag 2010;51:1196–201. https://doi.org/10.1016/j.enconman.2009.12.030.

[142] Amini H, Wang L, Hashemisohi A, Shahbazi A, Bikdash M, KC D, et al. An integrated growth kinetics and computational fluid dynamics model for the analysis of algal productivity in open raceway ponds. Comput Electron Agric 2018;145:363–72. https://doi.org/10.1016/j.compag.2018.01.010.

[143] Lapin A, Schmid J, Reuss M. Modeling the dynamics of E. coli populations in the three-dimensional turbulent field of a stirred-tank bioreactor-A structured-segregated approach. Chem Eng Sci 2006;61:4783–97. https://doi.org/10.1016/j.ces.2006.03.003.

[144] Gómez-Pérez CA, Espinosa J, Montenegro Ruiz LC, van Boxtel AJB. CFD simulation for reduced energy costs in tubular photobioreactors using wall turbulence promoters. Algal Res 2015;12:1–9. https://doi.org/10.1016/j.algal.2015.07.011.

[145] Amini H. Numerical and Experimental Investigation of a Microalgae cultivation System for Waterwater. North Carolina A&T State University, 2016.

[146] Jebahi M, Dau F, Charles JL, Iordanoff I. Multiscale Modeling of Complex Dynamic Problems: An Overview and Recent Developments. Archives of

Computational Methods in Engineering 2016;23:101–38. https://doi.org/10.1007/s11831-014-9136-6.

[147] Nikolaou A, Booth P, Gordon F, Yang J, Matar O, Chachuat B. Multi-Physics Modeling of Light-Limited Microalgae Growth in Raceway Ponds. IFAC-PapersOnLine 2016;49:324–9. https://doi.org/10.1016/j.ifacol.2016.12.147.

[148] Nauha EK, Alopaeus V. Modeling outdoors algal cultivation with compartmental approach. Chemical Engineering Journal 2015;259:945–60. https://doi.org/10.1016/j.cej.2014.08.073.

[149] Ross BS, Pott RWM. Hydrogen production by immobilized Rhodopseudomonas palustris in packed or fluidized bed photobioreactor systems. Int J Hydrogen Energy 2021;46:1715–27. https://doi.org/10.1016/j.ijhydene.2020.10.061.

[150] Park S, Li Y. Integration of biological kinetics and computational fluid dynamics to model the growth of Nannochloropsis salina in an open channel raceway. Biotechnol Bioeng 2015;112:923–33. https://doi.org/10.1002/bit.25509.

[151] Janssen M, Tramper J, Mur LR, Wijffels RH. Enclosed outdoor photobioreactors: Light regime, photosynthetic efficiency, scale-up, and future prospects. Biotechnol Bioeng 2003;81:193–210. https://doi.org/10.1002/bit.10468.

[152] Vejrazka C, Janssen M, Streefland M, Wijffels RH. Photosynthetic efficiency of chlamydomonas reinhardtii in attenuated, flashing light. Biotechnol Bioeng 2012;109:2567–74. https://doi.org/10.1002/bit.24525.

[153] Papáček Š, Jablonský JJ, Petera K, Rehák B, Matonoha C. Modeling and Optimization of Microalgae Growth in Photobioreactors: A Multidisciplinary Problem, ISCS 2014: Interdisciplinary Symposium on Complex Systems. In: Sanayei A, E. Rössler O, Zelinka I, editors. vol. 14, Cham: Springer International Publishing; 2014, p. 277–86. https://doi.org/10.1007/978-3-319-10759-2.

[154] Han BP. A mechanistic model of algal photoinhibition induced by photodamage to photosystem-II. J Theor Biol 2002;214:519–27. https://doi.org/10.1006/jtbi.2001.2468.

[155] Liu J, Huang J, Che F. Microalgae as Feedstocks for Biodiesel Production. Biodiesel - Feedstocks and Processing Technologies 2011. https://doi.org/10.5772/25600.

[156] Bernstein HC. Unlocking the Constraints of Cyanobacterial Productivity : MBio 2016;7:1–10. https://doi.org/10.1128/mBio.00949-16.Editor.

[157] Solimeno A, Samsó R, Uggetti E, Sialve B, Steyer JP, Gabarró A, et al. New mechanistic model to simulate microalgae growth. Algal Res 2015;12:350–8. https://doi.org/10.1016/j.algal.2015.09.008.

[158] Aiba S. Growth kinetics of photosynthetic microorganisms. Berlin Heidelberg: Springer Berlin Heidelberg; 1982. https://doi.org/10.1007/3540116982_3.

[159] Yang Z, del Ninno M, Wen Z, Hu H. An experimental investigation on the multiphase flows and turbulent mixing in a flat-panel photobioreactor for algae cultivation. J Appl Phycol 2014;26:2097–107. https://doi.org/10.1007/s10811-014-0239-0.

[160] Yu G, Li Y, Shen G, Wang W, Lin C, Wu H, et al. A novel method using CFD to optimize the inner structure parameters of flat photobioreactors. J Appl Phycol 2009;21:719–27. https://doi.org/10.1007/s10811-009-9407-z.

[161] Pfleger D, Gomes S, Gilbert N, Wagner HG. Hydrodynamic simulations of laboratory scale bubble columns fundamental studies of the Eulerian-Eulerian modelling approach. Chem Eng Sci 1999;54:5091–9. https://doi.org/10.1016/S0009-2509(99)00261-4.

[162] Rampure MR, Buwa V v., Ranade V v. Modelling of gas-liquid/gas-liquid-solid flows in bubble columns: Experiments and CFD simulations. Canadian Journal of Chemical Engineering 2003;81:692–706. https://doi.org/10.1002/cjce.5450810348.

[163] Leupold M, Hindersin S, Gust G, Kerner M, Hanelt D. Influence of mixing and shear stress on Chlorella vulgaris, Scenedesmus obliquus, and Chlamydomonas reinhardtii. J Appl Phycol 2013;25:485–95. https://doi.org/10.1007/s10811-012-9882-5.

[164] Zhao L, Gu Y, Peng C, Tang Z. Scale-up of the cross-flow flat-plate airlift photobioreactor. Asia-Pacific Journal of Chemical Engineering 2020:1–12. https://doi.org/10.1002/apj.2518.

[165] Richmond A. Efficient utilization of high irradiance for production of photoautotropic cell mass: A survey. J Appl Phycol 1996;8:381–7. https://doi.org/10.1007/BF02178581.

[166] Grobbelaar JU. Turbulence in mass algal cultures and the role of light/dark fluctuations. J Appl Phycol 1994;6:331–5. https://doi.org/10.1007/BF02181947.

[167] Fujasová M, Linek V, Moucha T. Mass transfer correlations for multiple-impeller gas-liquid contactors. Analysis of the effect of axial dispersion in gas and liquid phases on "local" kL a values measured by the dynamic pressure method in individual stages of the vessel. Chem Eng Sci 2007;62:1650–69. https://doi.org/10.1016/j.ces.2006.12.003.

[168] Moucha T, Linek V, Prokopová E. Gas hold-up, mixing time and gas-liquid volumetric mass transfer coefficient of various multiple-impeller configurations: Rushton turbine, pitched blade and techmix impeller and their combinations. Chem Eng Sci 2003;58:1839–46. https://doi.org/10.1016/S0009-2509(02)00682-6.

[169] Schulze PSC, Brindley C, Fernández JM, Rautenberger R, Pereira H, Wijffels RH, et al. Flashing light does not improve photosynthetic performance and growth of green microalgae. Bioresour Technol Rep 2020;9:100367. https://doi.org/10.1016/j.biteb.2019.100367.

[170] del Rio-Chanona EA, Ahmed NR, Wagner J, Lu Y, Zhang D, Jing K. Comparison of physics-based and data-driven modelling techniques for dynamic optimisation of fed-batch bioprocesses. Biotechnol Bioeng 2019;116:2971–82. https://doi.org/10.1002/bit.27131.

[171] Koller AP, Löwe H, Schmid V, Mundt S, Weuster-Botz D. Model-supported phototrophic growth studies with Scenedesmus obtusiusculus in a flat-plate photobioreactor. Biotechnol Bioeng 2017;114:308–20. https://doi.org/10.1002/bit.26072.

[172] Singh L, Wahid ZA. Methods for enhancing bio-hydrogen production from biological process: A review. Journal of Industrial and Engineering Chemistry 2015;21:70–80. https://doi.org/10.1016/j.jiec.2014.05.035.

[173] Kapdan IK, Kargi F. Bio-hydrogen production from waste materials. Enzyme Microb Technol 2006;38:569–82. https://doi.org/10.1016/j.enzmictec.2005.09.015.

[174] Preethi, Usman TMM, Rajesh Banu J, Gunasekaran M, Kumar G. Biohydrogen production from industrial wastewater: An overview. Bioresour Technol Rep 2019;7:100287. https://doi.org/10.1016/j.biteb.2019.100287.

[175] Giannelli L, Torzillo G. Hydrogen production with the microalga Chlamydomonas reinhardtii grown in a compact tubular photobioreactor immersed in a scattering light nanoparticle suspension. Int J Hydrogen Energy 2012;37:16951–61. https://doi.org/10.1016/j.ijhydene.2012.08.103.

[176] Fouchard S, Pruvost J, Degrenne B, Titica M, Legrand J. Kinetic modeling of light limitation and sulfur deprivation effects in the induction of hydrogen production with Chlamydomonas reinhardtii: Part I. model development and parameter identification. Biotechnol Bioeng 2009;102:232–45. https://doi.org/10.1002/bit.22034.

[177] Zhang D, Dechatiwongse P, del Rio-Chanona EA, Maitland GC, Hellgardt K, Vassiliadis VS. Dynamic modelling of high biomass density cultivation and biohydrogen production in different scales of flat plate photobioreactors. Biotechnol Bioeng 2015;112:2429–38. https://doi.org/10.1002/bit.25661.

[178] Bandyopadhyay A, Stöckel J, Min H, Sherman LA, Pakrasi HB. High rates of photobiological H2 production by a cyanobacterium under aerobic conditions. Nat Commun 2010;1:139. https://doi.org/10.1038/ncomms1139.

[179] Ghosh S, Dairkee UK, Chowdhury R, Bhattacharya P. Hydrogen from food processing wastes via photofermentation using Purple Non-sulfur Bacteria (PNSB) – A review. Energy Convers Manag 2017;141:299–314. https://doi.org/10.1016/j.enconman.2016.09.001.

[180] du Toit J-P, Pott RWM. Heat-acclimatised strains of Rhodopseudomonas palustris reveal higher temperature optima with concomitantly enhanced

biohydrogen production rates. Int J Hydrogen Energy 2021;46:11564–72. https://doi.org/10.1016/j.ijhydene.2021.01.068.

[181] Mabutyana L, Pott RWM. Photo-fermentative hydrogen production by Rhodopseudomonas palustris CGA009 in the presence of inhibitory compounds. Int J Hydrogen Energy 2021. https://doi.org/https://doi.org/10.1016/j.ijhydene.2020.12.189.

[182] Lee C-M, Hung G-J, Yang C-F. Hydrogen production by Rhodopseudomonas palustris WP 3-5 in a serial photobioreactor fed with hydrogen fermentation effluent. Bioresour Technol 2011;102:8350–6. https://doi.org/10.1016/j.biortech.2011.04.072.

[183] Padovani G, Vaičiulytė S, Carlozzi P. BioH 2 photoproduction by means of Rhodopseudomonas palustris sp. cultured in a lab-scale photobioreactor operated in batch, fed-batch and semi-continuous modes. Fuel 2016;166:203–10. https://doi.org/10.1016/j.fuel.2015.10.124.

[184] Wang YZ, Liao Q, Zhu X, Li J, Lee DJ. Effect of culture conditions on the kinetics of hydrogen production by photosynthetic bacteria in batch culture. Int J Hydrogen Energy 2011;36:14004–13. https://doi.org/10.1016/j.ijhydene.2011.04.005.

[185] Kaftan D, Bína D, Koblížek M. Temperature dependence of photosynthetic reaction centre activity in Rhodospirillum rubrum. Photosynth Res 2019;142:181–93. https://doi.org/10.1007/s11120-019-00652-7.

[186] Obeid J, Magnin JP, Flaus JM, Adrot O, Willison JC, Zlatev R. Modelling of hydrogen production in batch cultures of the photosynthetic bacterium Rhodobacter capsulatus. Int J Hydrogen Energy 2009;34:180–5. https://doi.org/10.1016/j.ijhydene.2008.09.081.

[187] Xie G-J, Liu B-F, Xing D-F, Ding J, Nan J, Ren H-Y, et al. The kinetic characterization of photofermentative bacterium Rhodopseudomonas faecalis RLD-53 and its application for enhancing continuous hydrogen production. Int J Hydrogen Energy 2012;37:13718–24. https://doi.org/10.1016/j.ijhydene.2012.02.168.

[188] Koku H, Eroğlu I, Gündüz U, Yücel M, Türker L. Kinetics of biological hydrogen production by the photosynthetic bacterium Rhodobacter

sphaeroides O.U. 001. Int J Hydrogen Energy 2003;28:381–8. https://doi.org/10.1016/S0360-3199(02)00080-0.

[189] Gilbert JJ, Ray S, Das D. Hydrogen production using Rhodobacter sphaeroides (O.U. 001) in a flat panel rocking photobioreactor. Int J Hydrogen Energy 2011;36:3434–41. https://doi.org/10.1016/j.ijhydene.2010.12.012.

[190] Pintucci C, Padovani G, Giovannelli A, Traversi ML, Ena A, Pushparaj B, et al. Hydrogen photo-evolution by Rhodopseudomonas palustris 6A using pre-treated olive mill wastewater and a synthetic medium containing sugars. Energy Convers Manag 2015;90:499–505. https://doi.org/10.1016/j.enconman.2014.11.045.

[191] Boran E, Özgür E, Yücel M, Gündüz U, Eroglu I. Biohydrogen production by Rhodobacter capsulatus in solar tubular photobioreactor on thick juice dark fermenter effluent. J Clean Prod 2012;31:150–7. https://doi.org/10.1016/j.jclepro.2012.03.020.

[192] Androga DD, Sevinç P, Koku H, Yücel M, Gündüz U, Eroglu I. Optimization of temperature and light intensity for improved photofermentative hydrogen production using Rhodobacter capsulatus DSM 1710. Int J Hydrogen Energy 2014;39:2472–80. https://doi.org/10.1016/j.ijhydene.2013.11.114.

[193] Imamoglu E, Sukan FV. Scale-up and kinetic modeling for bioethanol production. Bioresour Technol 2013;144:311–20. https://doi.org/10.1016/j.biortech.2013.06.118.

[194] Ziadi M, M'Hir S, Aydi A, Hamdi M. Bioreactor Scale-Up and Kinetic Modeling of Lactic Acid and Biomass Production by Enterococcus faecalis SLT13 during Batch Culture on Hydrolyzed Cheese Whey. J Chem 2020;2020:1–9. https://doi.org/10.1155/2020/1236784.

[195] Basak N, Das D. The prospect of purple non-sulfur (PNS) photosynthetic bacteria for hydrogen production: The present state of the art. World J Microbiol Biotechnol 2007;23:31–42. https://doi.org/10.1007/s11274-006-9190-9.

[196] Pottier L, Pruvost J, Deremetz J, Cornet J-F, Legrand J, Dussap CG. A fully predictive model for one-dimensional light attenuation byChlamydomonas

reinhardtii in a torus photobioreactor. Biotechnol Bioeng 2005;91:569–82. https://doi.org/10.1002/bit.20475.

[197] Rio-chanona EA, Ahmed N rashid, Zhang D, Lu Y, Jing K. Kinetic Modeling and Process Analysis for Desmodesmus sp. Lutein Photo-Production. AICHE Journal 2017;63:2546–54. https://doi.org/10.1002/aic.

[198] Zhang D, Wan M, del Rio-Chanona EA, Huang J, Wang W, Li Y, et al. Dynamic modelling of Haematococcus pluvialis photoinduction for astaxanthin production in both attached and suspended photobioreactors. Algal Res 2016;13:69–78. https://doi.org/10.1016/j.algal.2015.11.019.

[199] Wächter A, Biegler LT. On the implementation of an interior-point filter line-search algorithm for large-scale nonlinear programming. Math Program 2006;106:25–57. https://doi.org/10.1007/s10107-004-0559-y.

[200] Hart WE, Laird C, Watson J-P, Woodruff DL. Pyomo – Optimization Modeling in Python. vol. 67. Boston, MA: Springer US; 2012. https://doi.org/10.1007/978-1-4614-3226-5.

[201] Brun R, Martin K, Siegrist H, Gujer W, Reichert P. Practical identifiability of ASM2d parameters — systematic selection and tuning of parameter subsets. Water Res 2002;36:4113–27. https://doi.org/10.1016/S0043-1354(02)00104-5.

[202] Sin G, Gernaey K, Lantz A. Good Modeling Practice for PAT Applications : Propagation of Input Uncertainty and Sensitivity Analysis. Biotechnol Prog 2009:1043–53. https://doi.org/10.1002/btpr.166.

[203] Zhang D, Savage TR, Cho BA. Combining model structure identification and hybrid modelling for photo-production process predictive simulation and optimisation. Biotechnol Bioeng 2020;117:3356–67. https://doi.org/10.1002/bit.27512.

[204] Sánchez JF, Fernández-Sevilla JM, Acién FG, Cerón MC, Pérez-Parra J, Molina-Grima E. Biomass and lutein productivity of Scenedesmus almeriensis: influence of irradiance, dilution rate and temperature. Appl Microbiol Biotechnol 2008;79:719–29. https://doi.org/10.1007/s00253-008-1494-2.

[205] Li X, Wang Y, Zhang S, Chu J, Zhang M, Huang M, et al. Effects of light/dark cycle, mixing pattern and partial pressure of H2 on biohydrogen production by Rhodobacter sphaeroides ZX-5. Bioresour Technol 2011;102:1142–8. https://doi.org/10.1016/j.biortech.2010.09.015.

[206] Liao Q, Liu DM, Ye DD, Zhu X, Lee DJ. Mathematical modeling of two-phase flow and transport in an immobilized-cell photobioreactor. Int J Hydrogen Energy 2011;36:13939–48. https://doi.org/10.1016/j.ijhydene.2011.03.088.

[207] Cerruti M, Ouboter HT, Chasna V, van Loosdrecht MCM, Picioreanu C, Weissbrodt DG. Effects of light / dark diel cycles on the photoorganoheterotrophic metabolism of Rhodopseudomonas palustris for differential electron allocation to PHAs and H2. BioRxiv 2020. https://doi.org/10.1101/2020.08.19.258533.

[208] Aslanbay Guler B, Deniz I, Demirel Z, Oncel SS, Imamoglu E. Comparison of different photobioreactor configurations and empirical computational fluid dynamics simulation for fucoxanthin production. Algal Res 2019;37:195–204. https://doi.org/10.1016/j.algal.2018.11.019.

[209] Trentin G, Barbera E, Bertucco A, Sforza E. Role of oxygen in tubular photobioreactors: Model-Based design and operating conditions to minimize productivity losses. Chemical Engineering and Processing - Process Intensification 2020;157:108151. https://doi.org/10.1016/j.cep.2020.108151.

[210] el Ibrahimi M, Khay I, el Maakoul A, Moussa MO, Barkaoui A, Bakhouya M. Anaerobic co-digestion in a liquid recirculation pilot-scale reactor: Thermal and hydraulic study. Energy Reports 2020;6:496–502. https://doi.org/10.1016/j.egyr.2019.09.014.

[211] Saini AK, Paritosh K, Singh AK, Vivekanand V. CFD approach for pumped-recirculation mixing strategy in wastewater treatment: Minimizing power consumption, enhancing resource recovery in commercial anaerobic digester. Journal of Water Process Engineering 2021;40:101777. https://doi.org/10.1016/j.jwpe.2020.101777.

[212] Rivas J, Sadino-Riquelme MC, Garcés I, Carvajal A, Donoso-Bravo A. Spatial and temporal validation of a cfd model using residence time

distribution test in a tubular reactor. Computation 2020;8:1–10. https://doi.org/10.3390/computation8040094.

[213] Vaiano V, Sacco O, Pisano D, Sannino D, Ciambelli P. From the design to the development of a continuous fixed bed photoreactor for photocatalytic degradation of organic pollutants in wastewater. Chem Eng Sci 2015;137:152–60. https://doi.org/10.1016/j.ces.2015.06.023.

[214] Zhao L, Li J, Battaglia F, He Z. Investigation of multiphysics in tubular microbial fuel cells by coupled computational fluid dynamics with multi-order Butler-Volmer reactions. Chemical Engineering Journal 2016;296:377–85. https://doi.org/10.1016/j.cej.2016.03.110.

[215] Wols BA, Hofman JAMH, Uijttewaal WSJ, Rietveld LC, van Dijk JC. Evaluation of different disinfection calculation methods using CFD. Environmental Modelling and Software 2010;25:573–82. https://doi.org/10.1016/j.envsoft.2009.09.007.

[216] Greene DJ, Haas CN, Farouk B. Computational Fluid Dynamics Analysis of the Effects of Reactor Configuration on Disinfection Efficiency. Water Environment Research 2006;78:909–19. https://doi.org/10.2175/106143005x72984.

[217] Haynes WM, Lide DR, Bruno TJ. CRC Handbook of Chemistry and Physics. 97th Editi. Boca Raton, FLorida: CRC Press/Taylor & Francis; 2017.

[218] Zhang L, Pan Q, Rempel GL. Residence time distribution in a multistage agitated contactor with newtonian fluids: CFD prediction and experimental validation. Ind Eng Chem Res 2007;46:3538–46. https://doi.org/10.1021/ie060567+.

[219] Anane E, López C DC, Barz T, Sin G, Gernaey K v., Neubauer P, et al. Output uncertainty of dynamic growth models: Effect of uncertain parameter estimates on model reliability. Biochem Eng J 2019;150:107247. https://doi.org/10.1016/j.bej.2019.107247.

[220] Sin G, Meyer AS, Gernaey K v. Assessing reliability of cellulose hydrolysis models to support biofuel process design-Identifiability and uncertainty analysis. Comput Chem Eng 2010;34:1385–92. https://doi.org/10.1016/j.compchemeng.2010.02.012.

[221] Xu B, Li P, Waller P. Study of the flow mixing in a novel ARID raceway for algae production. Renew Energy 2014;62:249–57. https://doi.org/10.1016/j.renene.2013.06.049.

[222] Bayareh M. Artificial diffusion in the simulation of micromixers: A review. Proc Inst Mech Eng C J Mech Eng Sci 2021;235:5288–96. https://doi.org/10.1177/0954406220982028.

[223] Liu M. Computational study of convective-diffusive mixing in a microchannel mixer. Chem Eng Sci 2011;66:2211–23. https://doi.org/10.1016/j.ces.2011.02.036.

[224] Michalcová V, Kotrasová K. The numerical diffusion effect on the cfd simulation accuracy of velocity and temperature field for the application of sustainable architecture methodology. Sustainability (Switzerland) 2020;12:1–18. https://doi.org/10.3390/su122310173.

[225] Münkel R, Schmid-Staiger U, Werner A, Hirth T. Optimization of outdoor cultivation in flat panel airlift reactors for lipid production by Chlorella vulgaris. Biotechnol Bioeng 2013;110:2882–93. https://doi.org/10.1002/bit.24948.

[226] Wang L lin, Tao Y, Mao X zhong. A novel flat plate algal bioreactor with horizontal baffles: Structural optimization and cultivation performance. Bioresour Technol 2014;164:20–7. https://doi.org/10.1016/j.biortech.2014.04.100.

[227] Qin C, Lei Y, Wu J. Light/dark cycle enhancement and energy consumption of tubular microalgal photobioreactors with discrete double inclined ribs. Bioresources and Bioprocessing 2018;5. https://doi.org/10.1186/s40643-018-0214-8.

[228] Salguero-Rodríguez Y, Gómez-Pérez CA, Arango-Restrepo JP, Espinosa J. Static mixer proposal for tubular photobioreactors to reduce mixing energy consumption and enhance light–dark cycles. Journal of Chemical Technology and Biotechnology 2021;96:113–24. https://doi.org/10.1002/jctb.6516.

[229] Perner-Nochta I, Posten C. Simulations of light intensity variation in photobioreactors. Journal of Biotechnology 2007;131:276–85. https://doi.org/10.1016/j.jbiotec.2007.05.024.